Modeling the growth of cytosolic TDP-43 inclusion bodies and accumulated neurotoxicity of misfolded oligomers in neurons

Andrey V. Kuznetsov

Department of Mechanical and Aerospace Engineering, North Carolina State University,

Raleigh, NC 27695-7910, USA; e-mail: avkuznet@ncsu.edu

Abstract

This paper introduces a mathematical model for the growth of transactive response DNA binding protein of 43 kDa (TDP-43) inclusion bodies in neuron soma. The parameter representing the accumulated neurotoxicity caused by misfolded TDP-43 oligomers is also introduced. The model's equations enable the numerical calculation of the concentrations of TDP-43 monomers, dimers, free oligomers, and oligomers deposited in inclusion bodies. By simulating the deposition of free oligomers into inclusion bodies, the model predicts the size of TDP-43 inclusion bodies. An approximate solution to the model equations is derived for the scenario where protein degradation machinery is dysfunctional, leading to infinite half-lives for TDP-43 dimers, monomers, and both free and deposited oligomers. This solution, valid at large times, predicts that the radius of the inclusion body increases proportionally to the cube root of time, whereas the accumulated neurotoxicity increases linearly with time. To the best of the author's knowledge, this study is the first to model the relationship between the size of TDP-43 inclusion bodies and time, and the first to introduce the concept of accumulated neurotoxicity caused by misfolded TDP-43 oligomers. Sensitivity analysis of the approximate solution indicates that the inclusion body radius and accumulated neurotoxicity become independent of the kinetic constants at large timescales. While the numerical solution of the full mathematical model continues to work with finite half-lives, the approximate solution becomes invalid for scenarios with physiologically relevant (finite) half-lives of TDP-43 dimers, monomers, and free misfolded oligomers. In contrast to the scenario with infinite half-lives, the numerical solution reveals that, for different values of the kinetic constants, the curves representing the inclusion body radius and accumulated neurotoxicity converge to distinct curves over time.

Keywords neuron; amyotrophic lateral sclerosis; frontotemporal lobar degeneration; Finke-Watzky model; mathematical modeling

Abbreviations

ALS amyotrophic lateral sclerosis

F-W Finke-Watzky

FTLD frontotemporal lobar degeneration

TDP-43 transactive response DNA binding protein of 43 kDa

1. Introduction

The presence of transactive response DNA binding protein of 43 kDa (TDP-43) inclusion bodies represents a pathological hallmark in amyotrophic lateral sclerosis (ALS) and frontotemporal lobar degeneration (FTLD) diseases (Ishii et al. 2017; Jo et al. 2020; Prasad et al. 2019; Capitini et al. 2014). ALS is distinguished by the gradual decline of motor neurons, resulting in skeletal muscle weakness and, ultimately, fatality within a span of 3 to 5 years (Oiwa et al. 2023; Sugai et al. 2018). FTLD is an early-onset neurodegenerative disease characterized by progressive deterioration in behavior and language due to the loss of neurons, primarily in the frontal or temporal lobes, with a life expectancy of 6-8 years (Grossman et al. 2023). TDP-43, a nuclear, intrinsically disordered, soluble protein (Sun et al. 2019; French et al. 2019) with a molecular weight of 43 kDa (Suk and Rousseaux 2020), is synthesized in the cytoplasm and, in healthy neurons, predominantly resides in the nucleus (Pérez-Berlanga et al. 2023; Necarsulmer et al. 2023; Meneses et al. 2021). TDP-43 is degraded through both the proteasomal and autophagy pathways (Chhangani et al. 2021). However, in TDP-43 proteinopathies, this protein undergoes mislocalization from the nucleus to the cytoplasm (Glass 2020; Suk and Rousseaux 2020), forming TDP-43 inclusion bodies characterized by ubiquitinated and hyper-phosphorylated variants of TDP-43 (Prasad et al. 2019).

Under pathological conditions, TDP-43 undergoes a conversion from its native dimeric state (Jiang et al. 2017) to a monomeric form. This transformation results in TDP-43 mislocalization from the nucleus to the cytoplasm, where it forms irreversible, amorphous aggregates (Sun et al. 2014; Oiwa et al. 2023). Subsequently, these aggregates grow into inclusion bodies. Notably, the nature of these inclusion bodies, whether they exhibit toxicity or act in a neuroprotective manner by sequestering toxic soluble oligomers, remains uncertain (Ishii et al. 2017; Glass 2020). There is a possibility that TDP-43 pathology spreads between neurons through a prion-like mechanism (Jo et al. 2020; Chong and Forman-Kay 2016).

The proposed model is based on the following hypotheses regarding the mechanism of TDP-43 aggregation. First, TDP-43 dimers dissociate into monomers, which then translocate from the nucleus to the cytoplasm (Ingólfsson et al. 2023; Oiwa et al. 2023). Subsequent aggregation events occur in the cytoplasm, where monomers convert into pathogenic oligomers with autocatalytic properties (Wells et al. 2021; French et al. 2019); de Boer et al. 2021). These pathogenic oligomers deposit into sticky TDP-43 inclusion bodies, driving their growth (Lye and Chen 2022).

It is important to distinguish between physiological and pathological oligomers. Physiological oligomers play functional roles, such as supporting RNA splicing activity in the nucleus (Lye and Chen 2022).

However, as this study focuses on inclusion body growth, the term "oligomers" hereafter refers exclusively to pathological forms.

The developed model simulates the growth of TDP-43 inclusion bodies and predicts the relationship between their radius and time. This model builds upon the author's previous research, which explored the growth of amyloid-β plaques (Kuznetsov 2024b) and Lewy bodies (Kuznetsov and Kuznetsov 2022; Kuznetsov 2024a). The growth of TDP-43 inclusion bodies is simulated using the methodology developed in Kuznetsov (2024b), Kuznetsov (2024a). The model includes equations that describe the conservation of TDP-43 monomers, dimers, free misfolded oligomers, and misfolded oligomers deposited into inclusion bodies. TDP-43 misfolded oligomers are referred to as pathological and toxic oligomers hereafter. The conversion of TDP-43 monomers into free misfolded oligomers is simulated using the Finke-Watzky (F-W) model.

This paper also proposes a criterion to characterize the neurotoxicity of misfolded TDP-43 oligomers, which are hypothesized to be the main toxic species in ALS and FTLD. An approximate solution for accumulated neurotoxicity, derived under the assumption of dysfunctional degradation machinery for TDP-43 protomers, predicts a linear increase in neurotoxicity from the onset of misfolded oligomer formation.

2. Materials and models

2.1. Governing equations

According to Oiwa et al. (2023), the initial stage of TDP-43 aggregation involves the monomerization of TDP-43 dimers:

$$D \xrightarrow{k_M} 2M \tag{1}$$

Monomeric TDP-43 lacks functionality and is more likely to escape the nucleus, possibly through passive diffusion, while also being prone to aggregation. As a result, in ALS and FTLD, most TDP-43 inclusions are found in the cytoplasm Pérez-Berlanga et al. (2023). Consequently, the model focuses on simulating TDP-43 inclusion bodies' formation in the cytoplasm.

French et al. (2019) suggested that TDP-43 misfolded oligomers serve as critical intermediates in the transition to irreversible aggregates. To simulate TDP-43 aggregation, a phenomenological two-step F-W model, as described in Morris et al. (2008), Iashchishyn et al. (2017), was employed. The F-W model, which has been successfully applied to fit experimental data on neurological protein aggregation (Morris

et al. 2008), simulates polymer aggregation through two pseudoelementary, parallel, and competing processes: continuous nucleation and autocatalytic growth catalyzed by oligomer surfaces (Finke et al. 2020). The F-W model is characterized by the following transitions:

$$M \xrightarrow{k_1} B \tag{2}$$

$$M + B \xrightarrow{k_2} 2B \tag{3}$$

The mathematical model is derived by establishing four conservation statements for dimers, monomers, free misfolded oligomers, and misfolded oligomers deposited into inclusion bodies. The model employs the lumped capacitance approximation, with time, *t*, as the sole independent variable. The dependent variables are listed in Table 1, and the model parameters are summarized in Table 2.

The conservation of TDP-43 dimers in the soma is expressed by the following equation:

$$\frac{d[D]}{dt} = \frac{q_D}{V_{soma}} a_{21} - k_M [D] - [D] \frac{\ln(2)}{T_{1/2,D}} \tag{4}$$

In Eq. (4), $a_{21} = 10^{21} \frac{\mu\text{M}\ \mu\text{m}^3}{\text{mol}}$ represents the conversion factor from $\frac{\text{mol}}{\mu\text{m}^3}$ to μM. The first term on the right-hand side of Eq. (4) simulates the rate at which TDP-43 dimers, a native form of TDP-43, are produced in the soma. TDP-43 is an RNA-binding protein (Scherer et al. 2024). TDP-43 regulates its own expression by binding to specific sequences in its mRNA, thereby reducing its production rate (Ayala et al. 2011; Koehler et al. 2022). Therefore, it is likely that q_D decreases as the concentration of TDP-43 dimers increases. Since the exact dependence of q_D on $[D]$ is unknown, q_D is assumed to be constant in this study. The second term is formulated by applying the law of mass action to describe the rate of reaction in Eq. (1). The third term simulates the degradation of TDP-43 dimers due to their finite half-life.

The conservation of TDP-43 monomers in the soma is described by the following equation:

$$\frac{d[M]}{dt} = 2k_M [D] - k_1 [M] - k_2 [M][B] - [M] \frac{\ln(2)}{T_{1/2,M}}, \tag{5}$$

where the first term on the right-hand side describes the generation of TDP-43 monomers through their conversion from dimers. The second term simulates the decrease of monomer concentration resulting from their transformation into the misfolded active form capable of autocatalysis (pathological oligomers). In the F-W model, this process is conceptualized as a nucleation process (refer to Eq. (2)). The third term accounts for the decrease of monomer concentration due to autocatalytic conversion into

misfolded oligomers (refer to Eq. (3)). The fourth term represents the degradation of TDP-43 monomers due to their finite half-life.

By expressing the conservation of TDP-43 misfolded oligomers, the following is derived:

$$\frac{d[B]}{dt} = k_1[M] + k_2[M][B] - [B]\frac{\ln(2)}{T_{1/2,B}} - [B]\frac{\ln(2)}{\theta_{1/2,B}} \tag{6}$$

The first and second terms on the right-hand side of Eq. (6) simulate the generation of TDP-43 misfolded oligomers resulting from their production from monomers through nucleation and autocatalytic processes, respectively. The third term on the right-hand side represents the decline of TDP-43 misfolded oligomers due to their limited half-life.

The formation of TDP-43 inclusion bodies from sticky misfolded oligomers is modeled similarly to colloidal suspension coagulation in Boltachev and Ivanov (2020). In the model, free misfolded TDP-43 oligomers (B) are assumed to have a half-life of $\theta_{1/2,B}$. These misfolded oligomers deposit into TDP-43 inclusion bodies, and the concentration of the deposited oligomers is denoted as $[I]$.

$$\frac{d[I]}{dt} = [B]\frac{\ln(2)}{\theta_{1/2,B}} - [I]\frac{\ln(2)}{T_{1/2,I}} \tag{7}$$

In Eq. (7), the first term on the right-hand side corresponds to the fourth term in Eq. (6) with the opposite sign, while the second term represents the half-life of deposited TDP-43 oligomers incorporated into inclusion bodies.

Eqs. (4)-(7) are solved with the following initial conditions:

At $t = 0$: $\quad [D] = [D]_0, \quad [M] = 0, \quad [B] = 0, \quad [I] = 0$ (8a,b,c,d)

Table 1. Dependent variables in the model.

Symbol	Definition	Unit
$[B]$	Molar concentration of free toxic (pathological, misfolded) TDP-43 oligomers	μM
$[D]$	Molar concentration of TDP-43 dimers, representing the native form of TDP-43	μM

$[I]$	Concentration of toxic TDP-43 oligomers incorporated into inclusion bodies	μM
$[M]$	Molar concentration of TDP-43 monomers	μM
r_{IB}	Radius of the growing inclusion body, assuming it takes on a spherical form	μm

Table 2. Model parameters along with their estimated values.

Symbol	Definition	Unit	Value or range	Reference or estimation method	Value(s) used in computations
a_{21}	Conversion factor from $\frac{\text{mol}}{\mu\text{m}^3}$ to μM	$\frac{\mu\text{M}\ \mu\text{m}^3}{\text{mol}}$	10^{21}		10^{21}
$[D]_0$	Initial concentration of TDP-43 dimers	μM			0 [a]
D_{soma}	Diameter of the soma	μm	20 [b]		20
D_{IB}	Diameter of a mature spherical TDP-43 inclusion body	μm	1-25 μm [c]	Cascella et al. (2022)	8
k_1	Rate constant associated with the first pseudoelementary step in the F-W model that describes the nucleation of the misfolded form of TDP-43 oligomers prone to aggregation	s^{-1}			10^{-8}, 10^{-6}, 10^{-4} [d]

k_2	Rate constant associated with the second pseudoelementary step of the F-W model that describes the autocatalytic growth of the misfolded form of TDP-43 oligomers prone to aggregation	$\mu M^{-1}\ s^{-1}$			10^{-8}, 10^{-6}, 10^{-4} [e]
k_M	Rate constant associated with the reaction that describes the conversion of TDP-43 dimers into monomers	s^{-1}			10^{-6}, 10^{-4}, 10^{-2} [f]
MW	Molecular weight of TDP-43 monomer	$g\ mol^{-1}$	4.3×10^{4} [g]	Suk and Rousseaux (2020), Meneses et al. (2021), Hadley et al. (2015)	4.3×10^{4}
N_A	Avogadro's number	mol^{-1}	6.022×10^{23}		6.022×10^{23}
N_{IB}	Number of mature TDP-43 inclusion bodies within the soma (assumed to be of the same volume)		0-4 [h]	Ishii et al. (2017)	2
q_D	Rate at which TDP-43 dimers are	$mol\ s^{-1}$	6.68×10^{-23}	Estimated using Eq. (29)	6.68×10^{-23}

	generated within the soma				
$t_{IB,f}$	Duration of TDP-43 inclusion body growth	s	1.26×10^{8} [i]	Prasad et al. (2019), Oiwa et al. (2023), Chhangani et al. (2021), Sugai et al. (2018)	1.26×10^{8}
$T_{1/2,B}$	Half-life of misfolded TDP-43 oligomers	s	8.64×10^{4} - 1.73×10^{5} [j]	Prasad et al. (2019)	1.30×10^{5}, 10^{20} (to simulate $T_{1/2,B}\to\infty$)
$T_{1/2,D}$	Half-life of TDP-43 dimers	s	4.32×10^{4} [k]	Ling et al. (2010), Prasad et al. (2019)	4.32×10^{4}, 10^{20} (to simulate $T_{1/2,D}\to\infty$)
$T_{1/2,I}$	Half-life of TDP-43 oligomers once they have been deposited into inclusion bodies	s	10^{20} [l]		10^{20} (to simulate $T_{1/2,I}\to\infty$)
$T_{1/2,M}$	Half-life of TDP-43 monomers	s	4.32×10^{4} [m]	Ling et al. (2010), Prasad et al. (2019)	4.32×10^{4}, 10^{20} (to simulate $T_{1/2,M}\to\infty$)
V_{soma}	Volume of the soma	μm^3	4.19×10^{3} [n]		4.19×10^{3}
$\theta_{1/2,B}$	Half-deposition time of free TDP-43 misfolded oligomers into inclusion bodies, defined as the time required for half of the free TDP-43 misfolded oligomers within the soma (Fig.	s			10^{7} [o]

	1) to be deposited into inclusion bodies				
ρ_{IB}	Density of TDP-43 inclusion bodies	g/μm^3	1.35×10^{-12} [p]	Cavicchi et al. (2018)	1.35×10^{-12}

[a] Because TDP-43 dimers are assumed to be generated continuously, their initial concentration becomes less significant over extended periods of time.

[b] A representative neuron with a soma diameter of 20 μm was considered.

[c] Mature spherical TDP-43 inclusions vary in diameter from 1 to 25 μm, while skein-like inclusions have diameters ranging from 0.5 to 1.0 μm and lengths extending up to 15 μm (Cascella et al. 2022).

[d] As there is a lack of published data on the kinetic rates in the F-W model describing the aggregation of TDP-43 protein, three representative values, 10^{-8}, 10^{-6}, 10^{-4} s^{-1}, were selected for k_1 based on information presented in Morris et al. (2008) for various proteins (summarized in Table S1). The data presented in Morris et al. (2008) were obtained by curve-fitting experimental results reported in Bieschke et al. (2005), Vestergaard et al. (2005), Lu et al. (2003), Dong et al. (2006), Zirah et al. (2006), Fink (2006), Sode et al. (2005), Chen et al. (2002), Wetzel (2006), Ban et al. (2006), Dumoulin et al. (2006), all of which are also cited in Table S1.

[e] Due to the absence of published data on the kinetic rates in the F-W model describing the aggregation of TDP-43 protein, three representative values, 10^{-8}, 10^{-6}, 10^{-4} μM^{-1} s^{-1}, were selected for k_2 based on information presented in Morris et al. (2008) for various proteins (summarized in Table S1).

[f] Given that the half-life of the first-order reaction involved in TDP-43 monomerization (refer to Eq. (1)) is on the order of hours (Oiwa et al. 2023), and the rate constant of a first-order reaction is $k_M = 0.693 / T_{1/2}$, three representative kinetic rates, 10^{-6}, 10^{-4}, 10^{-2} s^{-1}, were employed to simulate potential rates of the TDP-43 monomerization reaction.

[g] A mass of TDP-43 monomer is 43,000 dalton (Suk and Rousseaux 2020; Meneses et al. 2021; Hadley et al. 2015).

[h] Number of TDP-43 inclusion bodies is taken from Fig. 8C in Ishii et al. (2017).

[i] In cases of ALS, patients typically succumb to the disease within 2–5 years from the onset of symptoms (Prasad et al. 2019; Oiwa et al. 2023; Chhangani et al. 2021; Sugai et al. 2018). The growth of TDP-43 inclusion bodies probably commenced even before the manifestation of the disease symptoms. Consequently, a growth duration of 4 years was assumed for the inclusion bodies, after which the neuron undergoes cell death.

[j] Given that the stability of TDP-43 increases in mutations (24-48 hours versus 12 hours for the wild type as shown in Prasad et al. 2019), it was hypothesized that the half-life of the misfolded form of TDP-43 is 2-4 times longer than that of the wild-type TDP-43.

[k] The reported half-life of wild-type TDP-43 is 12 hours (Ling et al. 2010; Prasad et al. 2019). Given that native TDP-43 exists in a dimeric form Sun et al. (2014), this half-life was attributed to TDP-43 dimers.

[l] Without therapeutic intervention, TDP-43 inclusion bodies are expected to degrade much slower than TDP-43 monomers and oligomers. Therefore, for computational modeling, they are considered stable, with an effectively infinite half-life.

[m] The same half-life of 12 hours was assumed for both TDP-43 monomers and TDP-43 dimers.

[n] Assuming a soma diameter of 20 μm, the volume of the soma is calculated to be $\frac{1}{6}\pi D_{soma}^{3} = 4.19\times10^{3}$ μm³.

[o] Assumed value.

[p] A commonly employed density value that remains consistent across different protein types is 1.35 g/cm³ (Cavicchi et al. 2018).

2.2. Criterion for assessing the accumulated neurotoxicity of pathological TDP-43 oligomers

The role of TDP-43 inclusion bodies in the neural tissue of individuals diagnosed with ALS or FTLD remains debated, as they may function as primary neurotoxic agents, harmless byproducts, or protective structures sequestering misfolded proteins (Baloh 2011). Liu et al. (2013) proposed that although TDP-43 aggregation may be correlated with neuronal cell death, it is not necessarily its direct cause. Accordingly, this study hypothesizes that TDP-43 neurotoxicity arises from misfolded TDP-43 oligomers and progressively accumulates over time as neurons are exposed to these toxic species, whereas inclusion bodies are primarily neuroprotective.

It is important to distinguish between functional and pathological (misfolded) oligomers of TDP-43. Functional oligomerization is crucial for TDP-43's role in nuclear splicing regulation and its incorporation into cytoplasmic stress granules during cellular stress (Pérez-Berlanga et al. 2023). French et al. (2019) noted similarities between TDP-43 pathological aggregation and the aggregation processes of tau, α-synuclein, and amyloid β, where oligomers are thought to be the primary toxic species. However, the neurotoxicity of TDP-43 oligomers remains a somewhat controversial topic. Fang et al. (2014) reported that TDP-43 oligomers could cause neurotoxicity and neurite degeneration. The neurotoxicity of TDP-43 oligomers was also reported in Lee et al. (2019), Lye and Chen (2022). Yang et al. (2024) produced recombinant TDP-43 oligomers and observed minimal or no neurotoxicity. However, these oligomers differed from those naturally occurring in cells. The structural and toxic characteristics of native TDP-43 oligomers may also be influenced by post-translational modifications, genetic mutations, and interactions with various cofactors (Yang et al. 2024). Kitamura et al. (2024) proposed that TDP-43 hetero-oligomers, formed by incorporating other proteins, exhibit greater neurotoxicity than their homo-oligomer counterparts. Lye and Chen (2022) provided a comprehensive review of misfolded TDP-43 oligomers, demonstrating their neurotoxic effects in both in vitro and in vivo studies.

The precise mechanism underlying the neurotoxicity of misfolded TDP-43 oligomers remains unknown. Some TDP-43 oligomers may be inherently more neurotoxic than others, or neurotoxicity could result from a heterogeneous mixture of oligomers with varying structures, stability, and concentrations. The mixture of oligomers may induce nonspecific neurotoxicity by interacting with membrane proteins, disrupting membrane lipids, triggering oxidative stress, and altering membrane dielectric properties and ion permeability (Benilova et al. 2012). If neurotoxicity results from the combined effects of various oligomers, a parameter quantifying the accumulated time-dependent damage caused by free misfolded TDP-43 oligomers can be defined, following Kuznetsov (2025a), Kuznetsov (2025b), as:

$$\Xi(t) = \int_0^t [B](\hat{t})\, d\hat{t} \tag{9}$$

If multiple distinct oligomeric TDP-43 species contribute to neurotoxicity with different weighting factors ω_1 and ω_2, then the neurotoxicity criterion can be reformulated as:

$$\Xi(t) = \omega_1 \int_0^t [B_1](\hat{t})\, d\hat{t} + \omega_2 \int_0^t [B_2](\hat{t})\, d\hat{t} + \ldots \tag{10}$$

Eqs. (9) and (10) provide microscale, or cellular-level, criteria for assessing TDP-43 neurotoxicity. These equations enable the evaluation of neurotoxicity for individual neurons.

2.3. Approximate solution for the case with $T_{1/2,D} \to \infty$, $T_{1/2,M} \to \infty$, $T_{1/2,B} \to \infty$, and $T_{1/2,I} \to \infty$

In the case of dysfunctional proteolytic machinery — namely, $T_{1/2,D} \to \infty$, $T_{1/2,M} \to \infty$, and $T_{1/2,B} \to \infty$ — the numerical simulations in Figs. S1-S3 indicate that the concentrations of TDP-43 dimers, monomers, and free misfolded oligomers—denoted as $[D]$, $[M]$, and $[B]$, respectively—gradually converge over time, reaching asymptotic steady-state values. This section focuses on determining these equilibrium concentrations. The analytical solution derived here, labeled as "approximate" in the figures, is obtained by applying steady-state conditions to Eqs. (4)-(6), yielding the following equations:

$$\frac{q_D}{V_{soma}} a_{21} - k_M [D] = 0 \tag{11}$$

$$2k_M [D] - k_1 [M] - k_2 [M][B] = 0 \tag{12}$$

$$k_1 [M] + k_2 [M][B] - [B] \frac{\ln(2)}{\theta_{1/2,B}} = 0 \tag{13}$$

Rearranging Eq. (11) to express $[D]$ yields:

$$[D] = \frac{q_D}{V_{soma} k_M} a_{21} \tag{14}$$

By adding Eq. (11) twice to Eqs. (12) and (13), the following expression is obtained:

$$\frac{2q_D}{V_{soma}} a_{21} - [B] \frac{\ln(2)}{\theta_{1/2,B}} = 0 \tag{15}$$

Rearranging Eq. (15) to express $[B]$ gives:

$$[B] = \frac{2q_D \theta_{1/2,B}}{V_{soma} \ln(2)} a_{21} \tag{16}$$

Incorporating Eqs. (14) and (16) into Eq. (12) and solving for $[M]$ gives:

$$[M] = \frac{2 \frac{q_D}{V_{soma}} a_{21}}{k_1 + k_2 \frac{2q_D \theta_{1/2,B}}{V_{soma} \ln(2)} a_{21}} \tag{17}$$

The numerically predicted concentration of dimers, $[D]$, quickly approaches a constant value, which is determined by the balance between dimer production and their conversion into monomers (Fig. S1). Fig. S1 demonstrates a strong agreement between the numerical and approximate (given by Eq. (14)) solutions for $[D]$ once time exceeds 0.002 years. As monomers convert into oligomers, the numerically predicted concentration of monomers, $[M]$, decreases over time, initially rapidly and then gradually (Fig. S2). The numerical and approximate (given by Eq. (17)) solutions for $[M]$ converge at large times, but the time it takes for the solutions to align depends on the value of k_1. The convergence is slower for larger values of k_1, taking approximately 1.5 years for the numerical solution to match the approximate solution when $k_1 = 10^{-4}$ s^{-1}. Note that $[M]$ converges to distinct asymptotic values, which depend on k_1 (Eq. (17)). The numerical solution for the concentration of free misfolded TDP-43 oligomers, $[B]$, exhibits a gradual increase to an asymptotic value over time, with the numerical and analytical (given by Eq. (16)) solutions (the latter gives a constant asymptotic value) converging after approximately 2.5 years (Fig. S3).

As $T_{1/2,I} \to \infty$, Eq. (7) can be reformulated as:

$$\frac{d[I]}{dt} = [B]\frac{\ln(2)}{\theta_{1/2,B}} \tag{18}$$

By incorporating Eq. (16) into Eq. (18), the following expression is obtained:

$$\frac{d[I]}{dt} = \frac{2q_D}{V_{soma}} a_{21} \tag{19}$$

Integrating Eq. (19) and applying the initial condition (8d) yields the following expression:

$$[I] = \frac{2q_D}{V_{soma}} a_{21} t \tag{20}$$

Fig. S4 illustrates that after approximately one year, the numerical solution for $[I]$ exhibits a linear increase. The numerical and approximate solutions for $[I]$ are similar but not identical. The discrepancy arises from differences between the numerical and approximate solutions for the concentration of free misfolded TDP-43 oligomers, $[B]$ (Fig. S3), leading to initial variations in the predicted concentrations of deposited oligomers, $[I]$, which persist over time.

Substituting the approximate solution for $[B]$ from Eq. (16) into Eq. (9) yields the following expression for accumulated neurotoxicity:

$$\Xi(t) = \frac{2q_D\theta_{1/2,B}}{V_{soma}\ln(2)}a_{21}t \tag{21}$$

Eq. (21) provides an approximate solution for $\Xi(t)$, indicating that accumulated neurotoxicity increases in direct proportion to disease duration.

2.4. Modeling the growth dynamics of TDP-43 inclusion bodies

The growth of TDP-43 inclusion bodies over time (see Fig. 1) is simulated using the following approach.

The total number of TDP-43 monomers incorporated into a single inclusion body at time *t* is given by the following equation, adapted from Watzky et al. (2008):

$$N_{single}(t) = \frac{1}{N_{IB}}\frac{[I](t)}{a_{21}}V_{soma}N_A \tag{22}$$

The F-W model does not distinguish between the molecular weights of monomers (native form) and misfolded oligomers (active form capable of autocatalysis); see Eqs. (2) and (3). In Eq. (13), N_{IB} represents the number of inclusion bodies in the soma, with the assumption that all inclusion bodies have equal volumes.

Alternatively, $N_{single}(t)$ can be calculated as follows (Watzky et al. 2008):

$$N_{single}(t) = \frac{V_{single}(t)\rho_{IB}}{MW}N_A \tag{23}$$

where MW denotes the molecular weight of TDP-43 monomers, defined as the sum of the atomic weights of all the atoms within a monomer.

By equating the right-hand sides of Eqs. (22) and (23) and solving for the volume of a single inclusion body, the following equation is obtained:

$$V_{single}(t) = \frac{[I](t)}{a_{21}N_{IB}}V_{soma}\frac{MW}{\rho_{IB}} \tag{24}$$

Substituting Eq. (20) into Eq. (24) yields:

$$V_{single}(t) = \frac{2}{N_{IB}} \frac{MW}{\rho_{IB}} q_D t \tag{25}$$

This implies that the volume of a single inclusion body in the soma increases linearly with both the rate of TDP-43 dimer generation and time.

The model includes separate equations for free misfolded TDP-43 oligomers (phase *B*) and oligomers deposited into TDP-43 inclusions (phase *I*). While free oligomers are initially highly dynamic structures, the model does not require resolving their shape—only an assumption about the shape of the inclusion bodies (phase *I*) is necessary.

TDP-43 inclusions within the soma can vary in shape, ranging from skein-like to rounded forms (Cascella et al. 2022). To simplify calculations, all inclusion bodies are assumed to be spherical and of uniform size. The volume of a spherical inclusion body is

$$V_{single}(t) = \frac{4}{3} \pi r_{IB}^3(t) \tag{26}$$

It is important to note that the model predicts the volume of the inclusion body, as in Eq. (25). In Eq. (26), the parameter r_{IB} can be interpreted as the effective radius, representing the radius of a sphere with the same volume as the inclusion body. This assumption does not impact the model's predictions regarding the growth of inclusion volume over time, as the model is independent of convexity. Therefore, variations in radius across the inclusion body structure do not affect the results.

Equating the right-hand sides of Eqs. (24) and (26) and solving for the radius of the inclusion body yields the following result:

$$r_{IB} = \left(\frac{3}{4\pi} \frac{[I]}{a_{21} N_{IB}} V_{soma} \frac{MW}{\rho_{IB}} \right)^{1/3} \tag{27}$$

Using the approximate solution for $[I]$ from Eq. (20) in Eq. (27), the following approximate solution for r_{IB} for the case of $T_{1/2,D} \to \infty$, $T_{1/2,M} \to \infty$, $T_{1/2,B} \to \infty$, and $T_{1/2,I} \to \infty$ is derived:

$$r_{IB} = \left(\frac{3}{2\pi} \frac{q_D}{N_{IB}} \frac{MW}{\rho_{IB}} \right)^{1/3} t^{1/3} \tag{28}$$

As indicated by Eq. (28), the radius of the inclusion body grows proportionally to the cube root of time. This growth is influenced by the production rate of TDP-43 dimers, q_D.

Eq. (28) can be utilized to estimate the rate at which TDP-43 dimers are generated in the soma. If, after the growth period $t_{IB,f}$ the inclusion body's radius attains the size $r_{IB,f}$, then, according to Eq. (28), q_D can be determined as:

$$q_D = \frac{2\pi}{3}\frac{\rho_{IB}}{MW}\frac{N_{IB}}{t_{IB,f}}r_{IB,f}^3 \tag{29}$$

2.5. Sensitivity analysis of the inclusion body radius and accumulated neurotoxicity of free misfolded TDP-43 oligomers with respect to model parameters

The study investigated the sensitivity of the inclusion body's radius, r_{IB}, to various parameters in Eq. (28). Local sensitivity coefficients (Beck and Arnold 1977; Zadeh and Montas 2010; Zi 2011; Kuznetsov and Kuznetsov 2019) were computed, representing the first-order partial derivatives of the inclusion body's radius with respect to, for example, the rate of TDP-43 dimer production, q_D, denoted by $\frac{\partial r_{IB}}{\partial q_D}$.

The dimensionless relative sensitivity coefficients (Zadeh and Montas 2010; Kacser et al. 1995) were determined as the ratio of the relative change in the inclusion body's radius, $\Delta r_{IB} / r_{IB}$, to the relative change in the respective parameter, in this case, $\Delta q_D / q_D$:

$$S_{q_D}^{r_{IB}} = \frac{q_D}{r_{IB}}\frac{\partial r_{IB}}{\partial q_D} = \frac{1}{3} \tag{30}$$

The approximate solution provided in Eq. (28) was used to calculate the derivative in Eq. (30). Importantly, the result in Eq. (30) is time-independent, indicating that the sensitivity remains constant at any given time. The positive sign of $S_{q_D}^{r_{IB}}$ suggests that r_{IB} increases with an increase in q_D. Similarly,

$$S_{MW}^{r_{IB}} = \frac{MW}{r_{IB}}\frac{\partial r_{IB}}{\partial MW} = \frac{1}{3} \tag{31}$$

$$S_{N_{IB}}^{r_{IB}} = \frac{N_{IB}}{r_{IB}}\frac{\partial r_{IB}}{\partial N_{IB}} = -\frac{1}{3} \tag{32}$$

$$S_{\rho_{IB}}^{r_{IB}} = \frac{\rho_{IB}}{r_{IB}}\frac{\partial r_{IB}}{\partial \rho_{IB}} = -\frac{1}{3} \tag{33}$$

$$S_{t}^{r_{IB}} = \frac{t}{r_{IB}}\frac{\partial r_{IB}}{\partial t} = \frac{1}{3} \tag{34}$$

Similarly, the dimensionless relative sensitivity coefficients characterizing the dependence of accumulated neurotoxicity on model parameters can be obtained using Eq. (21):

$$S_{q_D}^{\Xi} = \frac{q_D}{\Xi}\frac{\partial \Xi}{\partial q_D} = \frac{1}{3} \tag{35}$$

$$S_{\theta_{1/2,B}}^{\Xi} = \frac{\theta_{1/2,B}}{\Xi}\frac{\partial \Xi}{\partial \theta_{1/2,B}} = \frac{1}{3} \tag{36}$$

$$S_{V_{soma}}^{\Xi} = \frac{V_{soma}}{\Xi}\frac{\partial \Xi}{\partial V_{soma}} = -\frac{1}{3} \tag{37}$$

$$S_{t}^{\Xi} = \frac{t}{\Xi}\frac{\partial \Xi}{\partial t} = \frac{1}{3} \tag{38}$$

At large times, the sensitivity of r_{IB} to the kinetic constants k_1, k_2, and k_M is zero, as derived from the approximate solution (28). However, since this solution is valid only for long-term behavior, the numerical solution was used to evaluate the sensitivity of r_{IB} to these kinetic constants at earlier times. For instance:

$$S_{k_1}^{r_{IB}} = \frac{k_1}{r_{IB}}\frac{\partial r_{IB}}{\partial k_1} \approx \frac{k_1}{r_{IB}}\left.\frac{r_{IB}\left(k_1+\Delta k_1\right)-r_{IB}\left(k_1\right)}{\Delta k_1}\right|_{\text{other parmeters kept constant}} \tag{39}$$

where $\Delta k_1 = 10^{-3} k_1$ represents the step size. Sensitivity coefficients were computed using different step sizes to ensure that they remained unaffected by variations in step size.

Similarly, for large times, the sensitivity of Ξ to the kinetic constants k_1, k_2, and k_M is also zero, as indicated by the approximate analytical solution (21). Given that this solution applies only to large timescales, numerical simulations were employed to determine the sensitivity of Ξ to these kinetic constants at shorter time scales. For example:

$$S_{k_1}^{\Xi} = \frac{k_1}{r_{IB}}\frac{\partial \Xi}{\partial k_1} \approx \frac{k_1}{\Xi}\left.\frac{\Xi\left(k_1+\Delta k_1\right)-r_{IB}\left(k_1\right)}{\Delta k_1}\right|_{\text{other parmeters kept constant}} \tag{40}$$

2.6. Numerical solution

Eqs. (4)–(7), with initial conditions (8), were solved using MATLAB's well-validated ODE45 solver (MATLAB R2020b, MathWorks, Natick, MA, USA). To guarantee solution accuracy, the error tolerance

parameters, RelTol and AbsTol, were set to 1e-10. The convergence was established by calculating the residuals.

3. Results

Figs. 2, 5, 7, 9, 11, and 13 illustrate the radius of a TDP-43 inclusion body in a scenario where the soma contains two equally sized inclusion bodies. The model predicts the concentration of free misfolded TDP-43 oligomers, which are gradually deposited into the inclusion bodies, driving their growth. To simplify the interpretation, both inclusion bodies are assumed to be spherical, allowing the total volume of TDP-43 inclusion bodies to be expressed in terms of the radii of two identical spheres. Figs. 3, 6, 8, 10, 12, and 14 illustrate the accumulated neurotoxicity resulting from free misfolded TDP-43 oligomers.

Among all the model parameters listed in Table 2, the author had the least certainty regarding the values of the kinetic constants k_1, k_2, and k_M. An investigation was conducted to assess the consistency of the model's predictions, focusing on two key relationships: the direct proportionality of the TDP-43 inclusion body radius to the cube root of time, as described in Eq. (28), and the linear increase in accumulated neurotoxicity over time, as described in Eq. (21). This analysis was performed across a broad range of kinetic constant values.

Since inclusion bodies composed of misfolded TDP-43 are highly resistant to degradation (Ling et al. 2010), the half-life of TDP-43 oligomers deposited within them is assumed to be infinite (i.e. $T_{1/2,I} \to \infty$) in all figures. Figs. 2-8 are calculated for the scenario of dysfunctional protein degradation machinery, $T_{1/2,D} \to \infty$, $T_{1/2,M} \to \infty$, and $T_{1/2,B} \to \infty$. These figures show the effects of kinetic constants k_1, k_2, and k_M, respectively.

Fig. 2 shows that for $t > 0.2$ years the inclusion body's radius, r_{IB}, remains unaffected by the kinetic constant, k_1, that governs the conversion of TDP-43 monomers into a misfolded, aggregating form by nucleation. This is consistent with the approximate solution given by Eq. (28), indicating that the radius is insensitive to the kinetic constants. However, the validity of the approximate solution is limited to extended timeframes (for the parameter values used in computing Fig. 2, it is $t > 0.2$ years). Fig. 2 also shows that numerical solutions are close to the approximate solution given by Eq. (28), indicating that the inclusion body's radius grows approximately in proportion to $t^{1/3}$. The observed discrepancy between numerical and approximate solutions for r_{IB} (Fig. 2) stems from variations between the numerical and

approximate solutions for the concentration of free misfolded TDP-43 oligomers, $[B]$ (Fig. S3). These initial differences influence the predicted deposition rates of free misfolded oligomers into inclusion bodies, leading to a persistent deviation in their accumulated concentrations over time, $[I]$ (Fig. S4). Consequently, this results in a slight but systematic difference between the numerical and approximate solutions for the inclusion body radius, r_{IB} (Fig. 2). The approximate solution shown in Fig. 2a predicts larger values of r_{IB} than the numerical solution because it yields higher concentrations of $[B]$ and $[I]$ than the numerical solution, as illustrated in Figs. S3a and S4a.

Fig. 3 demonstrates that for $t > 0.12$ years, the accumulated neurotoxicity, Ξ, remains unaffected by the kinetic constant k_1, which governs the nucleation-driven conversion of TDP-43 monomers into misfolded, aggregation-prone oligomers. This aligns with the approximate solution derived in Eq. (21), which suggests that accumulated neurotoxicity is independent of kinetic parameters over extended timeframes. However, the validity of this approximation is constrained to later stages of disease progression (for the parameter values used in Fig. 3, this corresponds to $t > 0.12$ years). Additionally, Fig. 3 shows that the numerical results closely match the approximate solution given by Eq. (21), indicating that accumulated neurotoxicity increases approximately proportionally to time. The slight systematic deviation between the numerical and approximate solutions for Ξ (Fig. 3) can be attributed to differences between the numerical and approximate solutions for the concentrations of free misfolded TDP-43 oligomers, $[B]$, at the early stages of the process (Fig. S3).

The data depicting $\Xi(t)$ in Fig. 3a and $r_{IB}(t)$ in Fig. 2a have been combined to generate Fig. 4, which illustrates the relationship between accumulated neurotoxicity and the inclusion body radius, $\Xi = f(r_{IB})$. In ALS, larger TDP-43 inclusion bodies are often correlated with more severe disease progression and poorer prognosis (Jo et al. 2020). If the largest plaque sizes correspond to the most advanced disease stages and neuronal death occurs when plaques reach a critical size, the neurotoxicity threshold at which neurons die, Ξ_{crit}, can be estimated from Fig. 5 to be approximately 5×10^{10} μM·s, which corresponds to a plaque radius of around 3.5 μm. The approximate solution for $\Xi = f(r_{IB})$ is derived using Eqs. (21) and (28):

$$\Xi = \frac{4\pi\theta_{1/2,B} N_{IB} \rho_{IB}}{3V_{soma} MW \ln(2)} a_{21} r_{IB}^3 \tag{41}$$

As shown in Fig. 4, the agreement between the numerical and approximate solutions is excellent.

For different values of k_2, which represent the rate of autocatalytic aggregation of TDP-43 monomers, the numerical solution for the inclusion body radius, r_{IB}, gradually approaches the approximate solution given by Eq. (28) as time progresses (Fig. 5). The discrepancy between the numerical and approximate solutions for r_{IB} arises from differences in concentrations of free misfolded oligomers, $[B]$, predicted by numerical and approximate solutions during the first 2.5 years of the TDP-43 aggregation process (Fig. S7a). This variation leads to differing amounts of oligomers being deposited into inclusion bodies, explaining the shift between numerical and approximate solutions in Fig. 5a. Fig. 6 illustrates that for $t > 0.6$ years the accumulated neurotoxicity, Ξ, is not influenced by the kinetic constant k_2. This observation is consistent with the approximate solution given by Eq. (21), indicating that over long periods, accumulated neurotoxicity remains independent of kinetic constants.

The concentrations of TDP-43 dimers, monomers, and free misfolded oligomers converge to those given by the approximate solution (Figs. S5-S8). Note that as $t \to \infty$, $[M]$ converges to different asymptotic values, each depending on the value of k_2, as described in Eq. (17) (Fig. S6). The concentration of misfolded oligomers deposited into inclusion bodies reaches a linearly increasing curve with time (Fig. S8a), attributed to the constant supply of TDP-43 dimers at a rate of q_D.

Testing the numerical solution for various values of k_M, characterizing the rate of conversion of TDP-43 dimers into monomers, revealed that the numerical solution for r_{IB} converges to the cube root of time dependence, as predicted by the approximate solution in Eq. (28). The rate of convergence depends on the value of k_M (see Fig. 7), with the slowest convergence observed for the smallest tested value of 10^{-6} s^{-1}. At longer timescales, the accumulated neurotoxicity, Ξ, increases linearly with time, consistent with the approximate solution presented in Eq. (21) (Fig. 8a). In contrast, over shorter time scales, Ξ appears to exhibit a quadratic dependence on time (Fig. 8b). This aligns with the approximate solution for the neurotoxicity of amyloid β oligomers derived by Kuznetsov (2025a), which is applicable to shorter timeframes than the solution presented in this paper. That solution predicts that accumulated neurotoxicity increases quadratically with time.

The concentration of TDP-43 dimers, [*D*] (Fig. S9), is influenced by k_M, as it is inversely proportional to k_M for a constant value of q_D (see Eq. (14)). Numerical solutions converge to the approximate analytical solutions predicted by Eq. (14), resulting in three distinct curves corresponding to different values of k_M (Fig. S9). In contrast, the concentrations of monomers, $[M]$, and free misfolded oligomers, $[B]$,

converge to the analytical solutions given by Eqs. (17) and (16), respectively, which are independent of the value of k_M (Figs. S10 and S11). The concentration of misfolded TDP-43 oligomers deposited into inclusion bodies, $[I]$, exhibits a linear dependence on time at longer timescales (Fig. S12a). A slight discrepancy between the numerical solution and the approximate solution given by Eq. (20) (Fig. S12a) arises from differences in the concentrations of free oligomers, $[B]$, predicted by the numerical and analytical solutions during the initial 2.5 years of the process (Fig. S11a).

Figs. 9-14 are computed for physiologically relevant half-lives of TDP-43 dimers, monomers, and free misfolded oligomers ($T_{1/2,D} = 4.32\times10^4$ s, $T_{1/2,M} = 4.32\times10^4$ s, and $T_{1/2,B} = 1.30\times10^5$ s), indicating functional proteolytic machinery. These figures show the effects of kinetic constants k_1, k_2, and k_M, respectively. The approximate solution is not plotted, as it is exclusively applicable to the scenario involving infinite half-lives of TDP-43 dimers, monomers, and free misfolded oligomers.

In contrast to the case with infinite half-lives, the curves representing the radii of inclusion bodies do not converge to a single trajectory over time. Instead, for different values of the kinetic constants (k_1, k_2, and k_M), the curves differ, depending on the balance between the production of TDP-43 protomers and their degradation due to their finite half-lives (compare Fig. 9 with Fig. 2, Fig. 11 with Fig. 5, and Fig. 13 with Fig. 7). For finite half-lives, the final size of inclusion bodies after four years of growth is significantly smaller than that for infinite half-lives. For instance, in Fig. 9a, with $k_1 = 10^{-4}$ s^{-1}, the inclusion body reaches a size of 0.85 μm after four years, whereas in Fig. 2a, it grows to 4 μm.

Similarly, in the case of finite half-lives, the curves representing accumulated neurotoxicity do not converge to a single curve over time (compare Fig. 10 with Fig. 3, Fig. 12 with Fig. 6, and Fig. 14 with Fig. 8). However, even with finite half-lives, accumulated neurotoxicity increases linearly with time (Figs. 10a, 12a, and 14a). This relationship arises from the constant supply of TDP-43 dimers, q_D, in the model, as described by Eq. (4).

The concentration of TDP-43 dimers, $[D]$, remains independent of the kinetic constants k_1 and k_2 (Figs. S13 and S17) but varies with the value of k_M (Fig. S21). In contrast, the concentration of TDP-43 monomers, $[M]$, is influenced by k_1, k_2, and k_M (Figs. S14, S18, and S22). Similarly, the concentration of free misfolded TDP-43 oligomers, $[B]$, depends on k_1, k_2, and k_M (Figs. S15, S19, and S23). The

concentration of misfolded TDP-43 oligomers deposited into inclusion bodies, $[I]$, is also affected by k_1, k_2, and k_M (Figs. S16, S20, and S24). Notably, $[I]$ exhibits a linear dependence on time.

Fig. 15 examines the sensitivities of the inclusion body radius, r_{IB}, to the kinetic constants k_1, k_2, and k_M in a scenario where TDP-43 dimers, monomers, and free misfolded oligomers have an infinite half-life. At short timescales, the sensitivities to k_1, k_2, and k_M are positive, indicating that r_{IB} increases with increasing values of these kinetic constants. At larger timescales, the sensitivities of r_{IB} to all three kinetic constants gradually approach zero, consistent with the predictions obtained from the approximate analytical solution (Eq. (28)).

Fig. 16 examines the sensitivities of accumulated neurotoxicity, Ξ, to the kinetic constants k_1, k_2, and k_M in a scenario where TDP-43 dimers, monomers, and free misfolded oligomers have infinite half-lives. At small timescales, the sensitivities to k_1, k_2, and k_M are positive. At larger timescales, the sensitivities of Ξ to all three kinetic constants gradually approach zero, consistent with the predictions of the approximate analytical solution (Eq. (21)).

4. Discussion, limitations of the model, and future directions

This paper develops a model for the growth of TDP-43 inclusion bodies and introduces the concept of accumulated neurotoxicity caused by free misfolded TDP-43 oligomers. Numerical and approximate analytical solutions for neurotoxicity as a function of time were obtained. The model predicts the concentrations of TDP-43 dimers, monomers, free misfolded oligomers, and misfolded oligomers deposited into inclusion bodies.

In the case of dysfunctional protein degradation machinery—where protein dimers, monomers, and free misfolded oligomers have infinite half-lives—the model predicts that the inclusion body radius grows proportionally to the cube root of time, while accumulated neurotoxicity increases linearly over time. Since the kinetic constants governing TDP-43 monomerization, nucleation, and autocatalytic growth are not well-documented in the literature, an extensive analysis was conducted to assess the consistency of model predictions across a broad range of parameter values. The results indicate that the inclusion body radius and accumulated neurotoxicity are influenced by these kinetic constants only at short timescales.

The approximate solution, valid for infinite half-lives of TDP-43 protomers and long timescales, reveals that the concentration of TDP-43 dimers, $[D]$, is unaffected by the nucleation and autocatalytic kinetic

constants, k_1 and k_2, but depends on the monomerization kinetic constant, k_M (see Eq. (14)). In contrast, the concentration of TDP-43 monomers, $[M]$, is independent of k_M but varies with k_1 and k_2 (see Eq. (17)). The concentrations of free misfolded oligomers and those incorporated into inclusion bodies, $[B]$ and $[I]$, respectively, are independent of k_1, k_2, and k_M (see Eqs. (16) and (20)). The approximate solution also indicates a linear increase in the concentration of deposited TDP-43 oligomers, $[I]$, over time, attributed to the continuous synthesis of TDP-43 dimers in the cytoplasm (more precisely, TDP-43 monomers are synthesized and subsequently combined into dimers). The obtained results suggest that stabilization of TDP-43 dimers in the nucleus, which are not prone to aggregation, can be a viable therapeutic approach.

The approximate solution is no longer valid when considering physiologically relevant half-lives for TDP-43 dimers, monomers, and free misfolded oligomers. Unlike the case of infinite half-lives, the curves representing the inclusion body radii and accumulated neurotoxicity do not converge to a single trajectory over time for different values of the kinetic constants. The concentrations of dimers, monomers, and free misfolded oligomers reach distinct constant values, which depend on the values of the kinetic constants. Similarly, the concentrations of deposited misfolded oligomers converge to distinct linear trends over time.

When the half-lives of TDP-43 dimers, monomers, and free misfolded oligomers are assumed to be infinite, the sensitivities of the inclusion body radius to the kinetic constants governing nucleation, autocatalysis, and monomerization (k_1, k_2, and k_M) are positive at early times. As time progresses, all sensitivities gradually approach zero, indicating that at large timescales, the inclusion body radius becomes independent of these kinetic constants.

When the half-lives of TDP-43 dimers, monomers, and free misfolded oligomers are infinite, the sensitivities of accumulated neurotoxicity to the kinetic constants are initially positive but gradually decline to zero over time. This implies that, at large timescales, accumulated neurotoxicity is no longer affected by the kinetic constants.

The analysis presented here has limitations, primarily due to its reliance on a simplified mechanism of TDP-43 cytoplasmic mislocalization and subsequent aggregation, compounded by the absence of precise values for kinetic constants.

Investigating the biological mechanisms underlying TDP-43 misfolding would be highly valuable. Future studies should concentrate on developing more precise models for TDP-43 oligomerization, covering the

entire spectrum of oligomeric species, including trimers, tetramers, and multimers. Furthermore, the processes of TDP-43 phosphorylation and ubiquitination must be integrated into these models. Future models should incorporate simulations of TDP-43 shuttling between the nucleus and cytoplasm, the kinetics of TDP-43 binding to RNAs, and the impact of these processes on TDP-43 aggregation. Additionally, they should distinguish between physiological and pathological oligomerization. Investigating the potential prion-like spread of pathological TDP-43 species is also a crucial avenue for future exploration. Comparing the model's predictions with future experimental data will be essential for providing quantitative evidence to either support or refute the proposed theory.

Beyond neuronal cytoplasmic inclusions, neuropathological studies have also documented neuronal intranuclear inclusions and dystrophic neurites in both neurons and certain glial cells (Lee, E. B. et al. 2017). These diverse pathological features are frequently linked to the structural brain atrophy observed in neurodegenerative diseases (Youssef et al. 2024). Given the well-established role of TDP-43 as a nucleocytoplasmic shuttling protein, the current model's primary focus on cytosolic aggregation represents a limitation. Future extensions of the model should therefore consider incorporating aggregation dynamics across multiple subcellular compartments to better capture the full spectrum of TDP-43 pathology.

While the present model focuses on the aggregation dynamics of canonical TDP-43, it does not currently account for the heterogeneity of TDP-43 species often observed in disease states. Recent investigations have identified specific pathogenic variants, such as the 35-kDa N-terminally truncated species (Met85-TDP-35) arising from an alternative translation initiation site (Xiao et al. 2015). This variant is upregulated under pathological conditions and has been demonstrated to form cytoplasmic aggregates and induce motor neuron death. The exclusion of these alternative isoforms represents a limitation of the current framework. Future extensions of this model should therefore aim to incorporate the coexistence and interaction of multiple toxic TDP-43 species, examining how such variants might modulate the formation kinetics of misfolded oligomers and the subsequent growth of inclusion bodies.

The current model analyzes TDP-43 aggregation in isolation; however, in the context of FTLD, TDP-43 pathology often co-occurs with other proteinopathies. Recent evidence suggests that these co-pathologies may exacerbate neurodegeneration (Youssef et al. 2025). Consequently, limiting the simulation to a single aggregating species simplifies the complex proteostatic environment of the disease. A promising direction for future research is the extension of this mathematical framework to simulate the interaction kinetics between TDP-43 and other aggregating proteins, thereby broadening the model’s applicability to a wider spectrum of neurodegenerative disorders.

Incorporating modern mathematical techniques developed for biological problems—particularly those that offer tools for accounting for the elasticity of domain boundaries (in this case, the neuron)—would greatly enhance future models (Alghamdi et al. 2024; Sher Akbar et al. 2023; Maraj et al. 2023; Ghailan et al. 2023; Akbar et al. 2023; Akram and Akbar 2023; Akbar and Muhammad 2023; Akbar et al. 2024; Noreen and Akhtar 2023).

Acknowledgment

The author acknowledges the support provided by the National Science Foundation (grant DMS-2451660) and the Alexander von Humboldt Foundation through the Humboldt Research Award.

References

Akbar NS, Akhtar S, Maraj EN, Anqi AE, Homod RZ. 2023. Heat transfer analysis of MHD viscous fluid in a ciliated tube with entropy generation. Mathematical Methods in the Applied Sciences. 46:11495–11508.

Akbar NS, Muhammad T. 2023. Physical aspects of electro osmotically interactive cilia propulsion on symmetric plus asymmetric conduit flow of couple stress fluid with thermal radiation and heat transfer. Scientific Reports. 13:18491.

Akbar NS, Rafiq M, Muhammad T, Alghamdi M. 2024. Electro osmotically interactive biological study of thermally stratified micropolar nanofluid flow for copper and silver nanoparticles in a microchannel. Scientific Reports. 14:518.

Akram J, Akbar NS. 2023. Electroosmotically actuated peristaltic-ciliary flow of propylene glycol + water conveying titania nanoparticles. Scientific Reports. 13:11801.

Alghamdi M, Akbar NS, Zamir T, Muhammad T. 2024. Double layered combined convective heated flow of eyring-powell fluid across an elevated stretched cylinder using intelligent computing approach. Case Studies in Thermal Engineering. 54:104009.

Ayala YM, De Conti L, Avendaño-Vázquez SE, Dhir A, Romano M, D'Ambrogio A, Tollervey J, Ule J, Baralle M, Buratti E, Baralle FE. 2011. TDP-43 regulates its mRNA levels through a negative feedback loop. The EMBO Journal. 30:277–288.

Baloh RH. 2011. TDP-43: The relationship between protein aggregation and neurodegeneration in amyotrophic lateral sclerosis and frontotemporal lobar degeneration. The FEBS Journal. 278:3539–3549.

Ban T, Yamaguchi K, Goto Y. 2006. Direct observation of amyloid fibril growth, propagation, and adaptation. Accounts of Chemical Research. 39:663–670.

Beck JV, Arnold KJ. 1977. Parameter estimation in science and engineering. New York: Wiley.

Benilova I, Karran E, De Strooper B. 2012. The toxic aβ oligomer and Alzheimer's disease: An emperor in need of clothes. Nature Neuroscience. 15:349–357.

Bieschke J, Zhang Q, Powers ET, Lerner RA, Kelly JW. 2005. Oxidative metabolites accelerate Alzheimer's amyloidogenesis by a two-step mechanism, eliminating the requirement for nucleation. Biochemistry. 44:4977–4983.

Boltachev GS, Ivanov MG. 2020. Effect of nanoparticle concentration on coagulation rate of colloidal suspensions. Heliyon. 6:e03295.

Capitini C, Conti S, Perni M, Guidi F, Cascella R, De Poli A, Penco A, Relini A, Cecchi C, Chiti F. 2014. TDP-43 inclusion bodies formed in bacteria are structurally amorphous, non-amyloid and inherently toxic to neuroblastoma cells. PloS One. 9:e86720.

Cascella R, Bigi A, Riffert DG, Gagliani MC, Ermini E, Moretti M, Cortese K, Cecchi C, Chiti F. 2022. A quantitative biology approach correlates neuronal toxicity with the largest inclusions of TDP-43. Science Advances. 8:eabm6376.

Cavicchi RE, King J, Ripple DC. 2018. Measurement of average aggregate density by sedimentation and Brownian motion analysis. Journal of Pharmaceutical Sciences. 107:1304–1312.

Chen S, Ferrone FA, Wetzel R. 2002. Huntington's disease age-of-onset linked to polyglutamine aggregation nucleation. Proceedings of the National Academy of Sciences of the United States of America. 99:11884–11889.

Chhangani D, Martín-Peña A, Rincon-Limas DE. 2021. Molecular, functional, and pathological aspects of TDP-43 fragmentation. iScience. 24:102459.

Chong PA, Forman-Kay J. 2016. A new phase in ALS research. Structure. 24:1435–1436.

de Boer EMJ, Orie VK, Williams T, Baker MR, De Oliveira HM, Polvikoski T, Silsby M, Menon P, van den Bos M, Halliday GM, van den Berg LH, Van Den Bosch L, van Damme P, Kiernan MC, van Es MA, Vucic S. 2021. TDP-43 proteinopathies: A new wave of neurodegenerative diseases. Journal of Neurology, Neurosurgery & Psychiatry. 92:86–95.

Dong J, Shokes JE, Scott RA, Lynn DG. 2006. Modulating amyloid self-assembly and fibril morphology with Zn(II). Journal of the American Chemical Society. 128:3540–3542.

Dumoulin M, Kumita JR, Dobson CM. 2006. Normal and aberrant biological self-assembly: Insights from studies of human lysozyme and its amyloidogenic variants. Accounts of Chemical Research. 39:603–610.

Fang Y, Tsai K, Chang Y, Kao P, Woods R, Kuo P, Wu C, Liao J, Chou S, Lin V, Jin L, Yuan HS, Cheng IH, Tu P, Chen Y. 2014. Full-length TDP-43 forms toxic amyloid oligomers that are present in frontotemporal lobar dementia-TDP patients. Nature Communications. 5:4824.

Fink AL. 2006. The aggregation and fibrillation of alpha-synuclein. Accounts of Chemical Research. 39:628–634.

Finke RG, Watzky MA, Whitehead CB. 2020. Response to “particle size is a primary determinant for sigmoidal kinetics of nanoparticle formation: A “disproof” of the Finke–Watzky (F-W) nanoparticle nucleation and growth mechanism”. Chemistry of Materials. 32:3657–3672.

French RL, Grese ZR, Aligireddy H, Dhavale DD, Reeb AN, Kedia N, Kotzbauer PT, Bieschke J, Ayala YM. 2019. Detection of TAR DNA-binding protein 43 (TDP-43) oligomers as initial intermediate species during aggregate formation. The Journal of Biological Chemistry. 294:6696–6709.

Ghailan KY, Akbar NS, Albakri A, Alshehri MM. 2023. Biological analysis of emerging nanoparticles with blood through propagating flow along a plumb porous canal in the occurrence of energy and heat transfer. Surfaces and Interfaces. 40:103013.

Glass JD. 2020. Stathmin-2: Adding another piece to the puzzle of TDP-43 proteinopathies and neurodegeneration. The Journal of Clinical Investigation. 130:5677–5680.

Grossman M, Seeley WW, Boxer AL, Hillis AE, Knopman DS, Ljubenov PA, Miller B, Piguet O, Rademakers R, Whitwell JL, Zetterberg H, van Swieten JC. 2023. Frontotemporal lobar degeneration. Nature Reviews Disease Primers. 9:40.

Hadley KC, Rakhit R, Guo H, Sun Y, Jonkman JEN, McLaurin J, Hazrati L, Emili A, Chakrabartty A. 2015. Determining composition of micron-scale protein deposits in neurodegenerative disease by spatially targeted optical microproteomics. eLife. 4:e09579.

Iashchishyn IA, Sulskis D, Nguyen Ngoc M, Smirnovas V, Morozova-Roche LA. 2017. Finke-Watzky two-step nucleation-autocatalysis model of S100A9 amyloid formation: Protein misfolding as "nucleation" event. ACS Chemical Neuroscience. 8:2152–2158.

Ingólfsson HI, Rizuan A, Liu X, Mohanty P, Souza PCT, Marrink SJ, Bowers MT, Mittal J, Berry J. 2023. Multiscale simulations reveal TDP-43 molecular-level interactions driving condensation. Biophysical Journal. 122:4370–4381.

Ishii T, Kawakami E, Endo K, Misawa H, Watabe K. 2017. Formation and spreading of TDP-43 aggregates in cultured neuronal and glial cells demonstrated by time-lapse imaging. PloS One. 12:e0179375.

Jiang L, Xue W, Hong J, Zhang J, Li M, Yu S, He J, Hu H. 2017. The N-terminal dimerization is required for TDP-43 splicing activity. Scientific Reports. 7:6196.

Jo M, Lee S, Jeon Y, Kim S, Kwon Y, Kim H. 2020. The role of TDP-43 propagation in neurodegenerative diseases: Integrating insights from clinical and experimental studies. Experimental & Molecular Medicine. 52:1652–1662.

Kacser H, Burns JA, Fell DA. 1995. The control of flux. Biochemical Society Transactions. 23:341–366.

Kitamura A, Fujimoto A, Kawashima R, Lyu Y, Sasaki K, Hamada Y, Moriya K, Kurata A, Takahashi K, Brielmann R, Bott LC, Morimoto RI, Kinjo M. 2024. Hetero-oligomerization of TDP-43 carboxy-terminal fragments with cellular proteins contributes to proteotoxicity. Communications Biology. 7:743.

Koehler LC, Grese ZR, Bastos ACS, Mamede LD, Heyduk T, Ayala YM. 2022. TDP-43 oligomerization and phase separation properties are necessary for autoregulation. Frontiers in Neuroscience. 16:818655.

Kuznetsov AV. 2024a. Lewy body radius growth: The hypothesis of the cube root of time dependency. J Theor Biol. 581:111734.

Kuznetsov AV. 2024b. Numerical and analytical simulation of the growth of amyloid-β plaques. ASME Journal of Biomedical Engineering. 146:061004.

Kuznetsov AV. 2025a. A criterion characterizing accumulated neurotoxicity of Aβ oligomers in Alzheimer's disease. Proceedings of the Royal Society A. 481:20240652.

Kuznetsov AV. 2025b. Criterion for assessing accumulated neurotoxicity of alpha-synuclein oligomers in Parkinson's disease. International Journal for Numerical Methods in Biomedical Engineering. 41:e70027.

Kuznetsov IA, Kuznetsov AV. 2019. Investigating sensitivity coefficients characterizing the response of a model of tau protein transport in an axon to model parameters. Computer Methods in Biomechanics and Biomedical Engineering. 22:71–83.

Kuznetsov IA, Kuznetsov AV. 2022. An analytical solution simulating growth of Lewy bodies. Mathematical Medicine and Biology : A Journal of the IMA. 39:299–312.

Lee EB, Porta S, Michael Baer G, Xu Y, Suh E, Kwong LK, Elman L, Grossman M, Lee VM-, Irwin DJ, Van Deerlin VM, Trojanowski JQ. 2017. Expansion of the classification of FTLD-TDP: Distinct pathology associated with rapidly progressive frontotemporal degeneration. Acta Neuropathologica. 134:65–78.

Lee SM, Asress S, Hales CM, Gearing M, Vizcarra JC, Fournier CN, Gutman DA, Chin L, Li L, Glass JD. 2019. TDP-43 cytoplasmic inclusion formation is disrupted in C9orf72-associated amyotrophic lateral sclerosis/frontotemporal lobar degeneration. Brain Communications. 1:fcz014.

Ling S, Albuquerque CP, Han JS, Lagier-Tourenne C, Tokunaga S, Zhou H, Cleveland DW. 2010. ALS-associated mutations in TDP-43 increase its stability and promote TDP-43 complexes with FUS/TLS. Proceedings of the National Academy of Sciences of the United States of America. 107:13318–13323.

Liu R, Yang G, Nonaka T, Arai T, Jia W, Cynader MS. 2013. Reducing TDP-43 aggregation does not prevent its cytotoxicity. Acta Neuropathologica Communications. 1:49.

Lu K, Jacob J, Thiyagarajan P, Conticello VP, Lynn DG. 2003. Exploiting amyloid fibril lamination for nanotube self-assembly. Journal of the American Chemical Society. 125:6391–6393.

Lye YS, Chen Y. 2022. TAR DNA-binding protein 43 oligomers in physiology and pathology. IUBMB Life. 74:794–811.

Maraj EN, Shah SI, Akbar NS, Muhammad T. 2023. Thermally progressive particle-Cu/blood peristaltic transport with mass transfer in a non-uniform wavy channel: Closed-form exact solutions. Alexandria Engineering Journal. 74:453–466.

Meneses A, Koga S, O'Leary J, Dickson DW, Bu G, Zhao N. 2021. TDP-43 pathology in Alzheimer's disease. Molecular Neurodegeneration. 16:84.

Morris AM, Watzky MA, Agar JN, Finke RG. 2008. Fitting neurological protein aggregation kinetic data via a 2-step, minimal/"Ockham's razor" model: The Finke-Watzky mechanism of nucleation followed by autocatalytic surface growth. Biochemistry. 47:2413–2427.

Necarsulmer, J., Simon, J., Evangelista, B., Chen, Y., Tian, X., Nafees, S., Marquez Gonzalez, A., Jiang, H., Wang, P., Ajit, D., Nikolova, V., Harper, K., Ezzell, J., Feng-Chang, Beltran, A., Moy, S., Cohen, T. 2023. RNA-binding deficient TDP-43 drives cognitive decline in a mouse model of TDP-43 proteinopathy. eLife. 12:RP85921.

Noreen SA, Akhtar S. 2023. Metachronal wave form analysis on cilia-driven flow of non-newtonain Phan–Thien–Tanner fluid model: A physiological mathematical model. Proceedings of the Institution of Mechanical Engineers, Part E: Journal of Process Mechanical Engineering. 237:2567–2573.

Oiwa K, Watanabe S, Onodera K, Iguchi Y, Kinoshita Y, Komine O, Sobue A, Okada Y, Katsuno M, Yamanaka K. 2023. Monomerization of TDP-43 is a key determinant for inducing TDP-43 pathology in amyotrophic lateral sclerosis. Science Advances. 9:eadf6895.

Pérez-Berlanga M, Wiersma VI, Zbinden A, De Vos L, Wagner U, Foglieni C, Mallona I, Betz KM, Cléry A, Weber J, Guo Z, Rigort R, de Rossi P, Manglunia R, Tantardini E, Sahadevan S, Stach O, Hruska-Plochan M, Allain FH, Paganetti P, Polymenidou M. 2023. Loss of TDP-43 oligomerization or RNA binding elicits distinct aggregation patterns. The EMBO Journal. 42:e111719.

Prasad A, Bharathi V, Sivalingam V, Girdhar A, Patel BK. 2019. Molecular mechanisms of TDP-43 misfolding and pathology in amyotrophic lateral sclerosis. Frontiers in Molecular Neuroscience. 12:25.

Scherer NM, Maurel C, Graus MS, McAlary L, Richter G, Radford RAW, Hogan A, Don EK, Lee A, Yerbury J, Francois M, Chung RS, Morsch M. 2024. RNA-binding properties orchestrate TDP-43 homeostasis through condensate formation in vivo. Nucleic Acids Research. 52:5301–5319.

Sher Akbar N, Abouei Mehrizi A, Rafiq M, Bilal Habib M, Muhammad T. 2023. Peristaltic flow analysis of thermal engineering nano model with effective thermal conductivity of different shape nanomaterials assessing variable fluid properties. Alexandria Engineering Journal. 81:395–404.

Sode K, Usuzaka E, Kobayashi N, Ochiai S. 2005. Engineered alpha-synuclein prevents wild type and familial parkin variant fibril formation. Biochemical and Biophysical Research Communications. 335:432–436.

Sugai A, Kato T, Koyama A, Koike Y, Kasahara S, Konno T, Ishihara T, Onodera O. 2018. Robustness and vulnerability of the autoregulatory system that maintains nuclear TDP-43 levels: A trade-off hypothesis for ALS pathology based on *in silico* data. Frontiers in Neuroscience. 12:28.

Suk TR, Rousseaux MWC. 2020. The role of TDP-43 mislocalization in amyotrophic lateral sclerosis. Molecular Neurodegeneration. 15:45–1.

Sun Y, Arslan PE, Won A, Yip CM, Chakrabartty A. 2014. Binding of TDP-43 to the 3′UTR of its cognate mRNA enhances its solubility. Biochemistry. 53:5885–5894.

Sun Y, Medina Cruz A, Hadley KC, Galant NJ, Law R, Vernon RM, Morris VK, Robertson J, Chakrabartty A. 2019. Physiologically important electrolytes as regulators of TDP-43 aggregation and droplet-phase behavior. Biochemistry. 58:590–607.

Vestergaard M, Kerman K, Saito M, Nagatani N, Takamura Y, Tamiya E. 2005. A rapid label-free electrochemical detection and kinetic study of Alzheimer's amyloid beta aggregation. Journal of the American Chemical Society. 127:11892–11893.

Watzky MA, Finney EE, Finke RG. 2008. Transition-metal nanocluster size vs formation time and the catalytically effective nucleus number: A mechanism-based treatment. Journal of the American Chemical Society. 130:11959–11969.

Wells C, Brennan S, Keon M, Ooi L. 2021. The role of amyloid oligomers in neurodegenerative pathologies. International Journal of Biological Macromolecules. 181:582–604.

Wetzel R. 2006. Kinetics and thermodynamics of amyloid fibril assembly. Accounts of Chemical Research. 39:671–679.

Xiao S, Sanelli T, Chiang H, Sun Y, Chakrabartty A, Keith J, Rogaeva E, Zinman L, Robertson J. 2015. Low molecular weight species of TDP-43 generated by abnormal splicing form inclusions in amyotrophic lateral sclerosis and result in motor neuron death. Acta Neuropathologica. 130:49–61.

Yang L, Jasiqi Y, Lashuel H. 2024. Recombinant full-length TDP-43 oligomers retain their ability to bind RNAs, are not toxic, and do not seed TDP-43 aggregation in vitro. ACS Chemical Neuroscience. 15:193–204.

Youssef H, Gatto RG, Pham NTT, Petersen RC, Machulda MM, Reichard RR, Dickson DW, Jack CR, Whitwell JL, Josephs KA. 2024. TDP-43 is associated with subiculum and cornu ammonis 1 hippocampal subfield atrophy in primary age-related tauopathy. Journal of Alzheimer's Disease. 99:1023–1032.

Youssef H, Weissmann C, Uruk G, Gatto RG. 2025. Looking into abnormal co-expressions of tau and TDP-43 in the realm of mixed dementia types: A double-punch scenario. Brain Sciences. 15:716.

Zadeh KS, Montas HJ. 2010. A class of exact solutions for biomacromolecule diffusion-reaction in live cells. Journal of Theoretical Biology. 264:914–933.

Zi Z. 2011. Sensitivity analysis approaches applied to systems biology models. IET Systems Biology. 5:336–346.

Zirah S, Kozin SA, Mazur AK, Blond A, Cheminant M, Ségalas-Milazzo I, Debey P, Rebuffat S. 2006. Structural changes of region 1-16 of the Alzheimer disease amyloid beta-peptide upon zinc binding and in vitro aging. The Journal of Biological Chemistry. 281:2151–2161.

Figure captions

Fig. 1. A diagram depicting a neuron with two TDP-43 inclusion bodies of equal size located in the soma. The inclusion bodies shown in Fig. 1 are not drawn to scale. *Figure generated with the aid of servier medical art, licensed under a creative commons attribution 3.0 generic license. http://Smart.servier.com.*

Fig. 2. (a) The radius of the growing inclusion body over time (in years) is shown for three different values of k_1. The model predicts the total volume of all inclusion bodies in the soma as $N_{IB}V_{single}$. Assuming all inclusion bodies have the same volume, the volume of a single inclusion body, denoted by V_{single}, is calculated in Eqs. (24) and (25). To facilitate interpretation, the predicted volume is converted into the radius of a sphere with an equivalent volume. (b) Similar to Fig. 2a, but with a focus on the specific time range of [0, 0.2 years]. The concentration of the misfolded form of TDP-43, [*B*], is obtained by numerically solving Eqs. (4)–(7) with initial conditions (8), while the radius of the inclusion body is calculated using Eq. (27). The approximate solution for the radius is determined using Eq. (28). The presented scenario assumes dysfunctional protein degradation machinery, with $T_{1/2,D} \to \infty$, $T_{1/2,M} \to \infty$, $T_{1/2,B} \to \infty$, and $T_{1/2,I} \to \infty$. The case with $k_2 = 10^{-6}$ μM^{-1} s^{-1}, $k_M = 10^{-4}$ s^{-1}, and $\theta_{1/2,B} = 10^7$ s.

Fig. 3. (a) Accumulated neurotoxicity of pathological TDP-43 oligomers, Ξ, as a function of time (in years). Results are shown for three different values of k_1. (b) Similar to Fig. 3a, but with a focus on the specific time range of [0, 0.12 years]. The numerical solution is obtained by solving Eqs. (4)-(7) with initial conditions (8). The approximate solution is determined using Eq. (21). The presented scenario assumes dysfunctional protein degradation machinery with $T_{1/2,D} \to \infty$, $T_{1/2,M} \to \infty$, and $T_{1/2,B} \to \infty$. The case with $k_2 = 10^{-6}$ μM^{-1} s^{-1}, $k_M = 10^{-4}$ s^{-1}, and $\theta_{1/2,B} = 10^7$ s. Note that the approximate solution does not depend on k_1.

Fig. 4. Accumulated neurotoxicity of pathological TDP-43 oligomers, Ξ, as a function of the growing inclusion body radius, r_{IB}. Results are shown for three different values of k_1. The depicted scenario assumes a finite half-life for TDP-43 dimers, monomers, and pathological TDP-43 oligomers ($T_{1/2,D} \to \infty$, $T_{1/2,M} \to \infty$, and $T_{1/2,B} \to \infty$), as well as an intermediate half-deposition time for free misfolded TDP-43 oligomers into inclusion bodies ($\theta_{1/2,B} = 10^7$ s).

Fig. 5. (a) The radius of the growing inclusion body as a function of time (in years). Results are shown for three different values of k_2. (b) Similar to Fig. 5a, but with a focus on the specific time range of [0, 0.04

years]. The approximate solution is determined using Eq. (28). The presented scenario assumes dysfunctional protein degradation machinery with $T_{1/2,D} \to \infty$, $T_{1/2,M} \to \infty$, and $T_{1/2,B} \to \infty$. The case with $k_1 = 10^{-6}$ s^{-1}, $k_M = 10^{-4}$ s^{-1}, and $\theta_{1/2,B} = 10^7$ s.

Fig. 6. (a) Accumulated neurotoxicity of pathological TDP-43 oligomers, Ξ, as a function of time (in years). Results are shown for three different values of k_2. (b) Similar to Fig. 6a, but with a focus on the specific time range of [0, 0.6 years]. The numerical solution is obtained by solving Eqs. (4)-(7) numerically with initial conditions (8). The approximate solution is determined using Eq. (21). The presented scenario assumes dysfunctional protein degradation machinery with $T_{1/2,D} \to \infty$, $T_{1/2,M} \to \infty$, and $T_{1/2,B} \to \infty$. The case with $k_1 = 10^{-6}$ s^{-1}, $k_M = 10^{-4}$ s^{-1}, and $\theta_{1/2,B} = 10^7$ s. Note that the approximate solution does not depend on k_2.

Fig. 7. (a) The radius of the growing inclusion body as a function of time (in years). The results are displayed for three values of k_M. (b) Similar to Fig. 7a, but with a focus on the specific time range of [0, 0.4 years]. The approximate solution is determined using Eq. (28). The presented scenario assumes dysfunctional protein degradation machinery with $T_{1/2,D} \to \infty$, $T_{1/2,M} \to \infty$, and $T_{1/2,B} \to \infty$. The case with $k_1 = 10^{-6}$ s^{-1}, $k_M = 10^{-4}$ s^{-1}, and $\theta_{1/2,B} = 10^7$ s.

Fig. 8. (a) Accumulated neurotoxicity of pathological TDP-43 oligomers, Ξ, as a function of time (in years). Results are shown for three different values of k_M. (b) Similar to Fig. 8a, but with a focus on the specific time range of [0, 0.4 years]. The numerical solution is obtained by solving Eqs. (4)-(7) numerically with initial conditions (8). The approximate solution is determined using Eq. (21). The presented scenario assumes dysfunctional protein degradation machinery with $T_{1/2,D} \to \infty$, $T_{1/2,M} \to \infty$, and $T_{1/2,B} \to \infty$. The case with $k_1 = 10^{-6}$ s^{-1}, $k_M = 10^{-4}$ s^{-1}, and $\theta_{1/2,B} = 10^7$ s. Note that the approximate solution does not depend on k_M.

Fig. 9. (a) The radius of the growing inclusion body versus time (in years). The results are shown for three values of k_1. (b) Similar to Fig. 9a, but with a focus on the specific time range of [0, 0.04 years]. The presented scenario assumes physiologically relevant values for the half-lives of TDP-43 dimers, monomers, and free misfolded oligomers: $T_{1/2,D} = 4.32 \times 10^4$ s, $T_{1/2,M} = 4.32 \times 10^4$ s, $T_{1/2,B} = 1.30 \times 10^5$ s, and $T_{1/2,I} \to \infty$. The case with $k_2 = 10^{-6}$ μM^{-1} s^{-1}, $k_M = 10^{-4}$ s^{-1}, and $\theta_{1/2,B} = 10^7$ s.

Fig. 10. (a) Accumulated neurotoxicity of pathological TDP-43 oligomers, Ξ, as a function of time (in years). Results are shown for three different values of k_1. (b) Similar to Fig. 10a, but with a focus on the specific time range of [0, 0.04 years]. The numerical solution is obtained by solving Eqs. (4)-(7) numerically with initial conditions (8). The presented scenario assumes physiologically relevant values for the half-lives of TDP-43 dimers, monomers, and free misfolded oligomers: $T_{1/2,D} = 4.32\times10^4$ s, $T_{1/2,M} = 4.32\times10^4$ s, and $T_{1/2,B} = 1.30\times10^5$ s. The case with $k_2 = 10^{-6}$ μM^{-1} s^{-1}, $k_M = 10^{-4}$ s^{-1}, and $\theta_{1/2,B} = 10^7$ s.

Fig. 11. (a) The radius of the growing inclusion body as a function of time (in years). The results are displayed for three values of k_2. (b) Similar to Fig. 11a, but with a focus on the specific time range of [0, 0.04 years]. The presented scenario assumes physiologically relevant values for the half-lives of TDP-43 dimers, monomers, and free misfolded oligomers: $T_{1/2,D} = 4.32\times10^4$ s, $T_{1/2,M} = 4.32\times10^4$ s, $T_{1/2,B} = 1.30\times10^5$ s, and $T_{1/2,I} \to \infty$. The case with $k_1 = 10^{-6}$ s^{-1}, $k_M = 10^{-4}$ s^{-1}, and $\theta_{1/2,B} = 10^7$ s.

Fig. 12. (a) Accumulated neurotoxicity of pathological TDP-43 oligomers, Ξ, as a function of time (in years). Results are shown for three different values of k_2. (b) Similar to Fig. 12a, but with a focus on the specific time range of [0, 0.04 years]. The numerical solution is obtained by solving Eqs. (4)-(7) numerically with initial conditions (8). The presented scenario assumes physiologically relevant values for the half-lives of TDP-43 dimers, monomers, and free misfolded oligomers: $T_{1/2,D} = 4.32\times10^4$ s, $T_{1/2,M} = 4.32\times10^4$ s, and $T_{1/2,B} = 1.30\times10^5$ s. The case with $k_1 = 10^{-6}$ s^{-1}, $k_M = 10^{-4}$ s^{-1}, and $\theta_{1/2,B} = 10^7$ s.

Fig. 13. (a) The radius of the growing inclusion body as a function of time (in years). The results are shown for three different values of k_M. (b) Similar to Fig. 13a, but with a focus on the specific time range of [0, 0.004 years]. The presented scenario assumes physiologically relevant values for the half-lives of TDP-43 dimers, monomers, and free misfolded oligomers: $T_{1/2,D} = 4.32\times10^4$ s, $T_{1/2,M} = 4.32\times10^4$ s, $T_{1/2,B} = 1.30\times10^5$ s, and $T_{1/2,I} \to \infty$. The case with $k_1 = 10^{-6}$ s^{-1}, $k_2 = 10^{-6}$ μM^{-1} s^{-1}, and $\theta_{1/2,B} = 10^7$ s.

Fig. 14. (a) Accumulated neurotoxicity of pathological TDP-43 oligomers, Ξ, as a function of time (in years). Results are shown for three different values of k_M. (b) Similar to Fig. 14a, but with a focus on the specific time range of [0, 0.004 years]. The numerical solution is obtained by solving Eqs. (4)-(7) numerically with initial conditions (8). The presented scenario assumes physiologically relevant values

for the half-lives of TDP-43 dimers, monomers, and free misfolded oligomers: $T_{1/2,D} = 4.32 \times 10^4$ s, $T_{1/2,M} = 4.32 \times 10^4$ s, and $T_{1/2,B} = 1.30 \times 10^5$ s. The case with $k_1 = 10^{-6}$ s^{-1}, $k_2 = 10^{-6}$ μM^{-1} s^{-1}, and $\theta_{1/2,B} = 10^7$ s.

Fig. 15. The dimensionless sensitivity of the inclusion body's radius, r_{IB}, to:

(a) the rate constant associated with the first pseudoelementary step in the F-W model, describing the formation of free misfolded oligomers through nucleation, k_1 (calculated for $k_2 = 10^{-6}$ μM^{-1} s^{-1}, $k_M = 10^{-4}$ s^{-1}, $\theta_{1/2,B} = 10^7$ s for three distinct values of k_1);

(b) the rate constant associated with the second pseudoelementary step in the F-W model, describing the formation of free misfolded oligomers through autocatalytic growth, k_2 (calculated for $k_1 = 10^{-6}$ s^{-1}, $k_M = 10^{-4}$ s^{-1}, $\theta_{1/2,B} = 10^7$ s for three distinct values of k_2);

(c) the rate constant linked to the reaction describing the conversion of TDP-43 dimers into monomers, k_M (calculated for $k_1 = 10^{-6}$ s^{-1}, $k_2 = 10^{-6}$ μM^{-1} s^{-1}, $\theta_{1/2,B} = 10^7$ s for three distinct values of k_M).

Fig. 16. The dimensionless sensitivity of the accumulated neurotoxicity of pathological TDP-43 oligomers, Ξ, to:

(a) the rate constant associated with the first pseudoelementary step in the F-W model, describing the formation of free misfolded oligomers through nucleation, k_1 (calculated for $k_2 = 10^{-6}$ μM^{-1} s^{-1}, $k_M = 10^{-4}$ s^{-1}, $\theta_{1/2,B} = 10^7$ s for three distinct values of k_1);

(b) the rate constant associated with the second pseudoelementary step in the F-W model, describing the formation of free misfolded oligomers through autocatalytic growth, k_2 (calculated for $k_1 = 10^{-6}$ s^{-1}, $k_M = 10^{-4}$ s^{-1}, $\theta_{1/2,B} = 10^7$ s for three distinct values of k_2);

(c) the rate constant linked to the reaction describing the conversion of TDP-43 dimers into monomers, k_M (calculated for $k_1 = 10^{-6}$ s^{-1}, $k_2 = 10^{-6}$ μM^{-1} s^{-1}, $\theta_{1/2,B} = 10^7$ s for three distinct values of k_M).

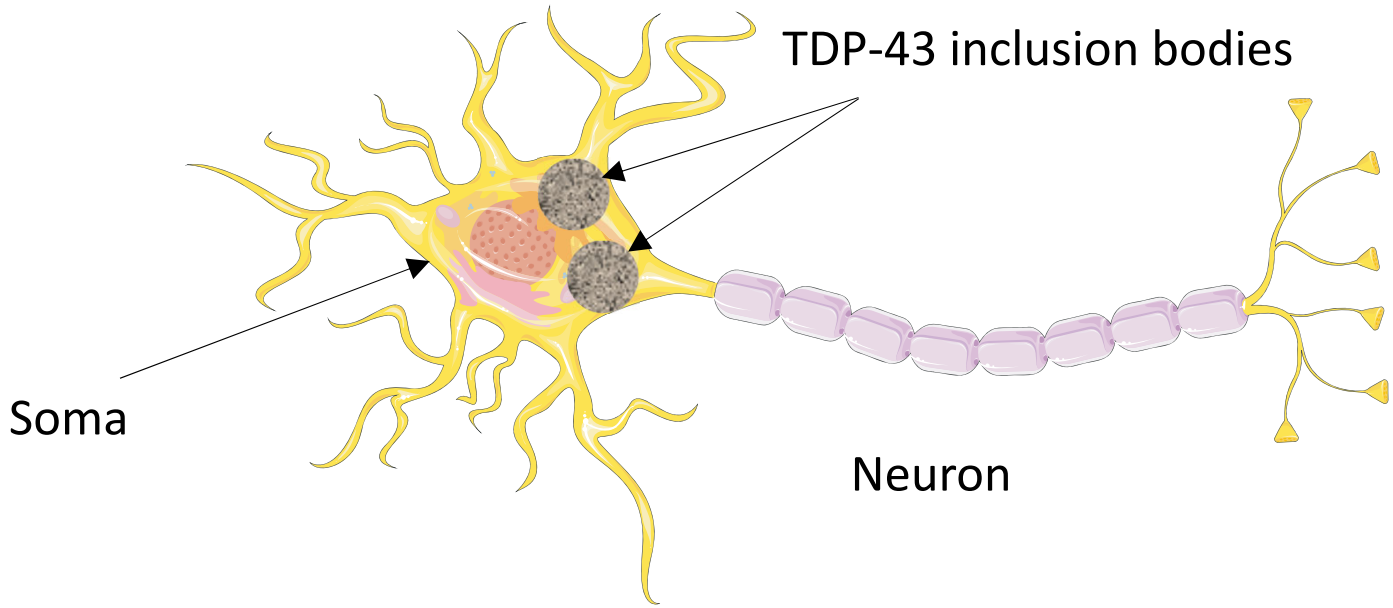

Figure 1

(a)

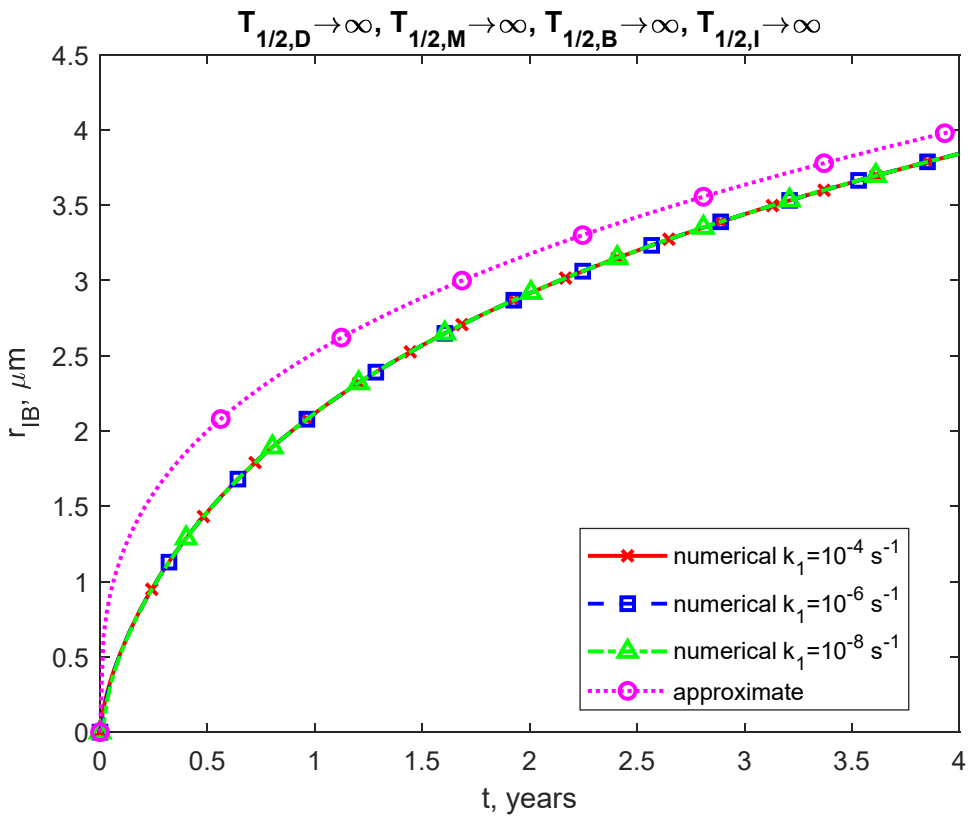
$T_{1/2,D} \to \infty$, $T_{1/2,M} \to \infty$, $T_{1/2,B} \to \infty$, $T_{1/2,I} \to \infty$
r_{IB}, μm
t, years
numerical $k_1=10^{-4}$ s^{-1}
numerical $k_1=10^{-6}$ s^{-1}
numerical $k_1=10^{-8}$ s^{-1}
approximate

(b)

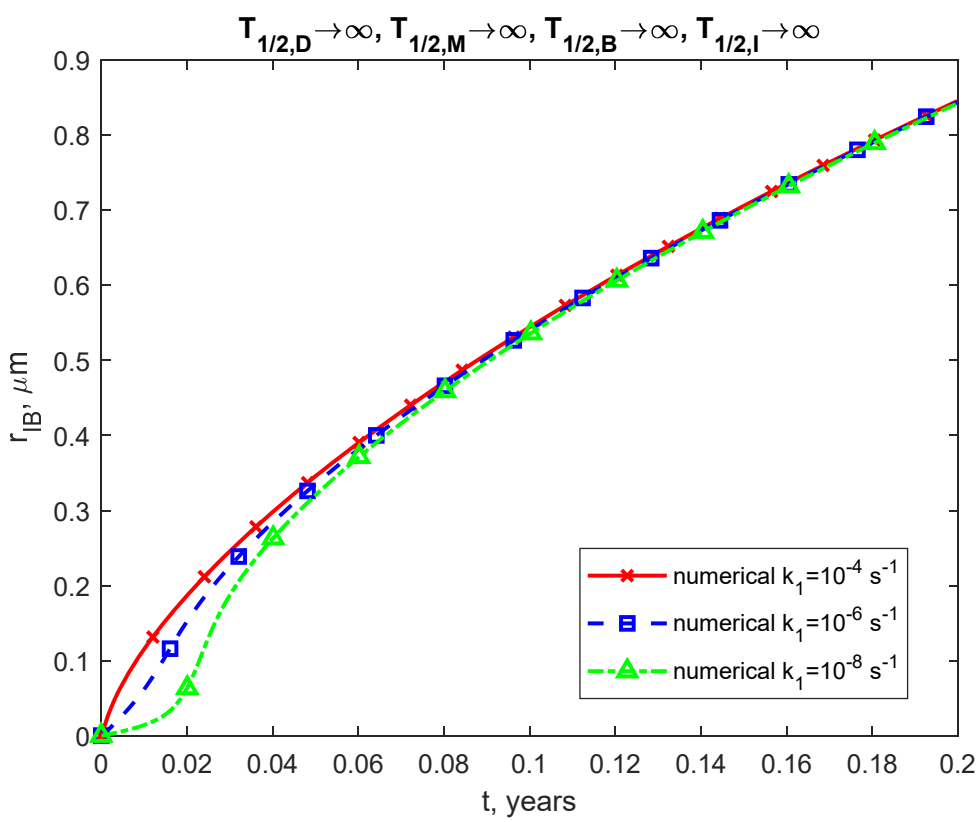
$T_{1/2,D} \to \infty$, $T_{1/2,M} \to \infty$, $T_{1/2,B} \to \infty$, $T_{1/2,I} \to \infty$
r_{IB}, μm
t, years
numerical $k_1=10^{-4}$ s^{-1}
numerical $k_1=10^{-6}$ s^{-1}
numerical $k_1=10^{-8}$ s^{-1}

Figure 2

(a)

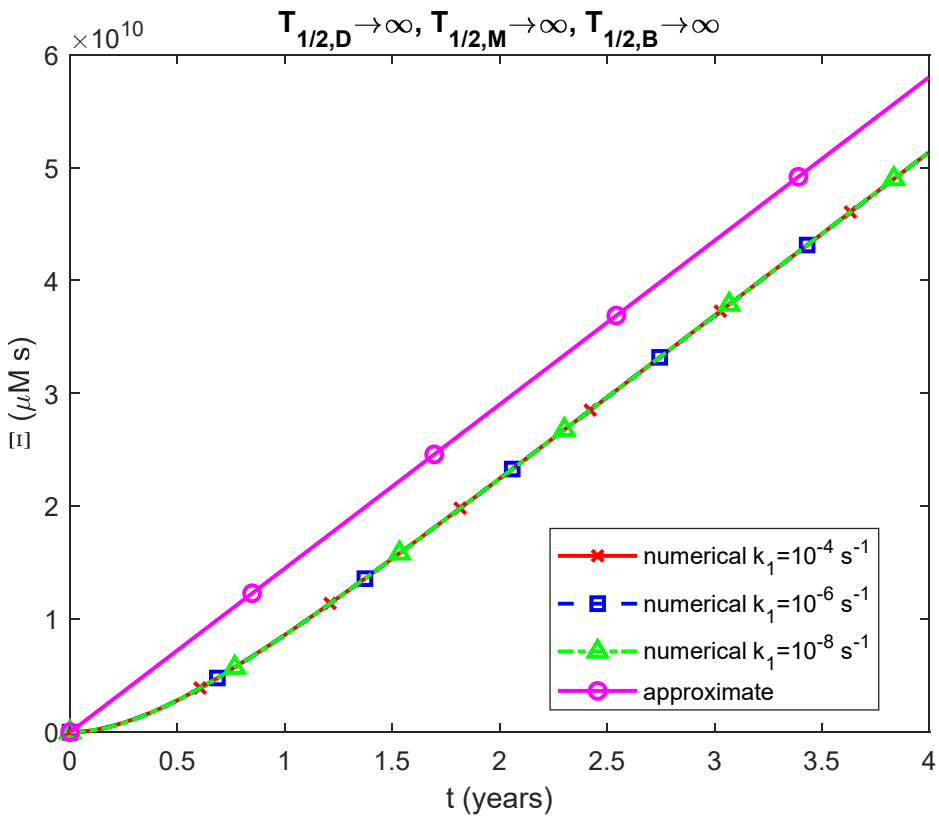
$T_{1/2,D} \to \infty$, $T_{1/2,M} \to \infty$, $T_{1/2,B} \to \infty$
$\times 10^{10}$
[I] (μM s)
t (years)
numerical $k_1=10^{-4}$ s^{-1}
numerical $k_1=10^{-6}$ s^{-1}
numerical $k_1=10^{-8}$ s^{-1}
approximate

(b)

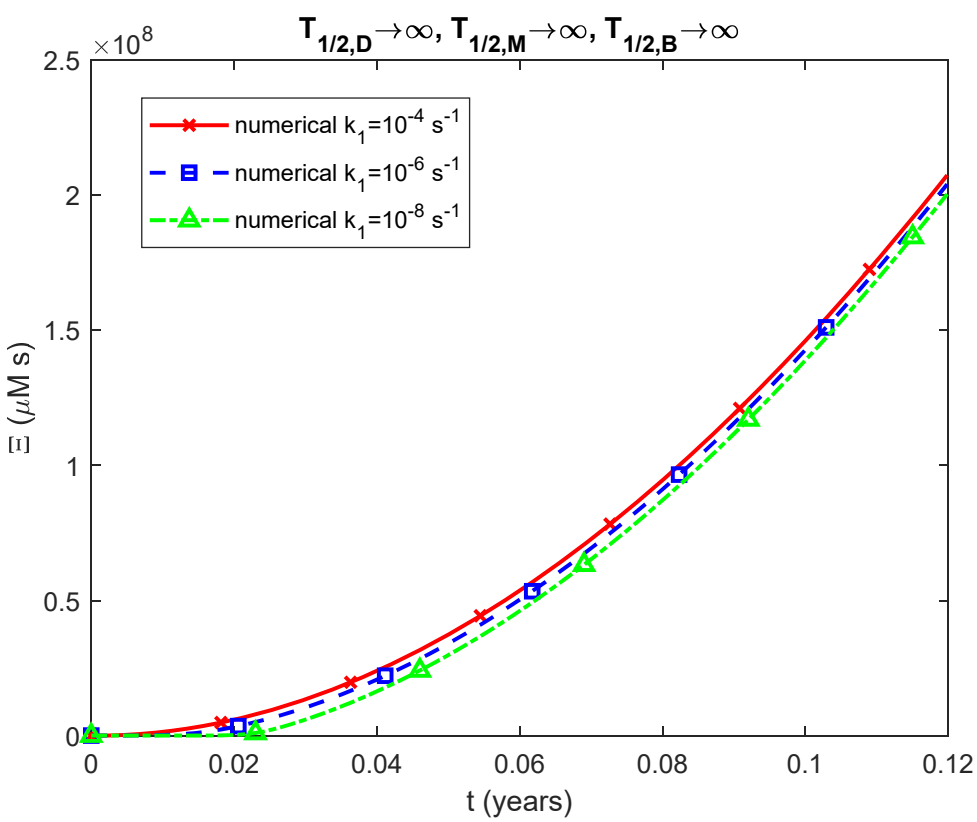
$T_{1/2,D} \to \infty$, $T_{1/2,M} \to \infty$, $T_{1/2,B} \to \infty$
$\times 10^{8}$
[I] (μM s)
t (years)
numerical $k_1=10^{-4}$ s^{-1}
numerical $k_1=10^{-6}$ s^{-1}
numerical $k_1=10^{-8}$ s^{-1}

Figure 3

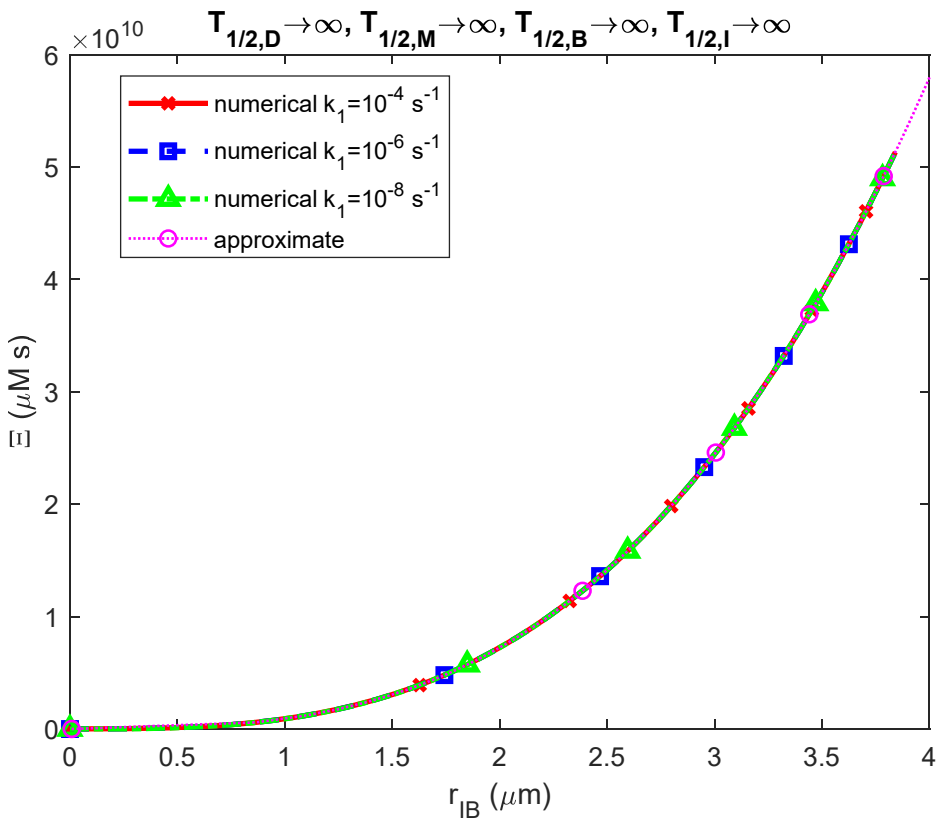
$T_{1/2,D} \to \infty$, $T_{1/2,M} \to \infty$, $T_{1/2,B} \to \infty$, $T_{1/2,I} \to \infty$
$\times 10^{10}$
numerical $k_1=10^{-4}$ s^{-1}
numerical $k_1=10^{-6}$ s^{-1}
numerical $k_1=10^{-8}$ s^{-1}
approximate
[I] (μM s)
r_{IB} (μm)
0
1
2
3
4
5
6
0.5
1.5
2.5
3.5

Figure 4

(a)

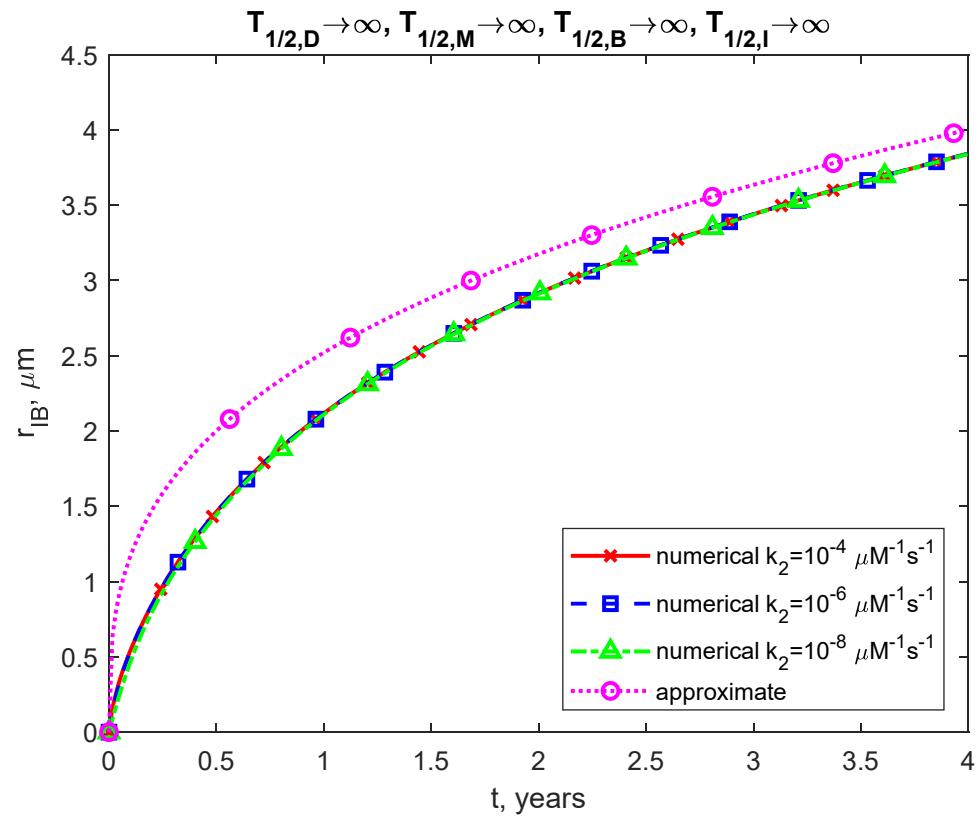
$T_{1/2,D} \to \infty$, $T_{1/2,M} \to \infty$, $T_{1/2,B} \to \infty$, $T_{1/2,I} \to \infty$
r_{IB}, μm
t, years
numerical $k_2=10^{-4}$ $\mu M^{-1}s^{-1}$
numerical $k_2=10^{-6}$ $\mu M^{-1}s^{-1}$
numerical $k_2=10^{-8}$ $\mu M^{-1}s^{-1}$
approximate

(b)

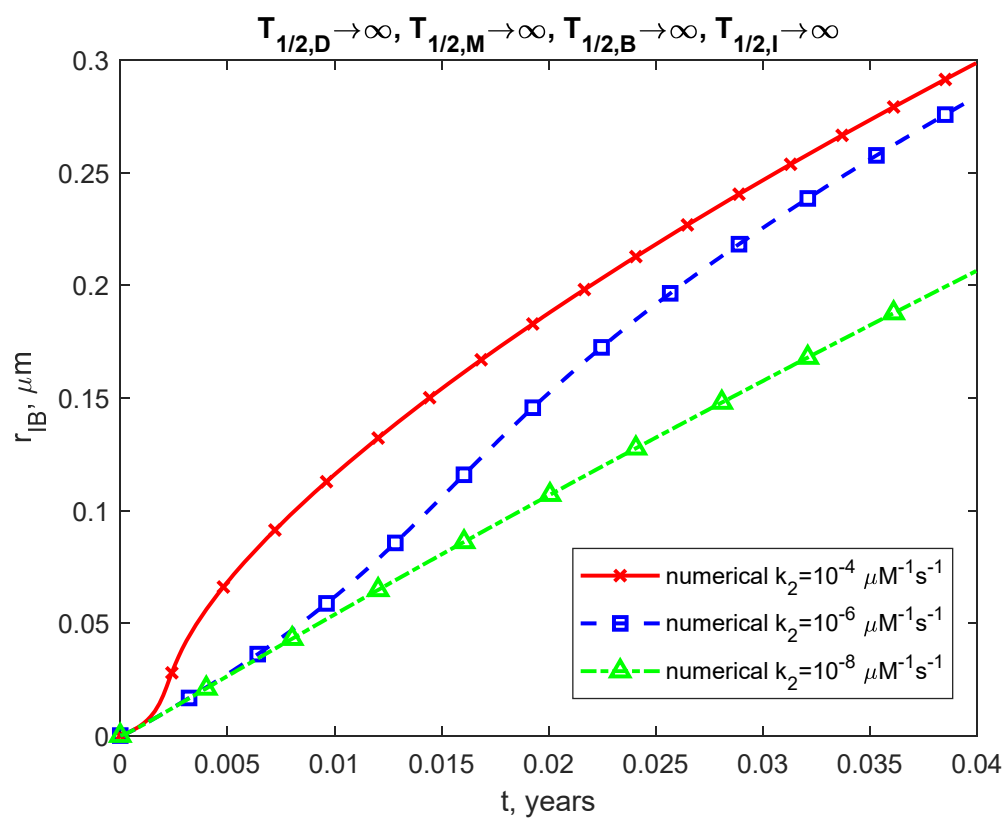
$T_{1/2,D} \to \infty$, $T_{1/2,M} \to \infty$, $T_{1/2,B} \to \infty$, $T_{1/2,I} \to \infty$
r_{IB}, μm
t, years
numerical $k_2=10^{-4}$ $\mu M^{-1}s^{-1}$
numerical $k_2=10^{-6}$ $\mu M^{-1}s^{-1}$
numerical $k_2=10^{-8}$ $\mu M^{-1}s^{-1}$

Figure 5

(a)

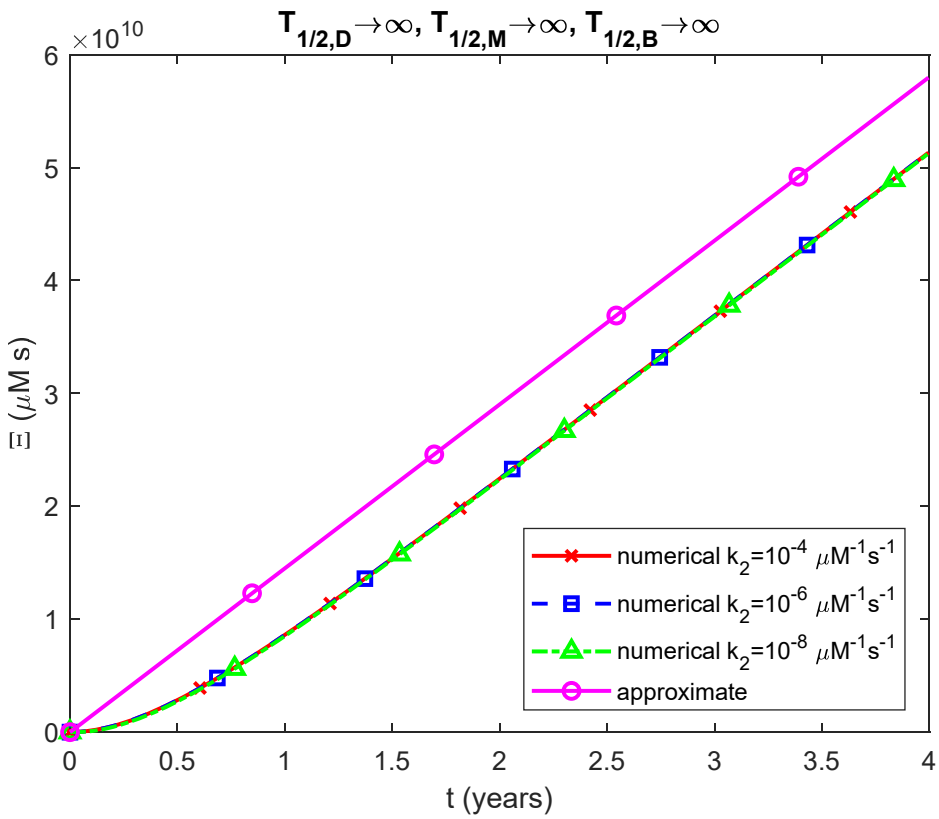
$T_{1/2,D} \to \infty$, $T_{1/2,M} \to \infty$, $T_{1/2,B} \to \infty$
$\times 10^{10}$
[I] (μM s)
t (years)
numerical $k_2=10^{-4}$ $\mu M^{-1}s^{-1}$
numerical $k_2=10^{-6}$ $\mu M^{-1}s^{-1}$
numerical $k_2=10^{-8}$ $\mu M^{-1}s^{-1}$
approximate

(b)

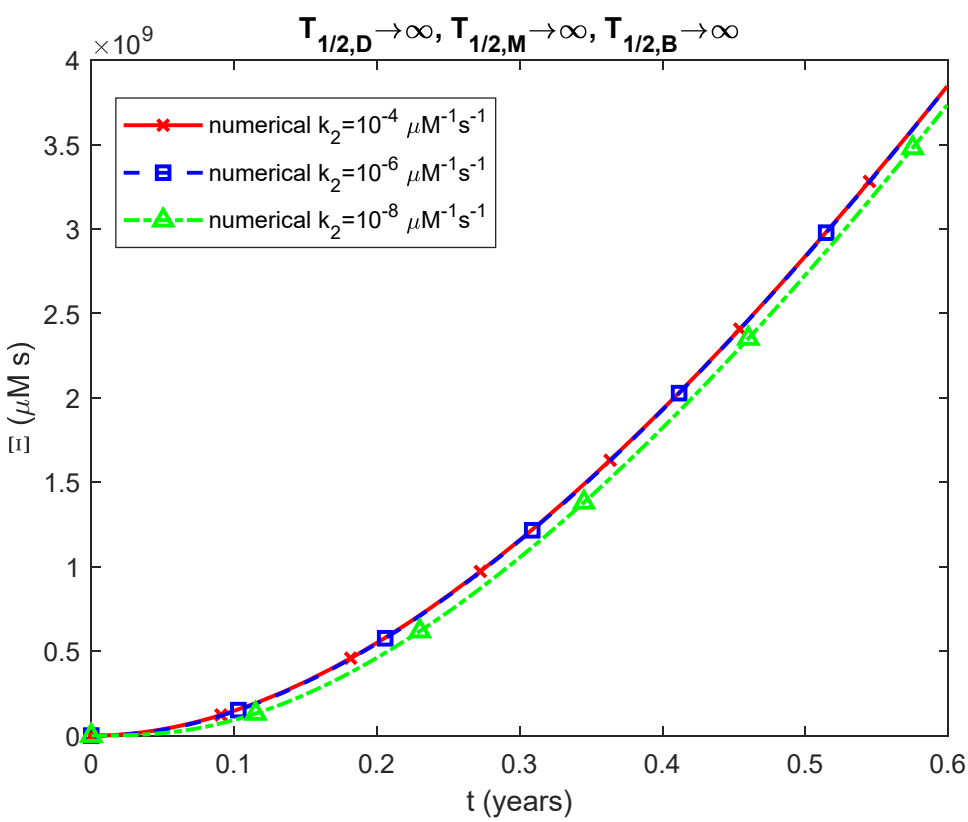
$T_{1/2,D} \to \infty$, $T_{1/2,M} \to \infty$, $T_{1/2,B} \to \infty$
$\times 10^{9}$
[I] (μM s)
t (years)
numerical $k_2=10^{-4}$ $\mu M^{-1}s^{-1}$
numerical $k_2=10^{-6}$ $\mu M^{-1}s^{-1}$
numerical $k_2=10^{-8}$ $\mu M^{-1}s^{-1}$

Figure 6

(a)

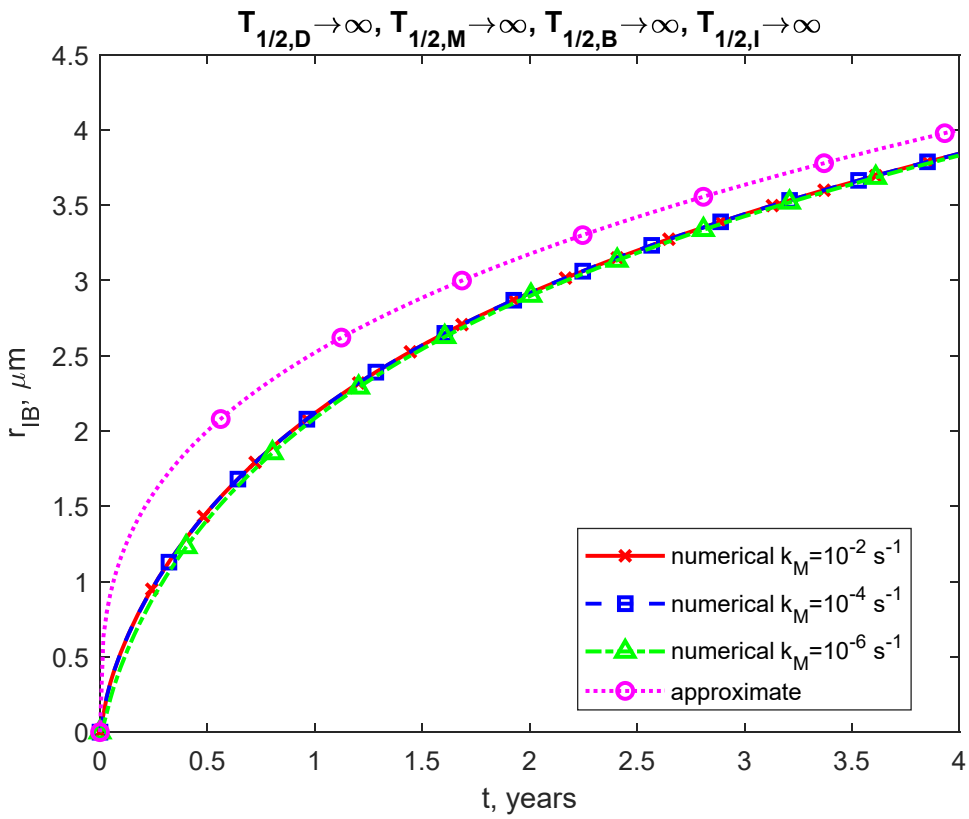
$T_{1/2,D} \to \infty$, $T_{1/2,M} \to \infty$, $T_{1/2,B} \to \infty$, $T_{1/2,I} \to \infty$
r_{IB}, μm
t, years
numerical $k_M=10^{-2}$ s^{-1}
numerical $k_M=10^{-4}$ s^{-1}
numerical $k_M=10^{-6}$ s^{-1}
approximate

(b)

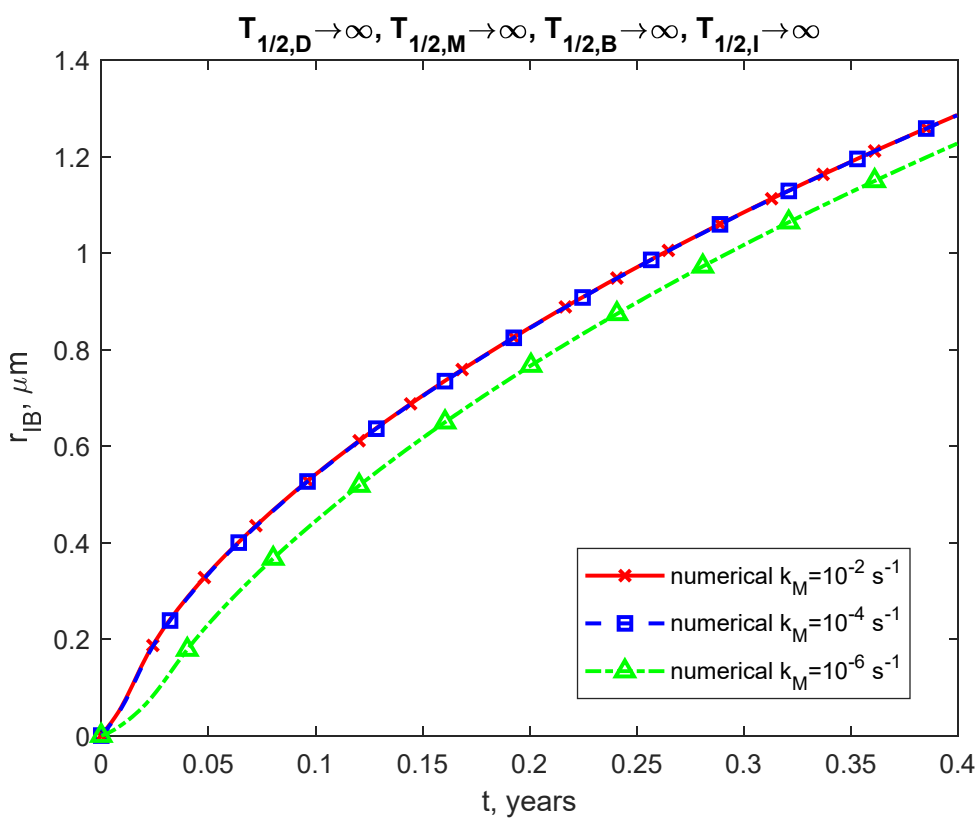
$T_{1/2,D} \to \infty$, $T_{1/2,M} \to \infty$, $T_{1/2,B} \to \infty$, $T_{1/2,I} \to \infty$
r_{IB}, μm
t, years
numerical $k_M=10^{-2}$ s^{-1}
numerical $k_M=10^{-4}$ s^{-1}
numerical $k_M=10^{-6}$ s^{-1}

Figure 7

(a)

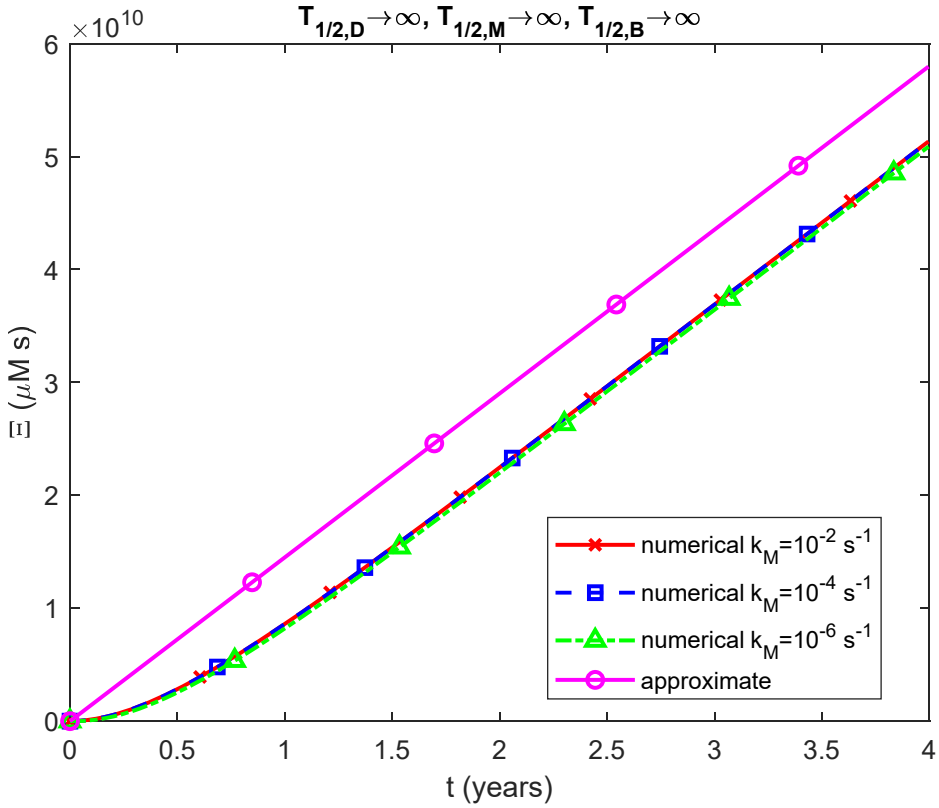
$T_{1/2,D}\to\infty$, $T_{1/2,M}\to\infty$, $T_{1/2,B}\to\infty$
$\times 10^{10}$
[I] (μM s)
t (years)
numerical $k_M=10^{-2}$ s^{-1}
numerical $k_M=10^{-4}$ s^{-1}
numerical $k_M=10^{-6}$ s^{-1}
approximate

(b)

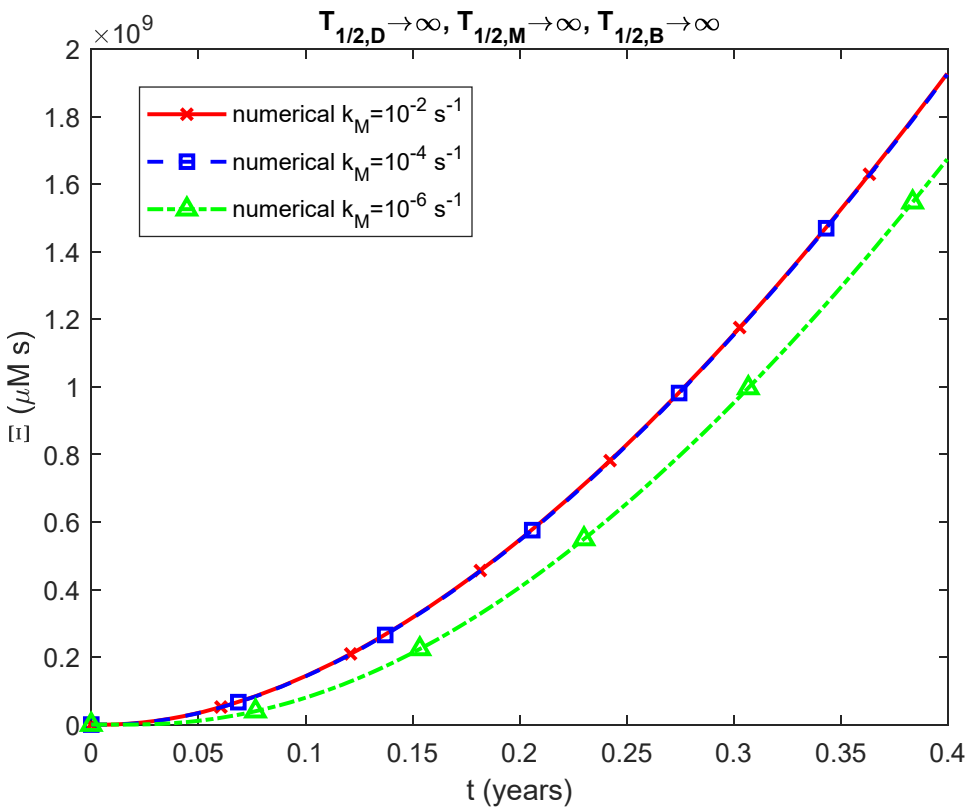
$T_{1/2,D}\to\infty$, $T_{1/2,M}\to\infty$, $T_{1/2,B}\to\infty$
$\times 10^{9}$
[I] (μM s)
t (years)
numerical $k_M=10^{-2}$ s^{-1}
numerical $k_M=10^{-4}$ s^{-1}
numerical $k_M=10^{-6}$ s^{-1}

Figure 8

(a)

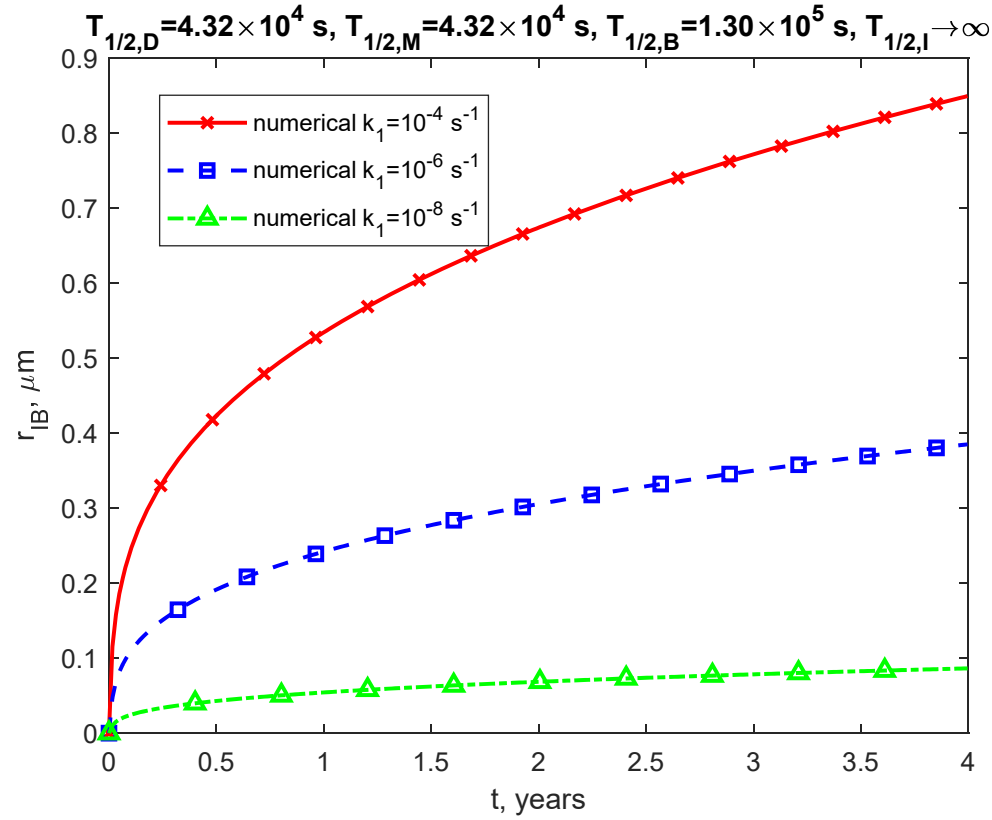
$T_{1/2,D}$=4.32×10^4 s, $T_{1/2,M}$=4.32×10^4 s, $T_{1/2,B}$=1.30×10^5 s, $T_{1/2,I}$→∞
numerical k_1=10^{-4} s^{-1}
numerical k_1=10^{-6} s^{-1}
numerical k_1=10^{-8} s^{-1}
r_{IB}, μm
t, years
0
0.1
0.2
0.3
0.4
0.5
0.6
0.7
0.8
0.9
0.5
1
1.5
2
2.5
3
3.5
4

(b)

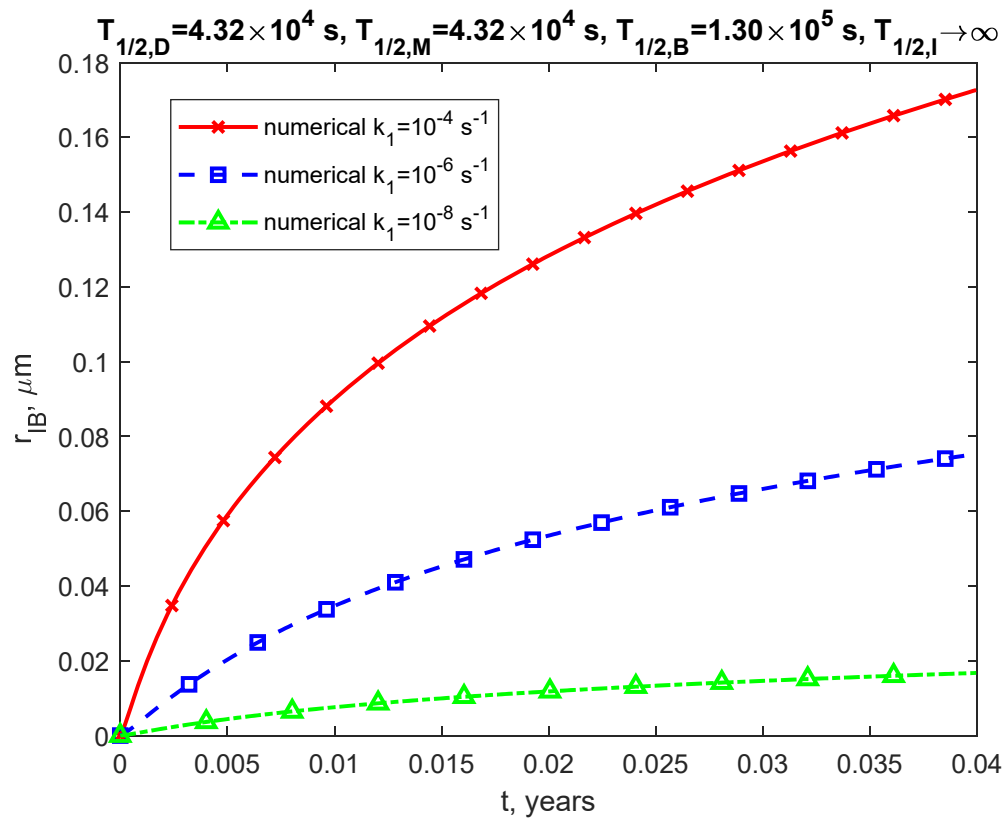
$T_{1/2,D}$=4.32×10^4 s, $T_{1/2,M}$=4.32×10^4 s, $T_{1/2,B}$=1.30×10^5 s, $T_{1/2,I}$→∞
numerical k_1=10^{-4} s^{-1}
numerical k_1=10^{-6} s^{-1}
numerical k_1=10^{-8} s^{-1}
r_{IB}, μm
t, years
0
0.02
0.04
0.06
0.08
0.1
0.12
0.14
0.16
0.18
0.005
0.01
0.015
0.02
0.025
0.03
0.035
0.04

Figure 9

(a)

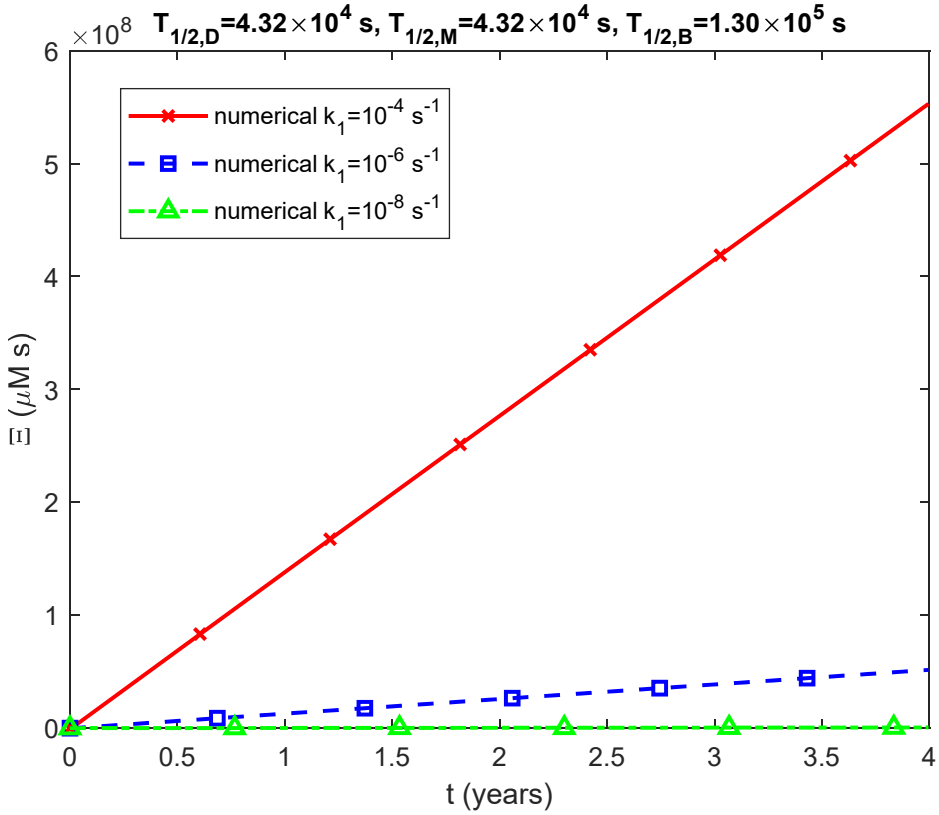
$T_{1/2,D}$=4.32×10^4 s, $T_{1/2,M}$=4.32×10^4 s, $T_{1/2,B}$=1.30×10^5 s
×10^8
numerical k_1=10^-4 s^-1
numerical k_1=10^-6 s^-1
numerical k_1=10^-8 s^-1
[I] (μM s)
t (years)

(b)

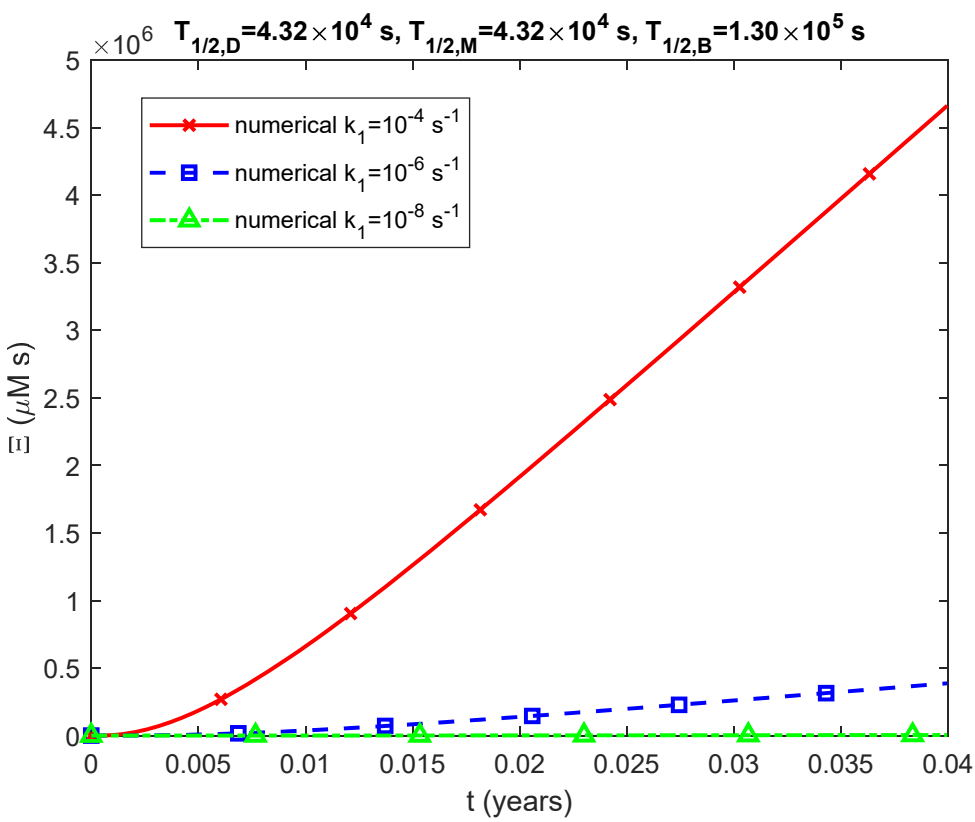
$T_{1/2,D}$=4.32×10^4 s, $T_{1/2,M}$=4.32×10^4 s, $T_{1/2,B}$=1.30×10^5 s
×10^6
numerical k_1=10^-4 s^-1
numerical k_1=10^-6 s^-1
numerical k_1=10^-8 s^-1
[I] (μM s)
t (years)

Figure 10

(a)

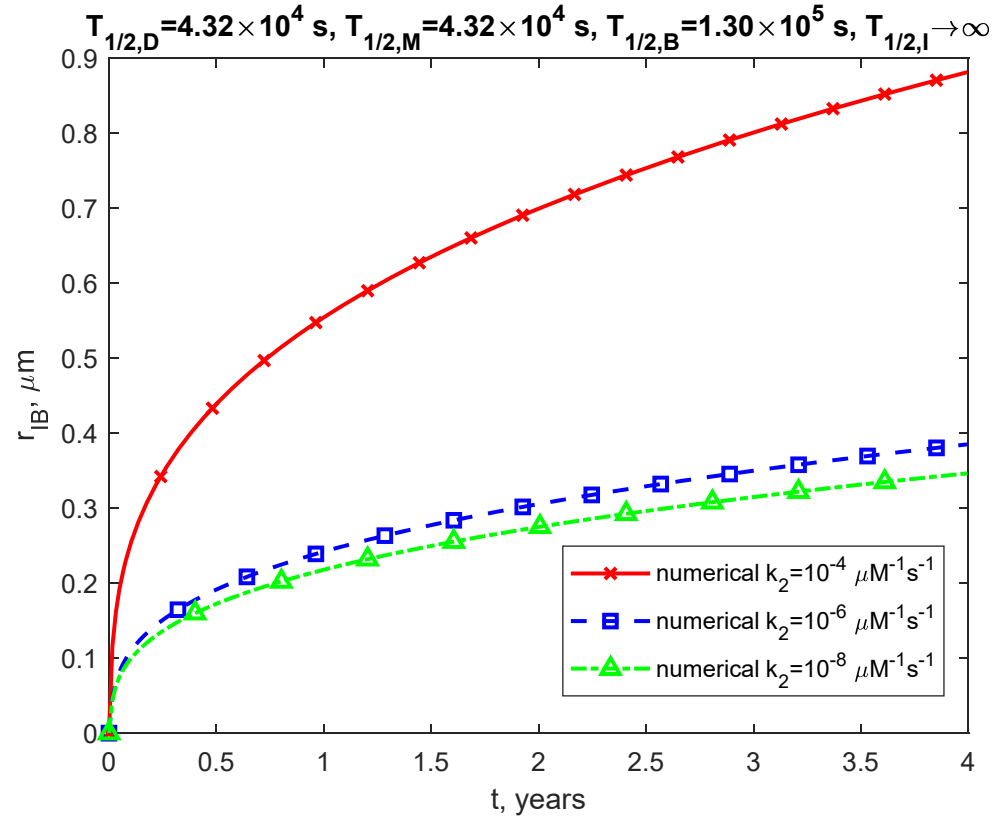
$T_{1/2,D}$=4.32×10^4 s, $T_{1/2,M}$=4.32×10^4 s, $T_{1/2,B}$=1.30×10^5 s, $T_{1/2,I}$→∞
r_{IB}, μm
t, years
numerical k_2=10^{-4} μM^{-1}s^{-1}
numerical k_2=10^{-6} μM^{-1}s^{-1}
numerical k_2=10^{-8} μM^{-1}s^{-1}

(b)

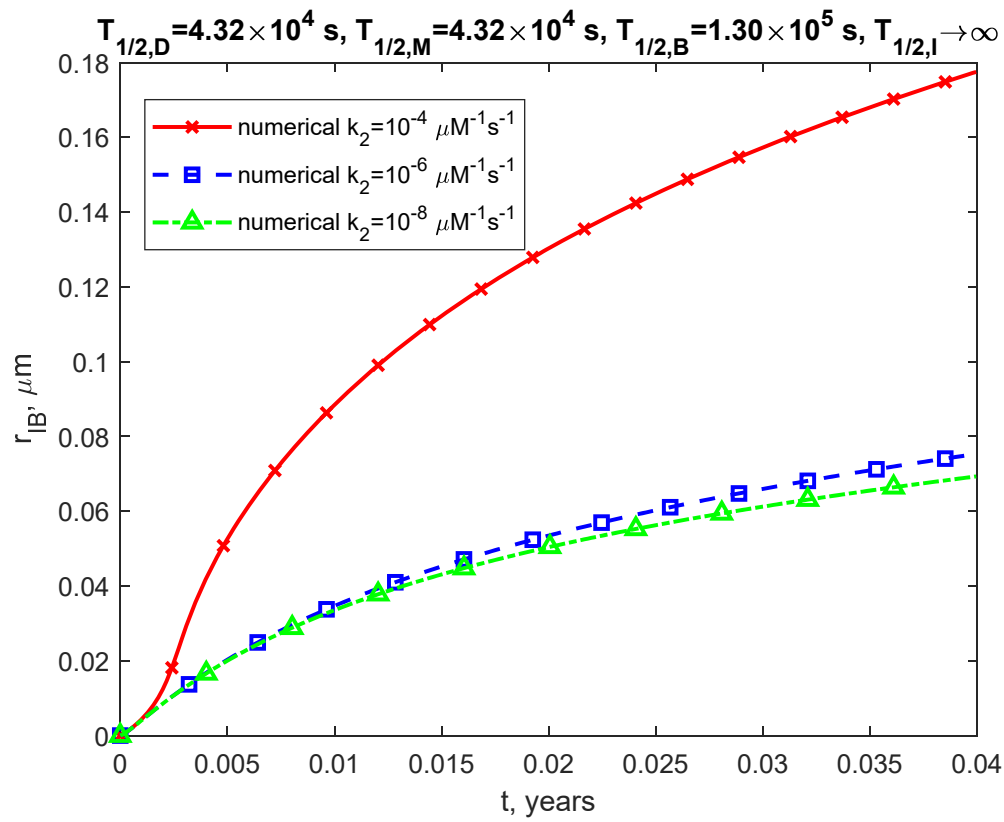
$T_{1/2,D}$=4.32×10^4 s, $T_{1/2,M}$=4.32×10^4 s, $T_{1/2,B}$=1.30×10^5 s, $T_{1/2,I}$→∞
r_{IB}, μm
t, years
numerical k_2=10^{-4} μM^{-1}s^{-1}
numerical k_2=10^{-6} μM^{-1}s^{-1}
numerical k_2=10^{-8} μM^{-1}s^{-1}

Figure 11

(a)

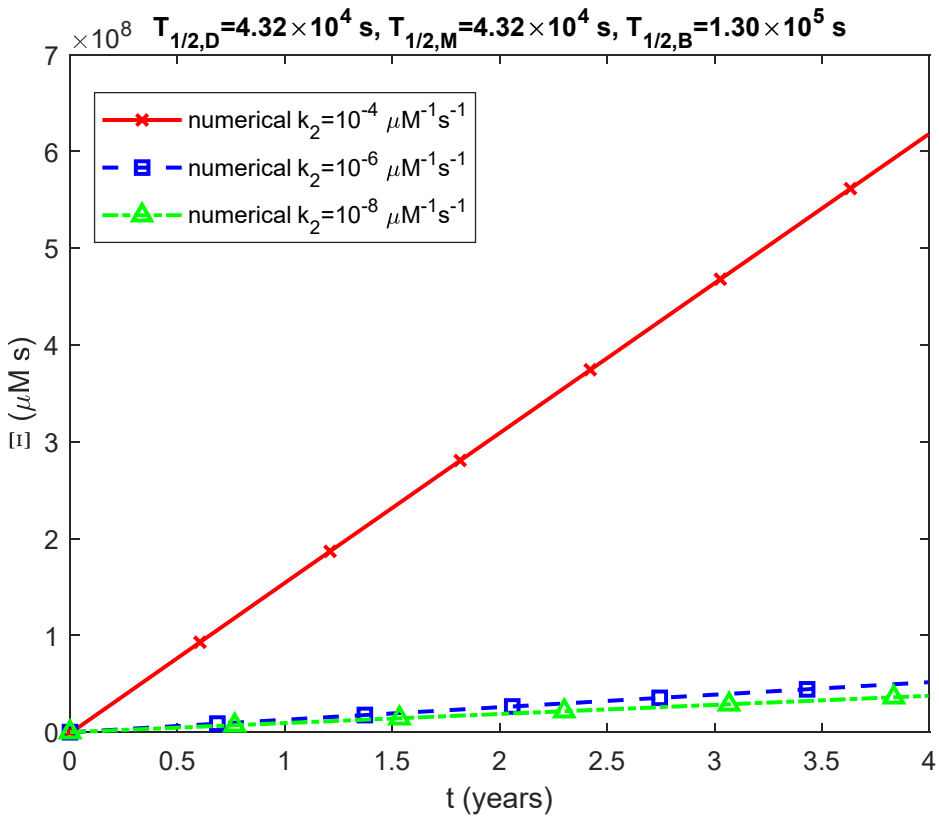
$T_{1/2,D}$=4.32×10^4 s, $T_{1/2,M}$=4.32×10^4 s, $T_{1/2,B}$=1.30×10^5 s
×10^8
numerical k_2=10^-4 μM^-1s^-1
numerical k_2=10^-6 μM^-1s^-1
numerical k_2=10^-8 μM^-1s^-1
[I] (μM s)
t (years)

(b)

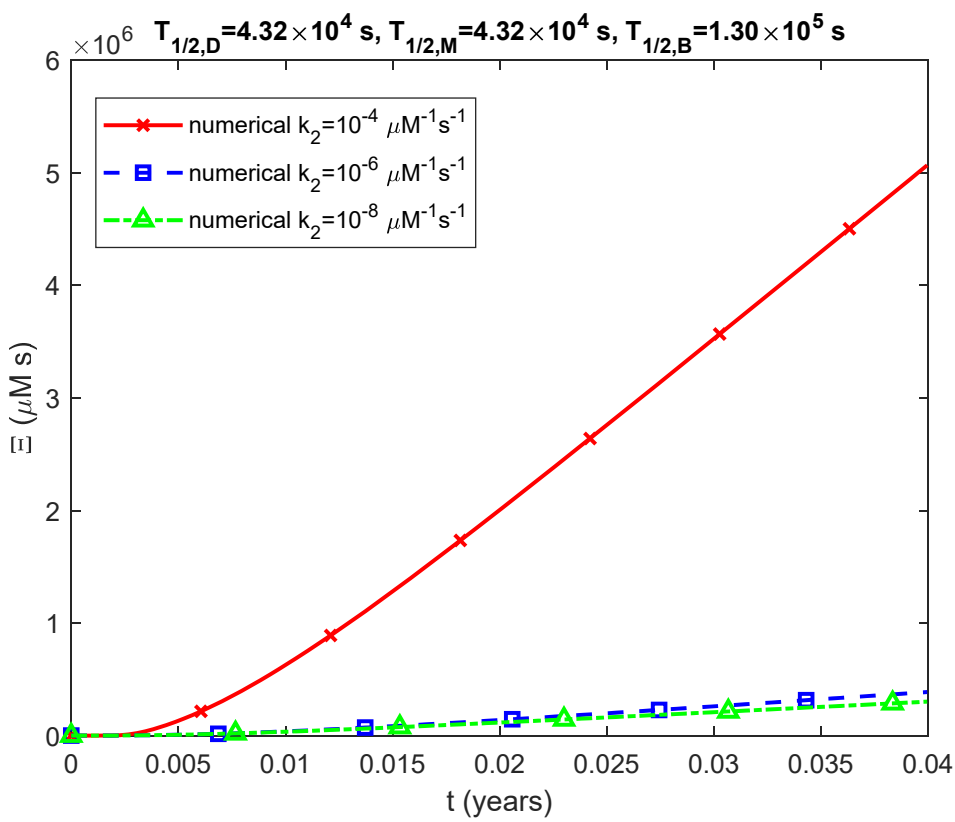
$T_{1/2,D}$=4.32×10^4 s, $T_{1/2,M}$=4.32×10^4 s, $T_{1/2,B}$=1.30×10^5 s
×10^6
numerical k_2=10^-4 μM^-1s^-1
numerical k_2=10^-6 μM^-1s^-1
numerical k_2=10^-8 μM^-1s^-1
[I] (μM s)
t (years)

Figure 12

(a)

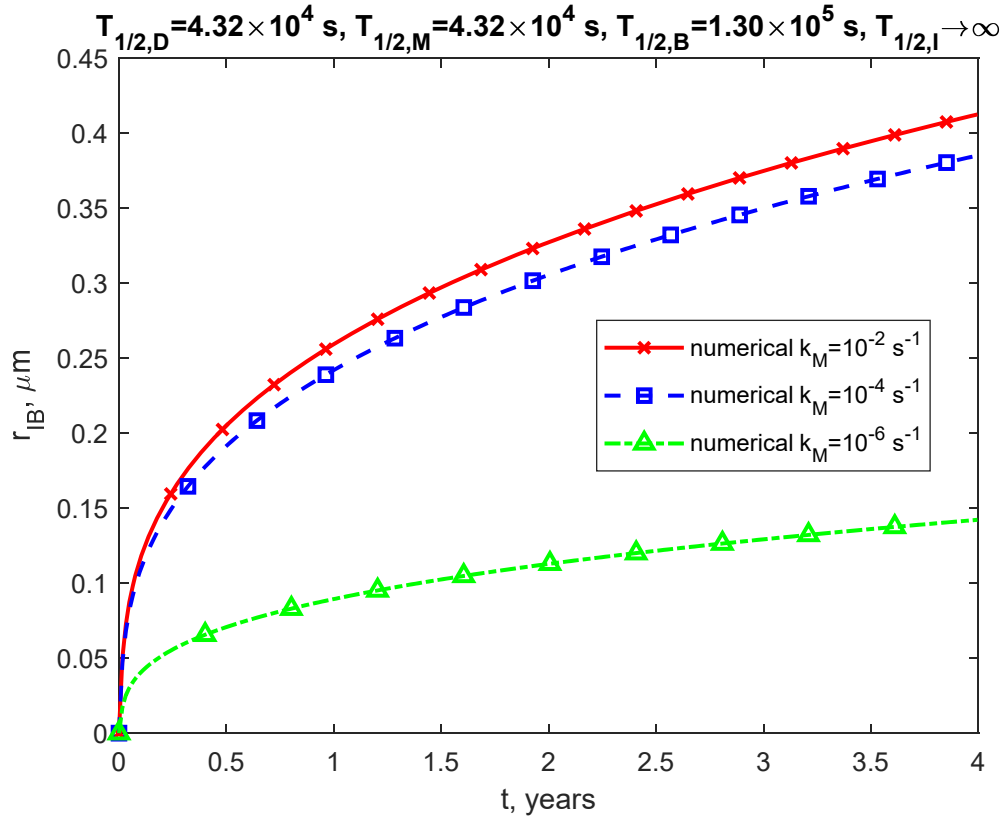
$T_{1/2,D}=4.32\times10^4$ s, $T_{1/2,M}=4.32\times10^4$ s, $T_{1/2,B}=1.30\times10^5$ s, $T_{1/2,I}\to\infty$
numerical $k_M=10^{-2}$ s^{-1}
numerical $k_M=10^{-4}$ s^{-1}
numerical $k_M=10^{-6}$ s^{-1}
r_{IB}, μm
t, years

(b)

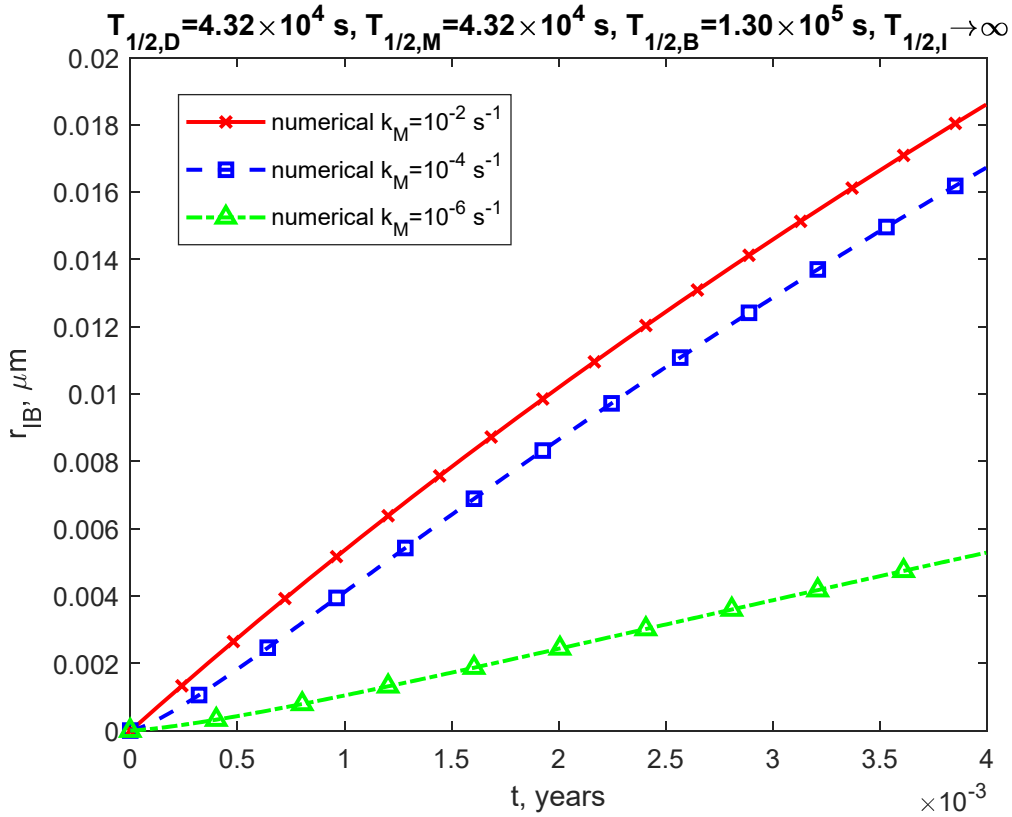
$T_{1/2,D}=4.32\times10^4$ s, $T_{1/2,M}=4.32\times10^4$ s, $T_{1/2,B}=1.30\times10^5$ s, $T_{1/2,I}\to\infty$
numerical $k_M=10^{-2}$ s^{-1}
numerical $k_M=10^{-4}$ s^{-1}
numerical $k_M=10^{-6}$ s^{-1}
r_{IB}, μm
t, years
$\times10^{-3}$

Figure 13

(a)

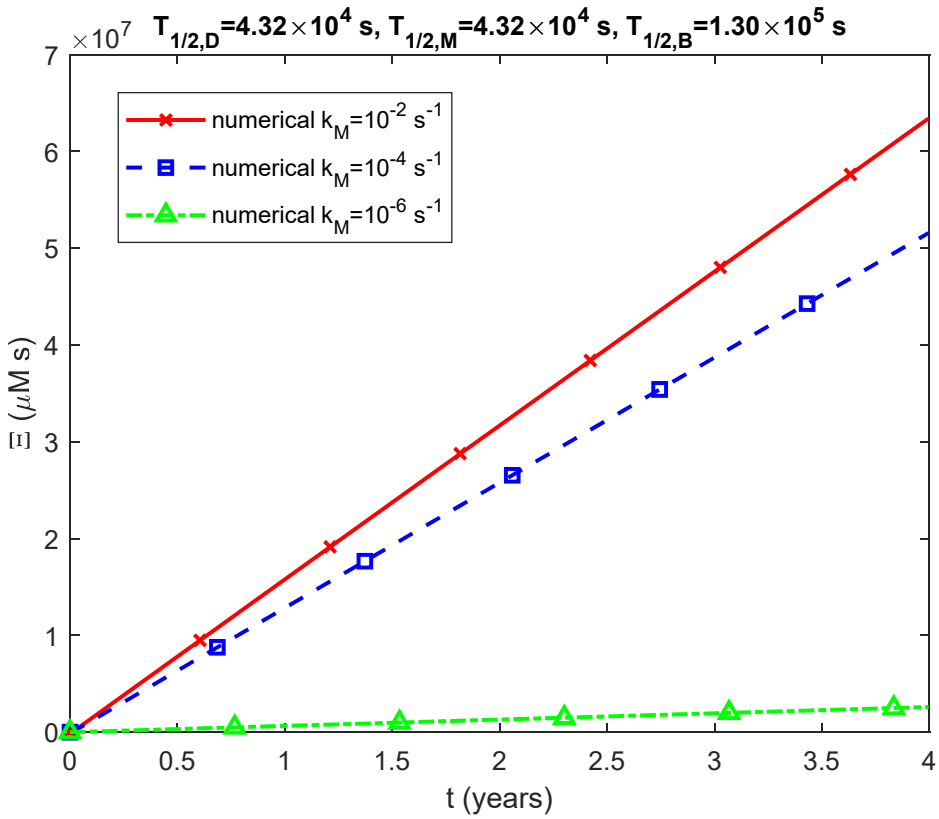
$T_{1/2,D}=4.32\times10^4$ s, $T_{1/2,M}=4.32\times10^4$ s, $T_{1/2,B}=1.30\times10^5$ s
$\times10^7$
numerical $k_M=10^{-2}$ s^{-1}
numerical $k_M=10^{-4}$ s^{-1}
numerical $k_M=10^{-6}$ s^{-1}
[I] (μM s)
t (years)

(b)

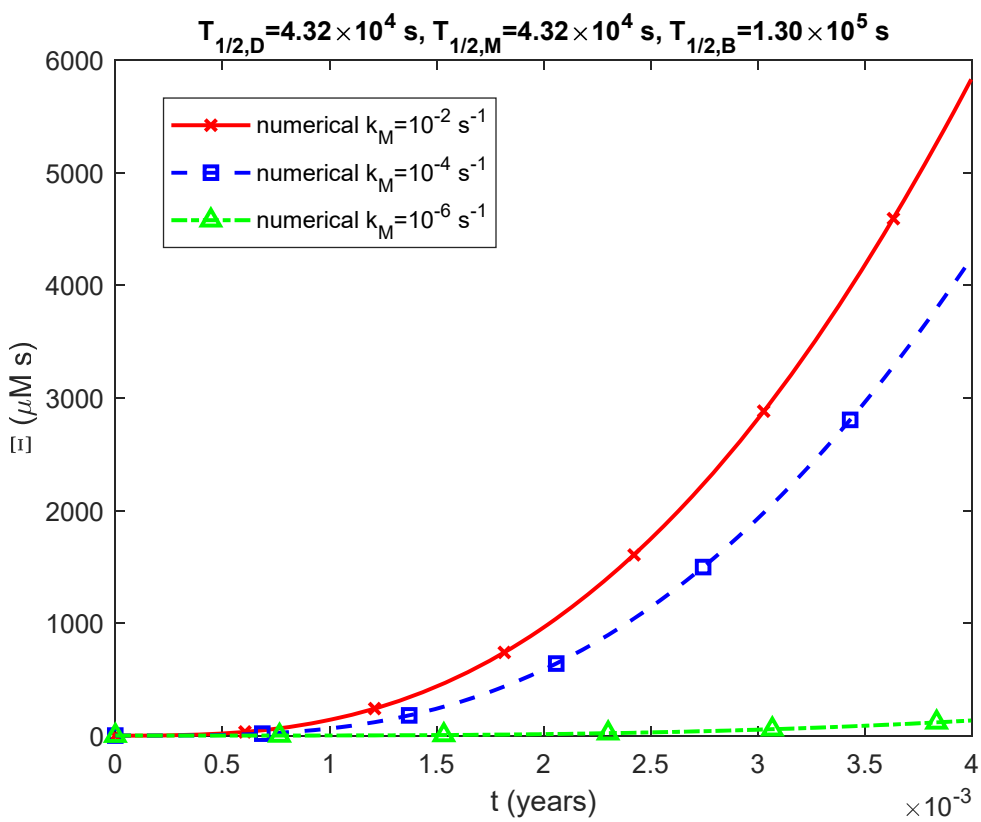
$T_{1/2,D}=4.32\times10^4$ s, $T_{1/2,M}=4.32\times10^4$ s, $T_{1/2,B}=1.30\times10^5$ s
numerical $k_M=10^{-2}$ s^{-1}
numerical $k_M=10^{-4}$ s^{-1}
numerical $k_M=10^{-6}$ s^{-1}
[I] (μM s)
t (years)
$\times10^{-3}$

Figure 14

(a)

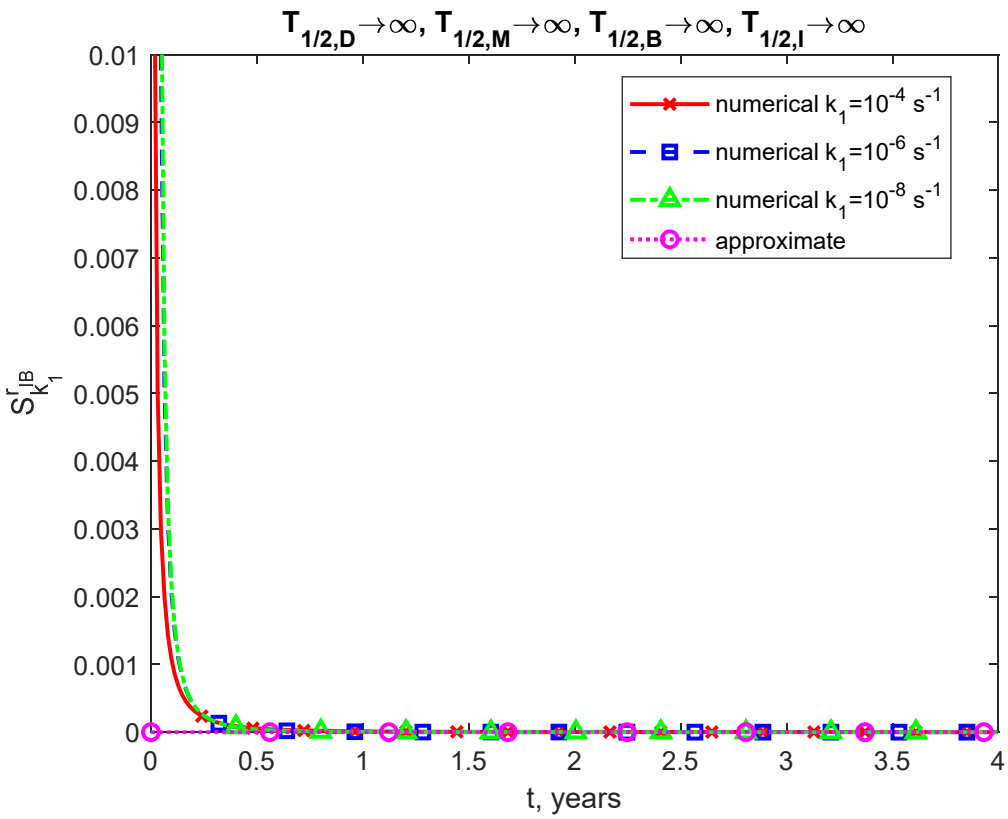

(b)

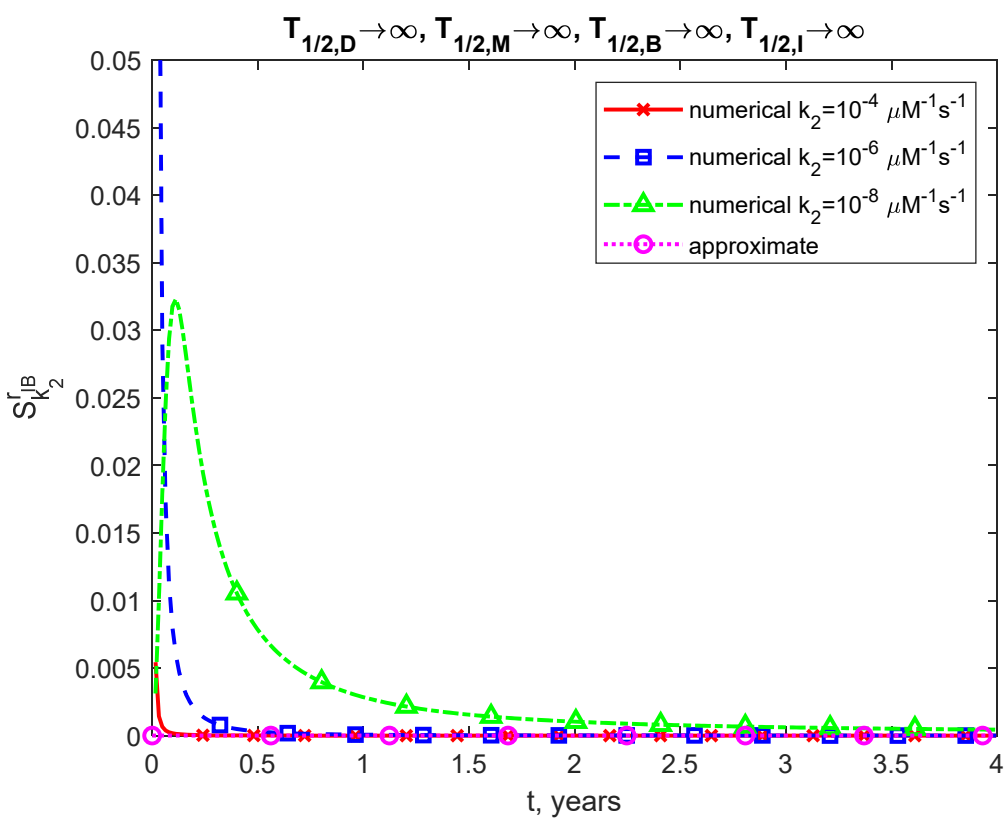

Figure 15a,b

(c)

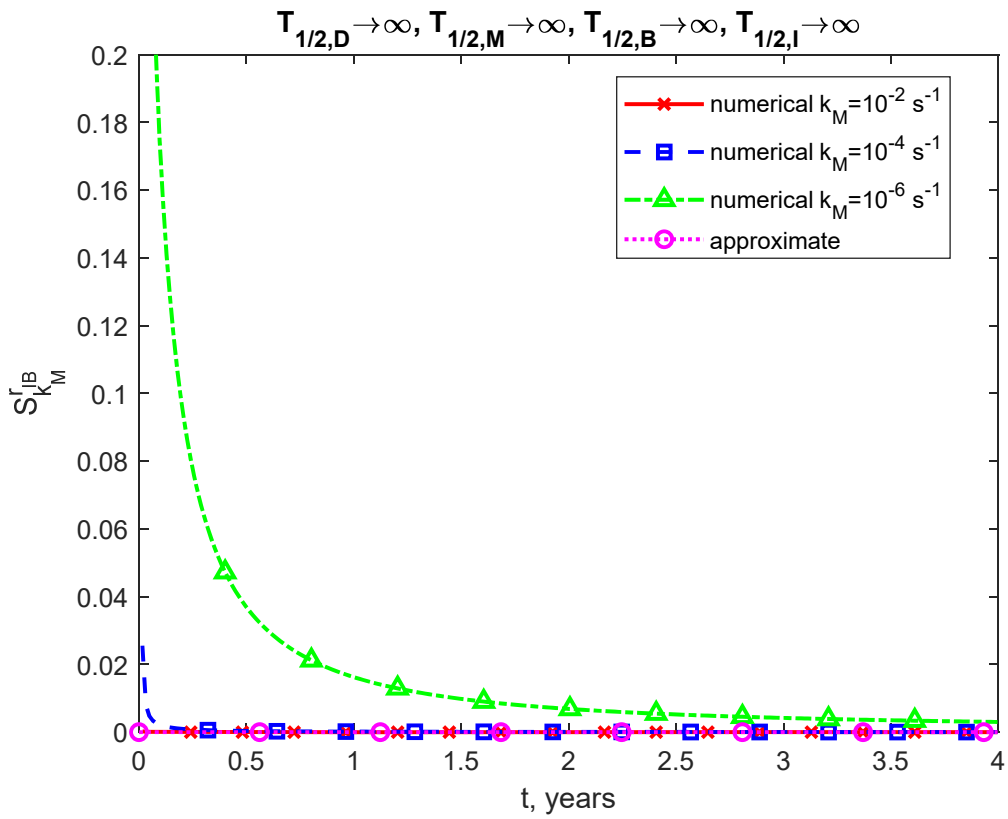
$T_{1/2,D} \to \infty$, $T_{1/2,M} \to \infty$, $T_{1/2,B} \to \infty$, $T_{1/2,I} \to \infty$
numerical $k_M=10^{-2}$ s^{-1}
numerical $k_M=10^{-4}$ s^{-1}
numerical $k_M=10^{-6}$ s^{-1}
approximate
$S^{r_{IB}}_{k_M}$
t, years
0
0.02
0.04
0.06
0.08
0.1
0.12
0.14
0.16
0.18
0.2
0.5
1
1.5
2
2.5
3
3.5
4

Figure 15c

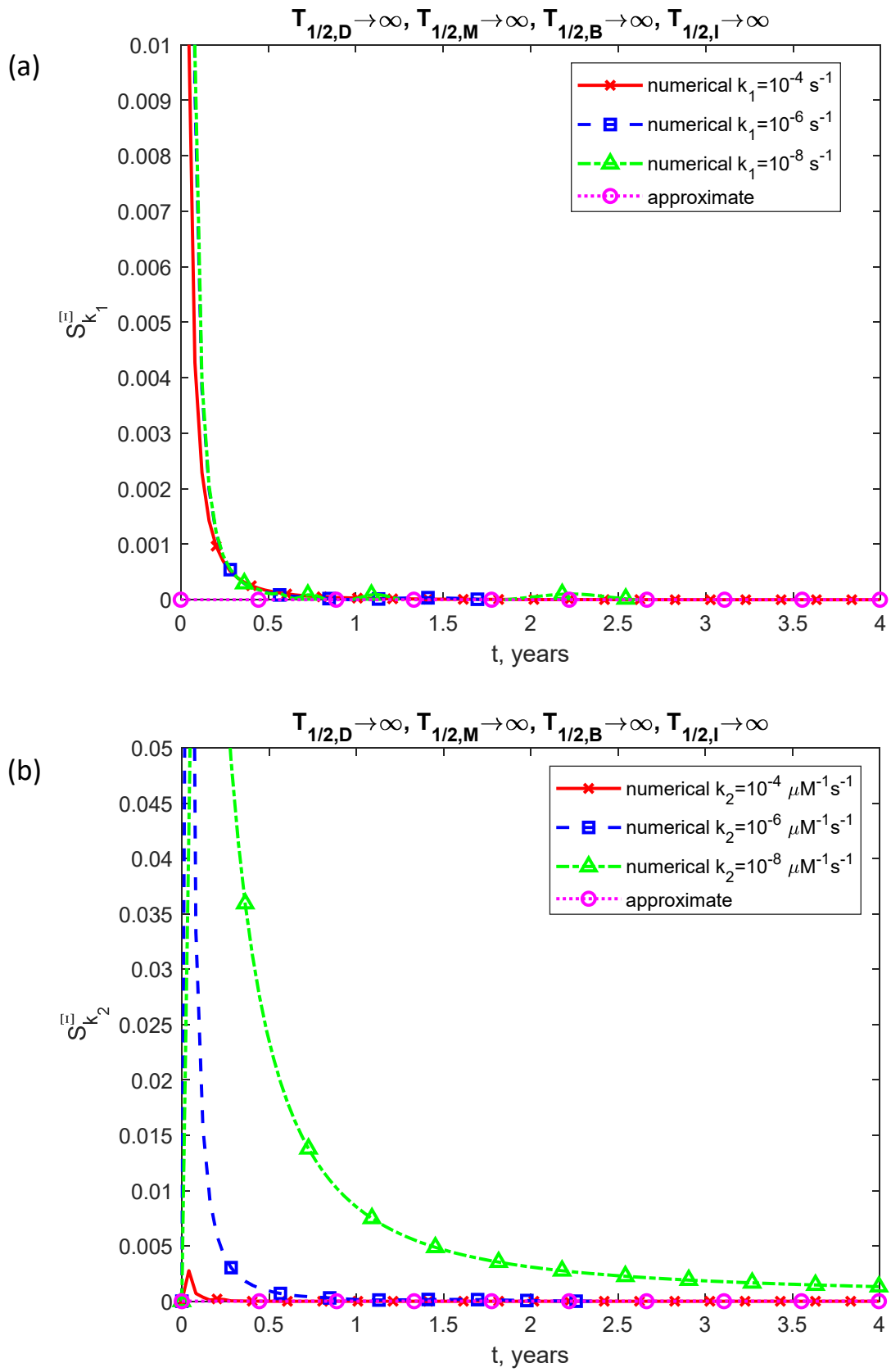
(a)
$T_{1/2,D} \to \infty$, $T_{1/2,M} \to \infty$, $T_{1/2,B} \to \infty$, $T_{1/2,I} \to \infty$
numerical $k_1=10^{-4}$ s^{-1}
numerical $k_1=10^{-6}$ s^{-1}
numerical $k_1=10^{-8}$ s^{-1}
approximate
$S^{[I]}_{k_1}$
t, years
(b)
$T_{1/2,D} \to \infty$, $T_{1/2,M} \to \infty$, $T_{1/2,B} \to \infty$, $T_{1/2,I} \to \infty$
numerical $k_2=10^{-4}$ $\mu M^{-1}s^{-1}$
numerical $k_2=10^{-6}$ $\mu M^{-1}s^{-1}$
numerical $k_2=10^{-8}$ $\mu M^{-1}s^{-1}$
approximate
$S^{[I]}_{k_2}$
t, years

Figure 16a,b

(c)

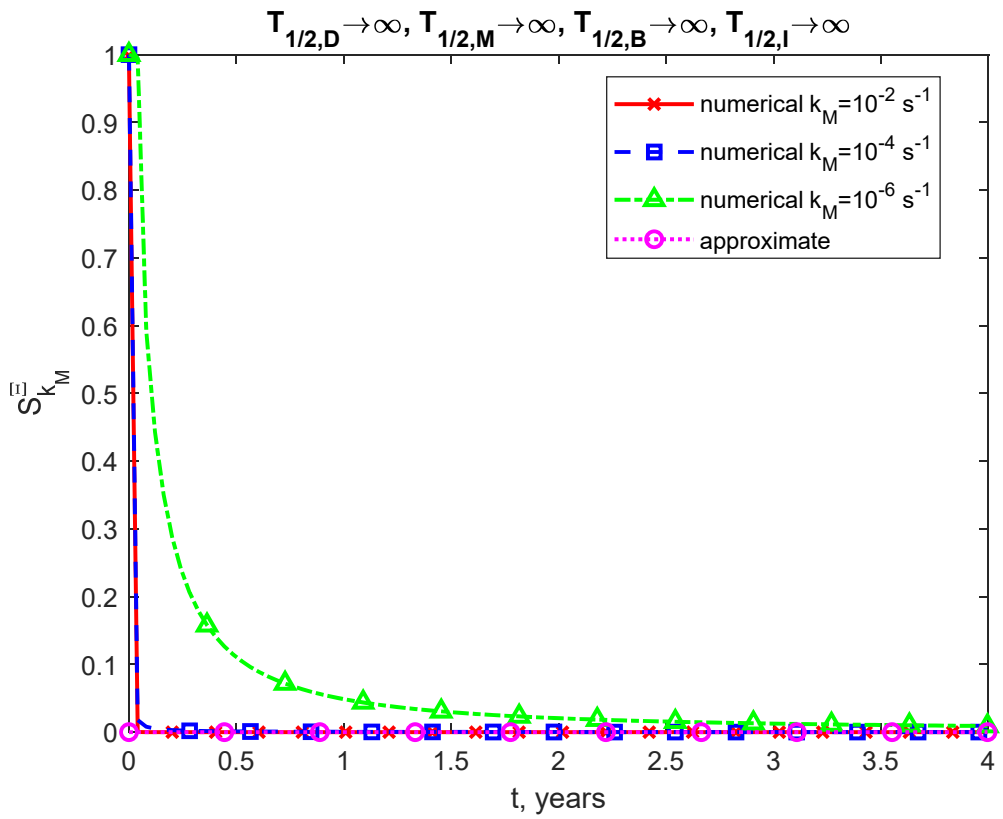
$T_{1/2,D} \to \infty$, $T_{1/2,M} \to \infty$, $T_{1/2,B} \to \infty$, $T_{1/2,I} \to \infty$
numerical $k_M=10^{-2}$ s^{-1}
numerical $k_M=10^{-4}$ s^{-1}
numerical $k_M=10^{-6}$ s^{-1}
approximate
$S_{k_M}^{[I]}$
t, years
0
0.1
0.2
0.3
0.4
0.5
0.6
0.7
0.8
0.9
1
0.5
1.5
2
2.5
3
3.5
4

Figure 16c

Modeling the growth of cytosolic TDP-43 inclusion bodies and accumulated neurotoxicity of misfolded oligomers in neurons

Andrey V. Kuznetsov

Department of Mechanical and Aerospace Engineering, North Carolina State University,

Raleigh, NC 27695-7910, USA; e-mail: avkuznet@ncsu.edu

Supplemental Materials

S1. Supplemental tables

Table S1. Data extracted from Table 2 of Morris et al. (2008), presenting best-fit values of rate constants, k_1 and k_2, used for simulating the aggregation of diverse proteins by the F-W model, $A \xrightarrow{k_1} B$, $A + B \xrightarrow{k_2} 2B$ (A denotes monomers and B denotes aggregates). The data reported in Morris et al. (2008) have been converted into SI units to establish representative ranges for k_1 and k_2. This was done because values for k_1 and k_2 specific to TDP-43 are not available in the literature.

Entry (same as in Morris et al. 2008)	System	k_1, s^{-1}	k_2, μM^{-1} s^{-1}	Reference
1	amyloid β	2.2×10^{-9}	6.4×10^{-7}	Bieschke et al. (2005)
2	amyloid β	1×10^{-4}	1.2×10^{-5}	Vestergaard et al. (2005)
3	amyloid β	1.7×10^{-10}	8.3×10^{-2}	Lu et al. (2003)
4	amyloid β, 1 mM peptide	2.8×10^{-8}	1.6×10^{-2}	Dong et al. (2006)
5	amyloid β, [Zn]:[peptide]= 0.2	2.3×10^{-7}	1.8×10^{-2}	Dong et al. (2006)
6	amyloid β, [Zn]:[peptide]= 0.4	4.4×10^{-8}	1.9×10^{-2}	Dong et al. (2006)
7	amyloid β, Aβ 1-16	8.1×10^{-8}	2.1×10^{-5}	Zirah et al. (2006)
8	amyloid β, Aβ 5-16	2.4×10^{-8}	4.1×10^{-5}	Zirah et al. (2006)
9	α-synuclein	1.1×10^{-8}	1.1×10^{-6}	Fink (2006)
10	α-synuclein	2.8×10^{-7}	3.1×10^{-4}	Sode et al. (2005)
11	polyglutamine	7.2×10^{-7}	6.4×10^{-8}	Chen et al. (2002)
12	polyglutamine	2.8×10^{-7}	3.6×10^{-6}	Wetzel (2006)
13	β-microglobulin	1.7×10^{-13}	1.5×10^{-4}	Ban et al. (2006)

14	D67H lysozyme	3.1×10^{-5}	3.9×10^{-5}	Dumoulin et al. (2006)

S2. Supplemental figures

Figs. S1-S12 and Figs. S13-S24 illustrate the time-dependent concentration profiles of TDP-43 dimers [*D*], monomers [*M*], free misfolded oligomers [*B*], and misfolded TDP-43 oligomers deposited into inclusion bodies [*I*] under different conditions. Figs. S1-S12 depict a situation with infinite half-lives of TDP-43 dimers, monomers, and free misfolded oligomers, while Figs. S13-S24 represent a scenario with physiologically relevant half-lives of these proteins. The numerical solution is obtained by solving Eqs. (4)-(7) numerically with initial conditions (8). The approximate analytical solution depicted in Figs. S1-S12 is computed utilizing Eqs. (14), (16), (17), and (20).

(a)

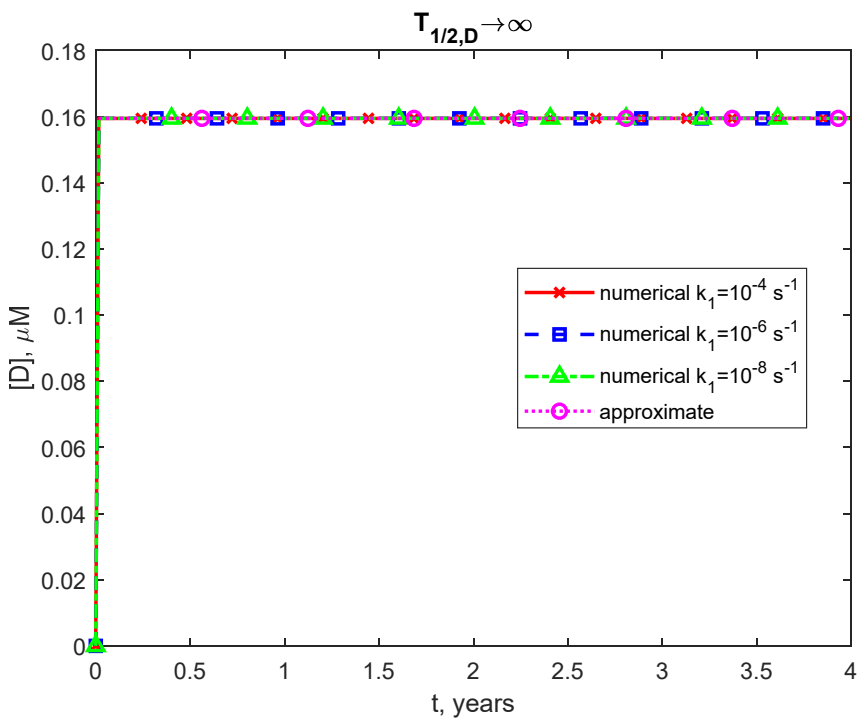

(b)

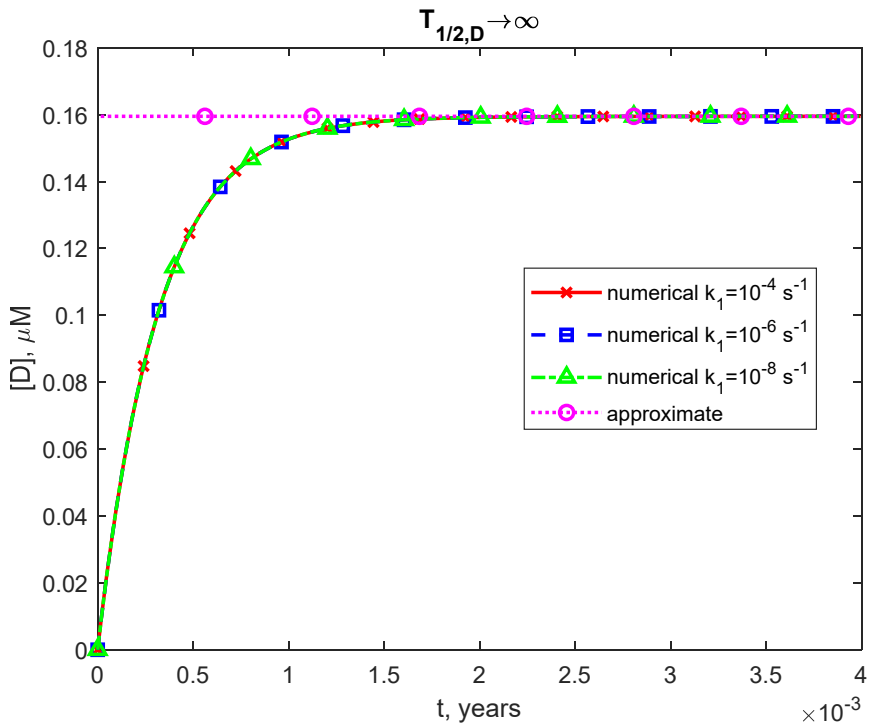

Fig. S1. (a) Molar concentration of TDP-43 dimers, [*D*], as a function of time (in years). (b) Similar to Fig. S1a, but with a focus on the specific time range of [0, 0.004 years] on the *x*-axis. The numerical solution is obtained by solving Eqs. (4)-(7) with initial conditions (8). The approximate solution is determined using Eq. (14). The presented scenario assumes dysfunctional protein degradation machinery with $T_{1/2,D} \to \infty$. The results are shown for three values of k_1. The case with $k_2 = 10^{-6}$ μM^{-1} s^{-1}, $k_M = 10^{-4}$ s^{-1}, and $\theta_{1/2,B} = 10^7$ s.

(a)

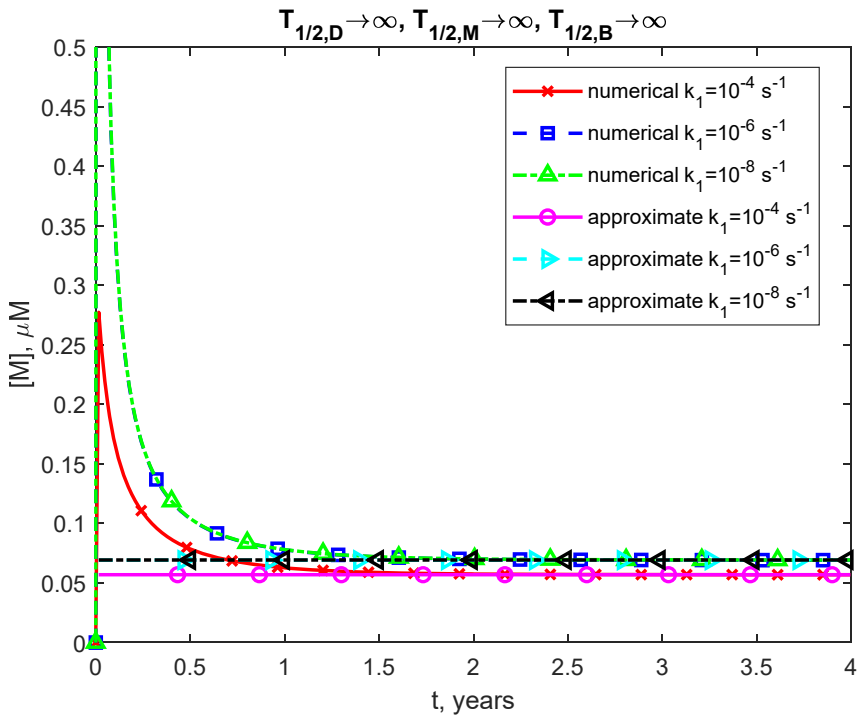

(b)

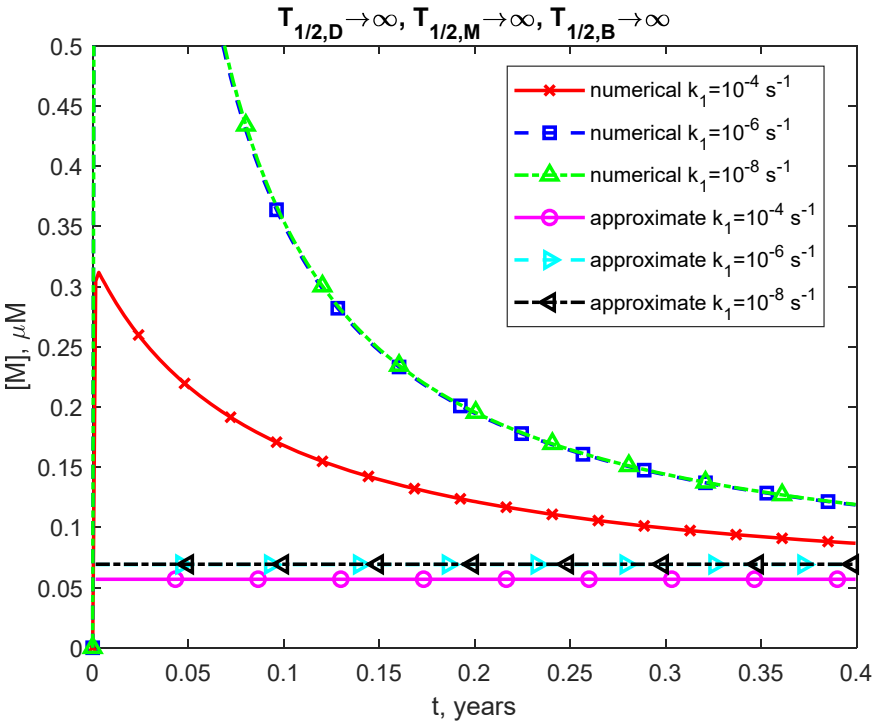

Fig. S2. (a) Molar concentration of TDP-43 monomers, [*M*], as a function of time (in years). (b) Similar to Fig. S2a, but with a focus on the specific time range of [0, 0.4 years] on the *x*-axis. The numerical

solution is obtained by solving Eqs. (4)-(7) with initial conditions (8). The approximate solution is determined using Eq. (17). The presented scenario assumes dysfunctional protein degradation machinery with $T_{1/2,D} \to \infty$, $T_{1/2,M} \to \infty$, and $T_{1/2,B} \to \infty$. The results are shown for three values of k_1. The case with $k_2 = 10^{-6}$ μM^{-1} s^{-1}, $k_M = 10^{-4}$ s^{-1}, and $\theta_{1/2,B} = 10^7$ s.

(a)

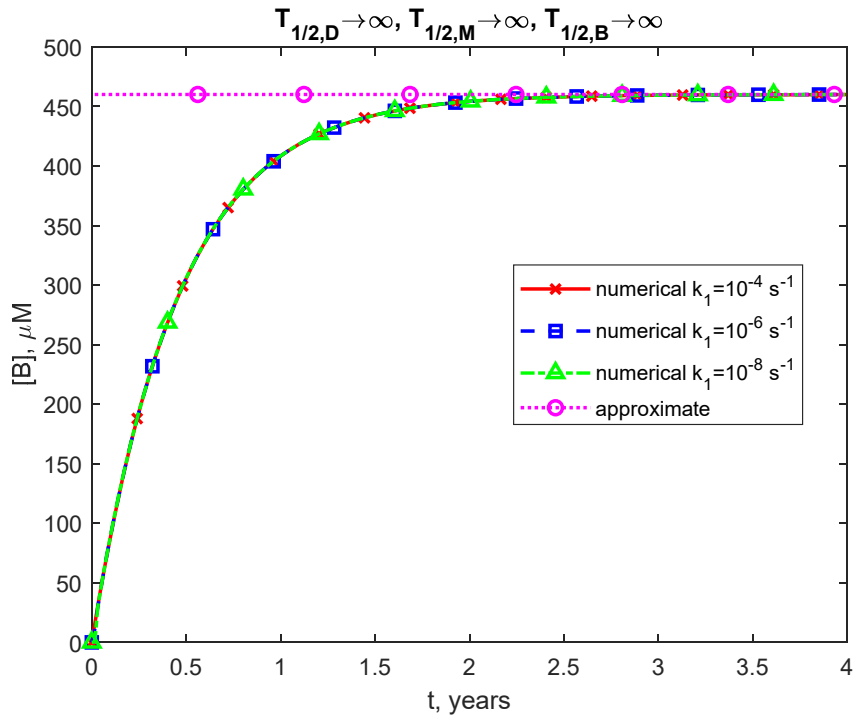

(b)

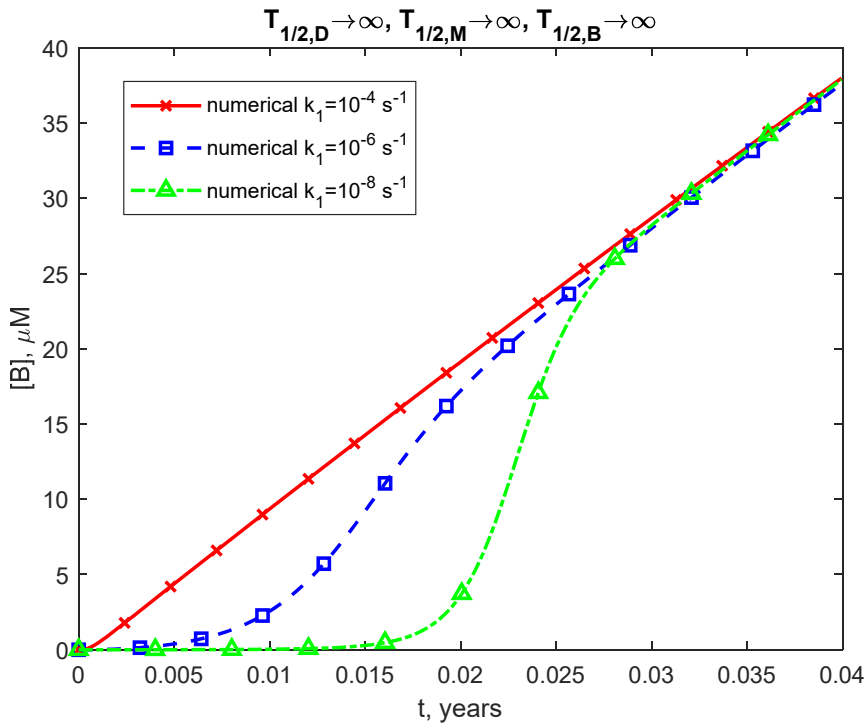

Fig. S3. (a) Molar concentration of free misfolded oligomers of TDP-43, [*B*], as a function of time (in years). (b) Similar to Fig. S3a, but with a focus on the specific time range of [0, 0.04 years] on the *x*-axis. The numerical solution is obtained by solving Eqs. (4)-(7) with initial condition (8). The approximate solution is determined using Eq. (16). The presented scenario assumes dysfunctional protein degradation machinery with $T_{1/2,D} \to \infty$, $T_{1/2,M} \to \infty$, and $T_{1/2,B} \to \infty$. The results are shown for three values of k_1. The case with $k_2 = 10^{-6}$ μM^{-1} s^{-1}, $k_M = 10^{-4}$ s^{-1}, and $\theta_{1/2,B} = 10^7$ s.

(a)

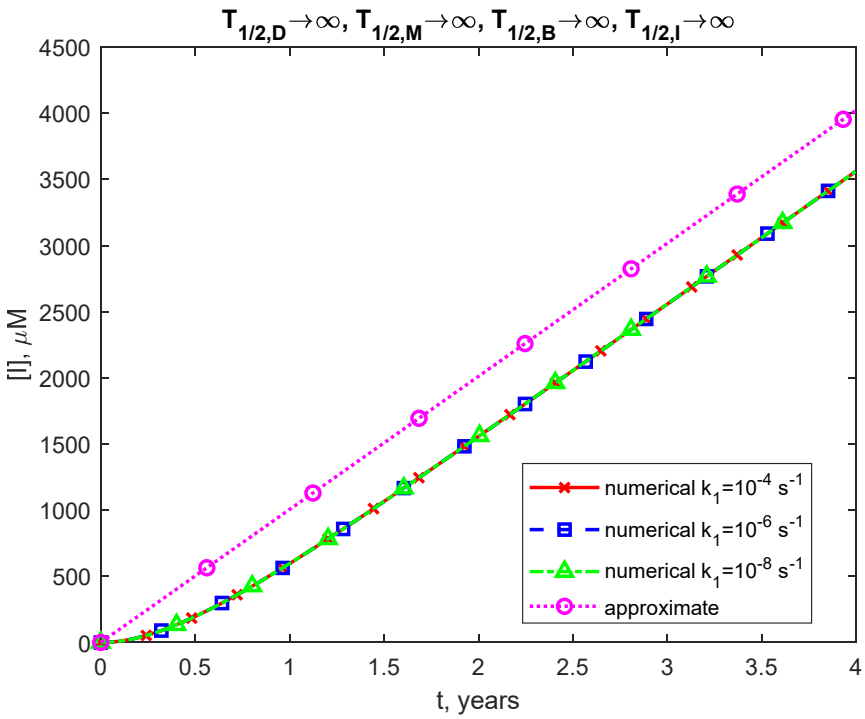

(b)

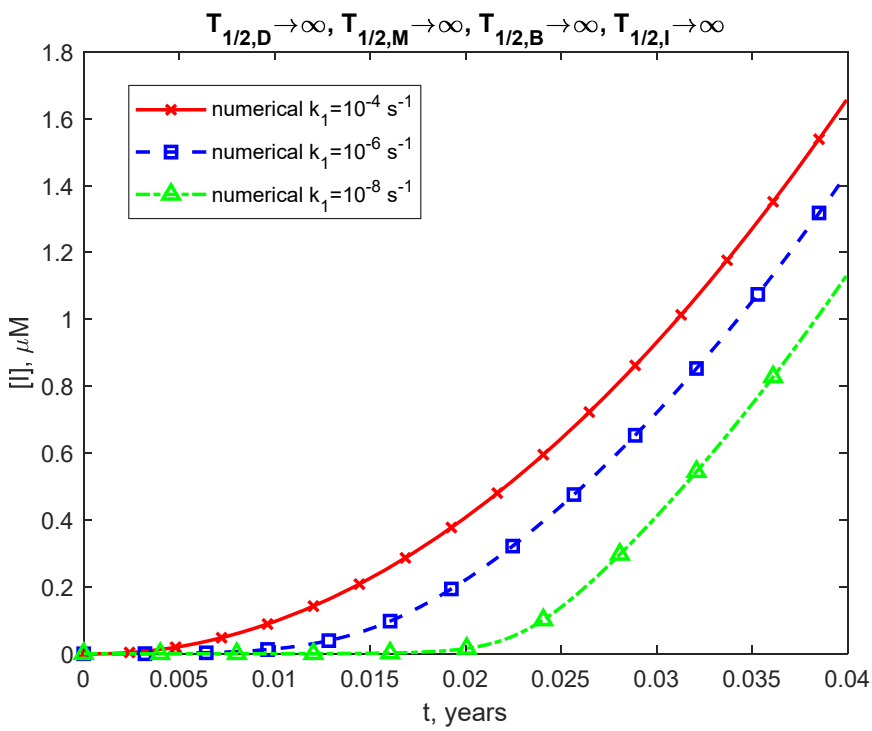

Fig. S4. (a) Molar concentration of toxic TDP-43 oligomers incorporated into inclusion bodies, [*I*], as a function of time (in years). (b) Similar to Fig. S4a, but with a focus on the specific time range of [0, 0.04

years] on the *x*-axis. The numerical solution is obtained by solving Eqs. (4)-(7) with initial conditions (8). The approximate solution is determined using Eq. (20). The presented scenario assumes dysfunctional protein degradation machinery with $T_{1/2,D} \to \infty$, $T_{1/2,M} \to \infty$, $T_{1/2,B} \to \infty$, and $T_{1/2,I} \to \infty$. The results are shown for three values of k_1. The case with $k_2 = 10^{-6}$ μM^{-1} s^{-1}, $k_M = 10^{-4}$ s^{-1}, and $\theta_{1/2,B} = 10^7$ s.

(a)

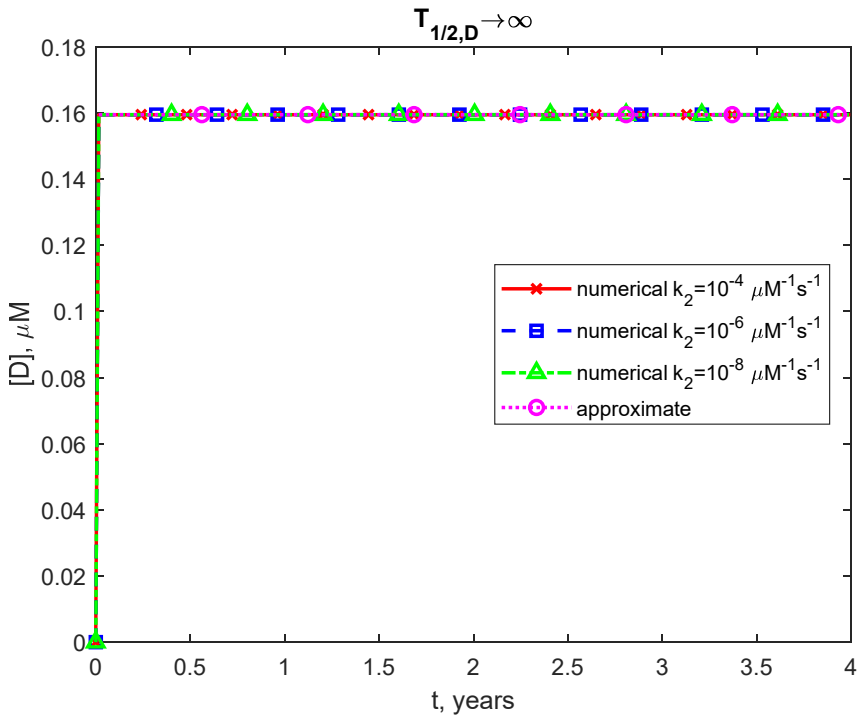

(b)

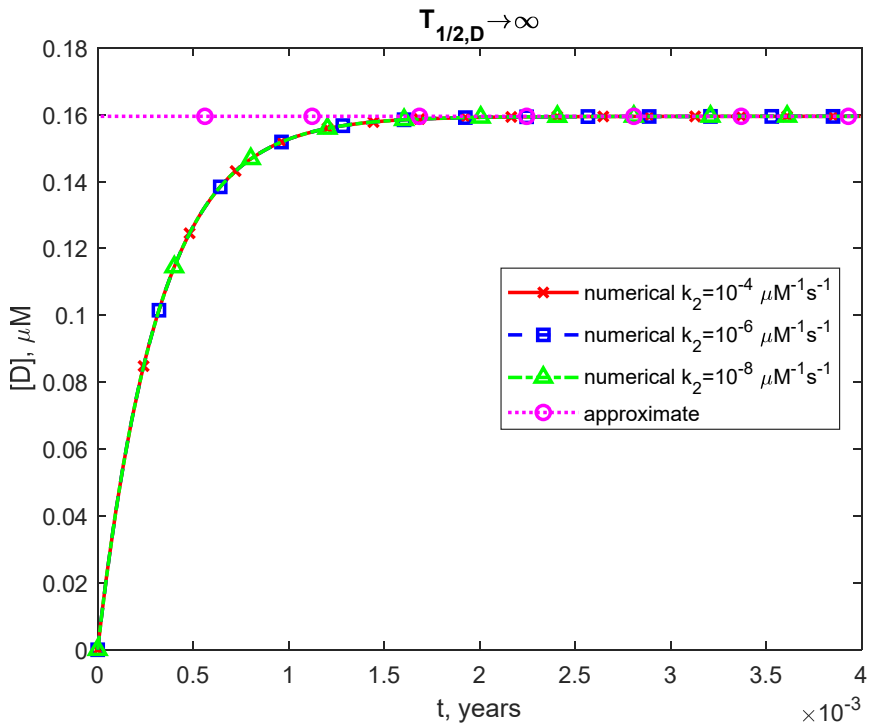

Fig. S5. (a) Molar concentration of TDP-43 dimers, [*D*], as a function of time (in years). (b) Similar to Fig. S5a, but with a focus on the specific time range of [0, 0.004 years] on the *x*-axis. The numerical solution is obtained by solving Eqs. (4)-(7) with initial conditions (8). The approximate solution is determined using Eq. (14). The presented scenario assumes dysfunctional protein degradation machinery with $T_{1/2,D} \to \infty$. The results are shown for three values of k_2. The case with $k_1 = 10^{-6}$ s^{-1}, $k_M = 10^{-4}$ s^{-1}, and $\theta_{1/2,B} = 10^7$ s.

(a)

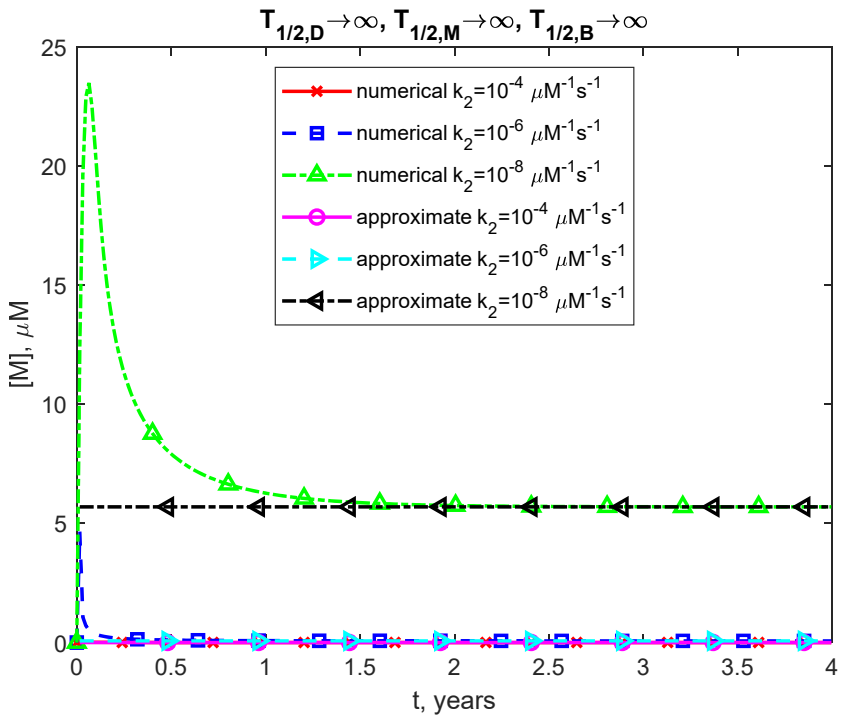

(b)

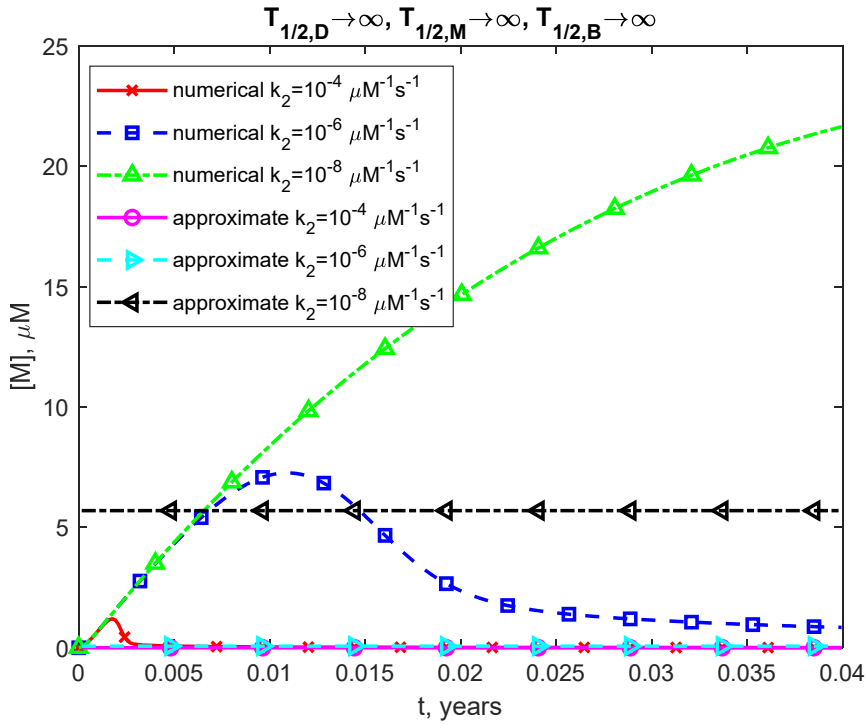

Fig. S6. (a) Molar concentration of TDP-43 monomers, [*M*], as a function of time (in years). (b) Similar to Fig. S6a, but with a focus on the specific time range of [0, 0.04 years] on the *x*-axis. The numerical

solution is obtained by solving Eqs. (4)-(7) with initial conditions (8). The approximate solution is determined using Eq. (17). The presented scenario assumes dysfunctional protein degradation machinery with $T_{1/2,D} \to \infty$, $T_{1/2,M} \to \infty$, and $T_{1/2,B} \to \infty$. The results are shown for three values of k_2. The case with $k_1 = 10^{-6}$ s^{-1}, $k_M = 10^{-4}$ s^{-1}, and $\theta_{1/2,B} = 10^7$ s.

(a)

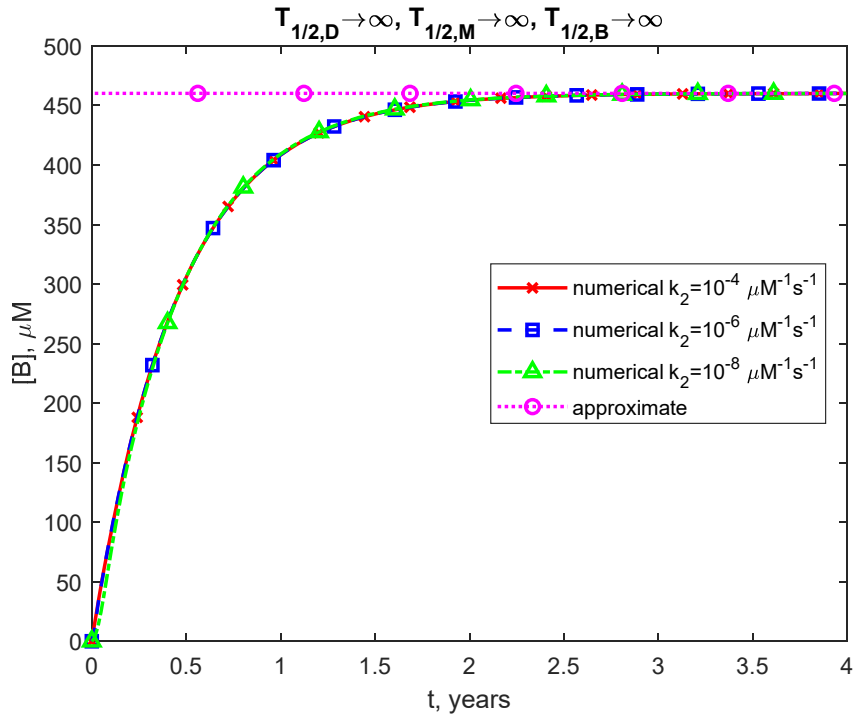

(b)

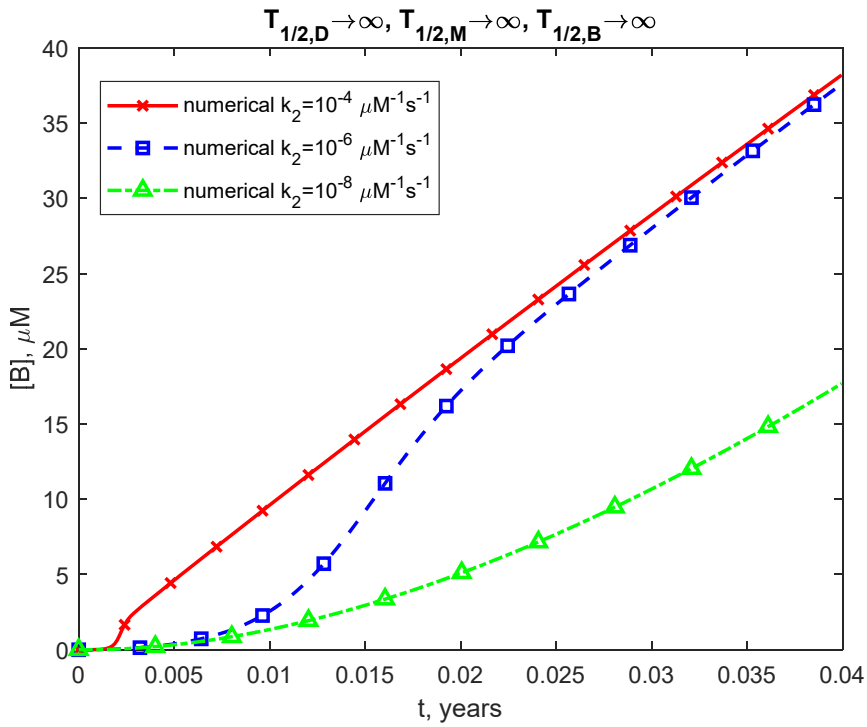

Fig. S7. (a) Molar concentration of free misfolded TDP-43 oligomers, [*B*], as a function of time (in years). (b) Similar to Fig. S7a, but with a focus on the specific time range of [0, 0.04 years] on the *x*-axis. The numerical solution is obtained by solving Eqs. (4)-(7) with initial conditions (8), while the approximate solution is determined using Eq. (16). The presented scenario assumes dysfunctional protein degradation machinery with $T_{1/2,D} \to \infty$, $T_{1/2,M} \to \infty$, and $T_{1/2,B} \to \infty$. The results are shown for three values of k_2. The case with $k_1 = 10^{-6}$ s^{-1}, $k_M = 10^{-4}$ s^{-1}, and $\theta_{1/2,B} = 10^7$ s.

(a)

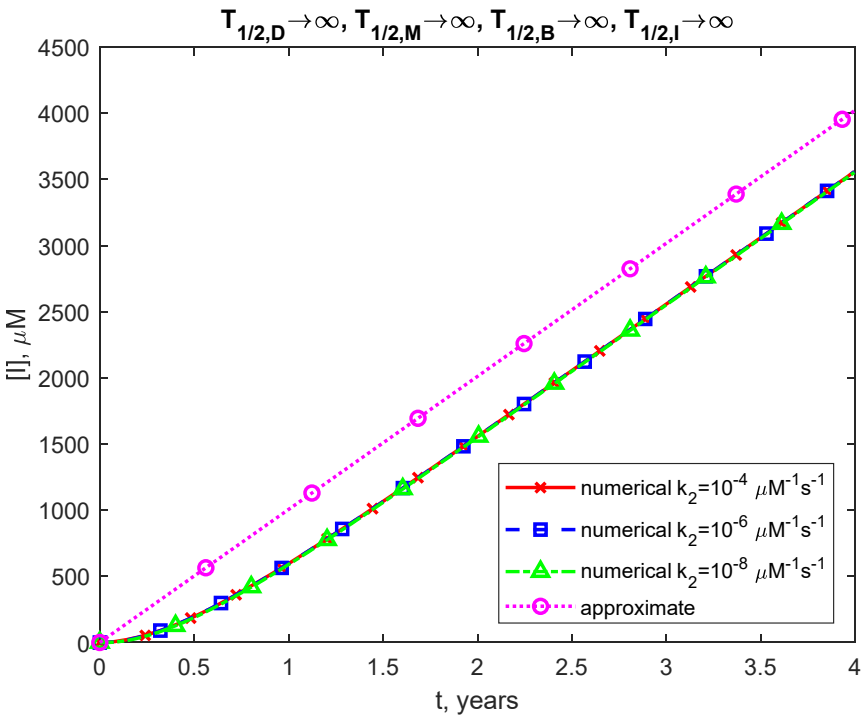

(b)

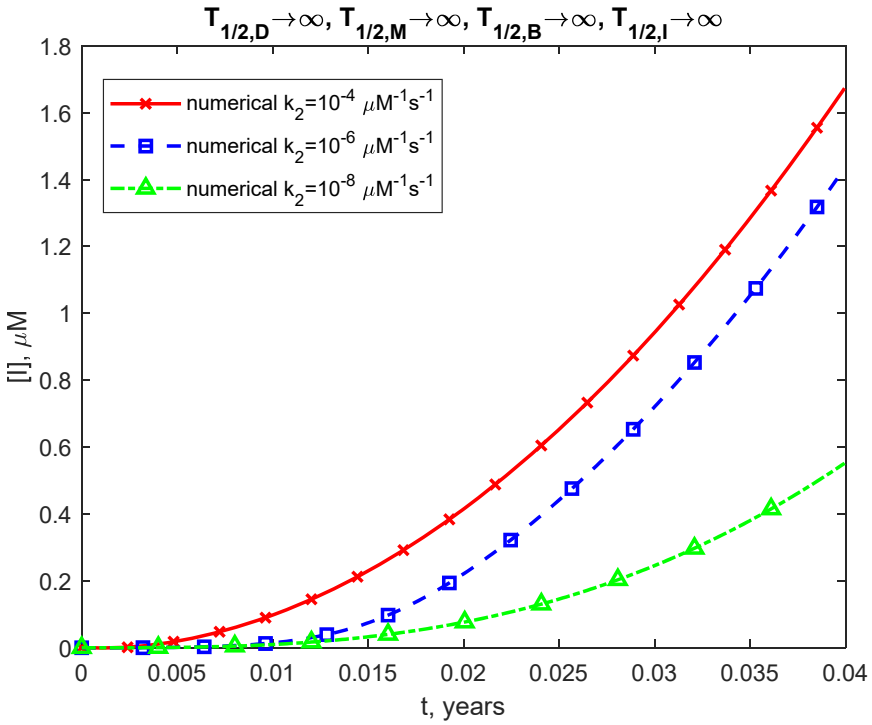

Fig. S8. (a) Molar concentration of toxic TDP-43 oligomers incorporated into inclusion bodies, [*I*], as a function of time (in years). (b) Similar to Fig. S8a, but with a focus on the specific time range of [0, 0.04

years] on the *x*-axis. The numerical solution is obtained by solving Eqs. (4)-(7) with initial conditions (8), while the approximate solution is determined using Eq. (20). The presented scenario assumes dysfunctional protein degradation machinery with $T_{1/2,D} \to \infty$, $T_{1/2,M} \to \infty$, $T_{1/2,B} \to \infty$, and $T_{1/2,I} \to \infty$. The results are shown for three values of k_2. The case with $k_1 = 10^{-6}$ s^{-1}, $k_M = 10^{-4}$ s^{-1}, and $\theta_{1/2,B} = 10^7$ s.

(a)

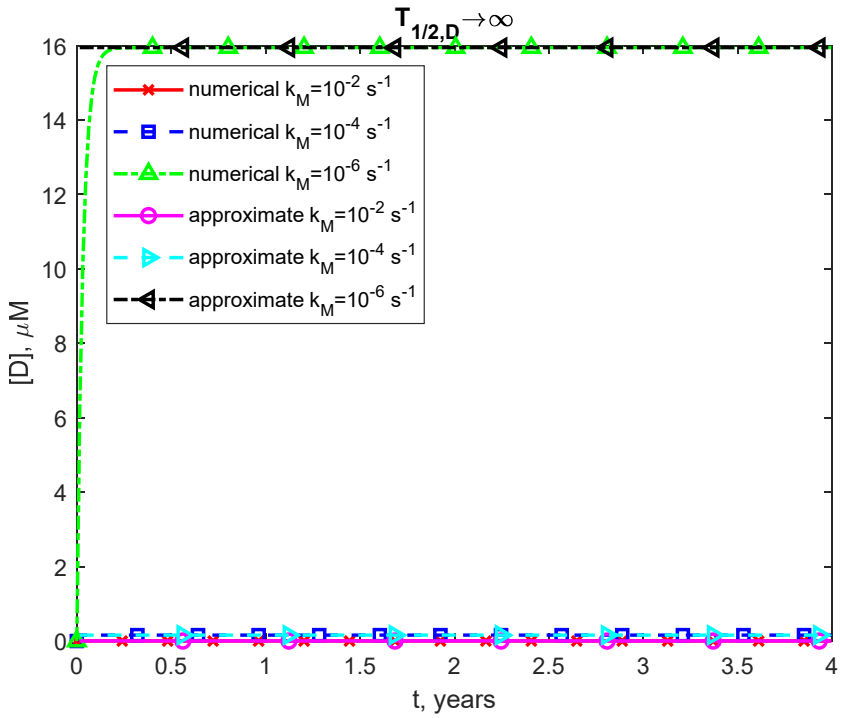

(b)

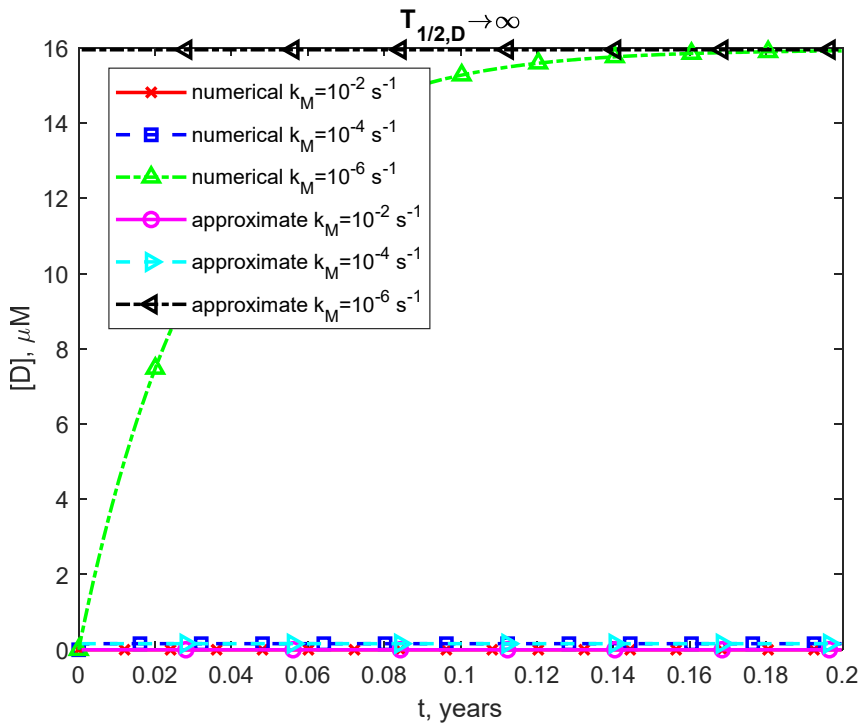

Fig. S9. (a) Molar concentration of TDP-43 dimers, [*D*], as a function of time (in years). (b) Similar to Fig. S9a, but with a focus on the specific time range of [0, 0.2 years] on the *x*-axis. The numerical solution is obtained by solving Eqs. (4)-(7) with initial conditions (8), while the approximate solution is determined using Eq. (14). The presented scenario assumes dysfunctional protein degradation machinery with $T_{1/2,D} \to \infty$. The results are shown for three values of k_M. The case with $k_1 = 10^{-6}$ s^{-1}, $k_2 = 10^{-6}$ μM^{-1} s^{-1}, and $\theta_{1/2,B} = 10^7$ s.

(a)

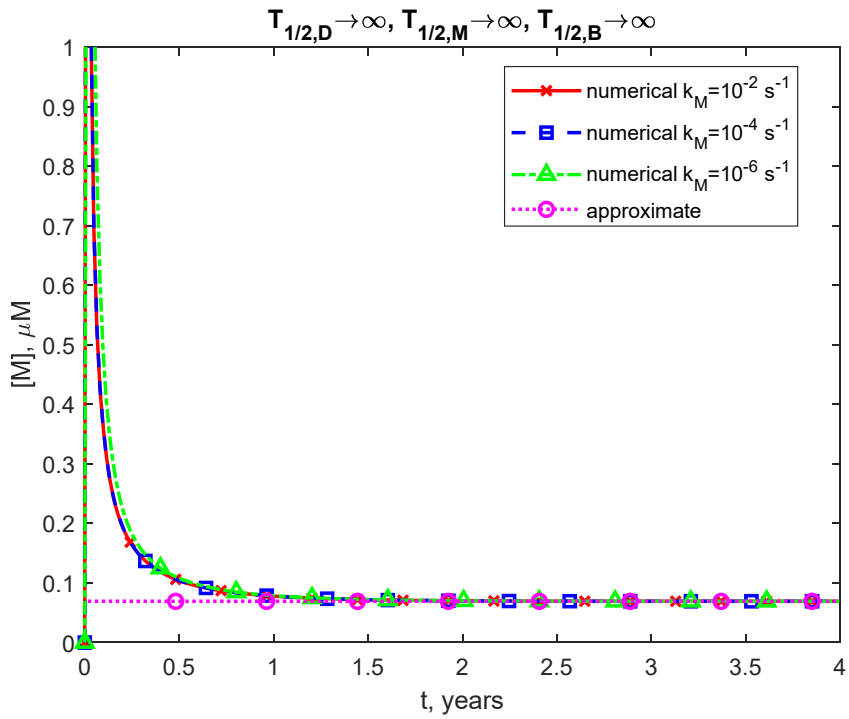

(b)

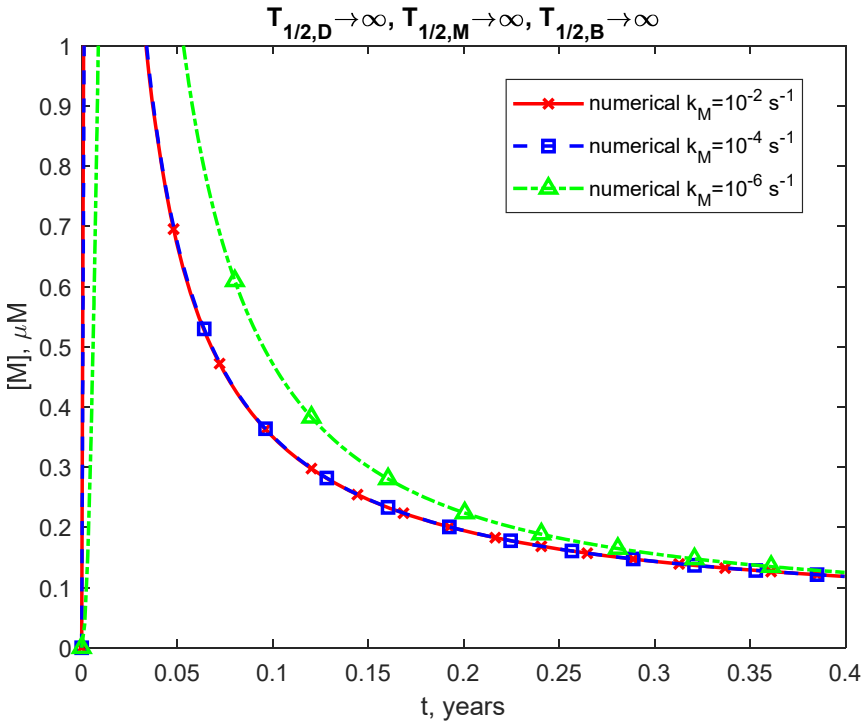

Fig. S10. (a) Molar concentration of TDP-43 monomers, [*M*], as a function of time (in years). (b) Similar to Fig. S10a, but with a focus on the specific time range of [0, 0.4 years] on the *x*-axis. The numerical

solution is obtained by solving Eqs. (4)-(7) with initial conditions (8), while the approximate solution is determined using Eq. (17). The presented scenario assumes dysfunctional protein degradation machinery with $T_{1/2,D} \to \infty$, $T_{1/2,M} \to \infty$, and $T_{1/2,B} \to \infty$. The results are shown for three values of k_M. The case with $k_1 = 10^{-6}$ s^{-1}, $k_2 = 10^{-6}$ μM^{-1} s^{-1}, and $\theta_{1/2,B} = 10^7$ s.

(a)

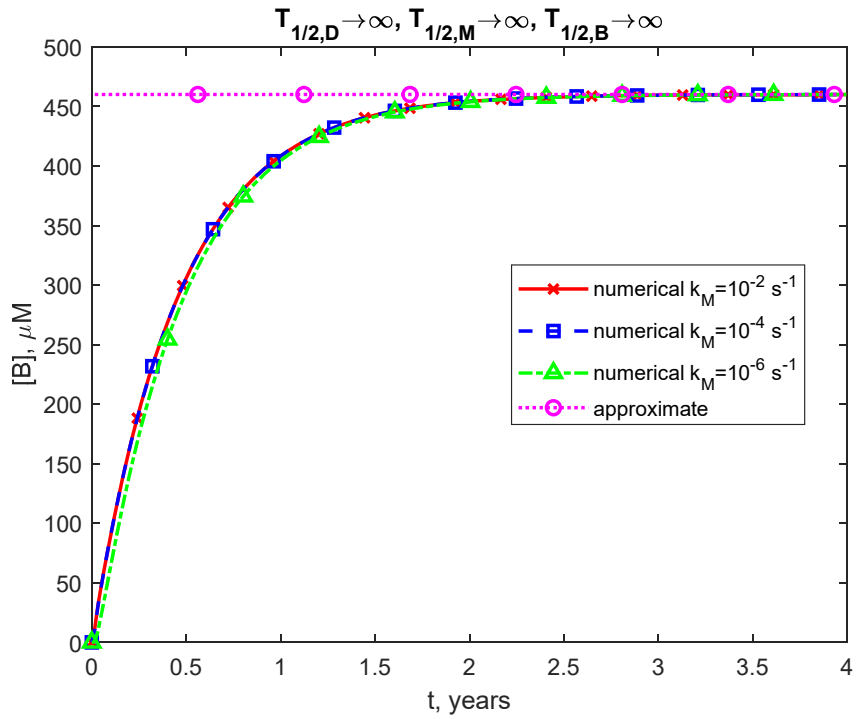

(b)

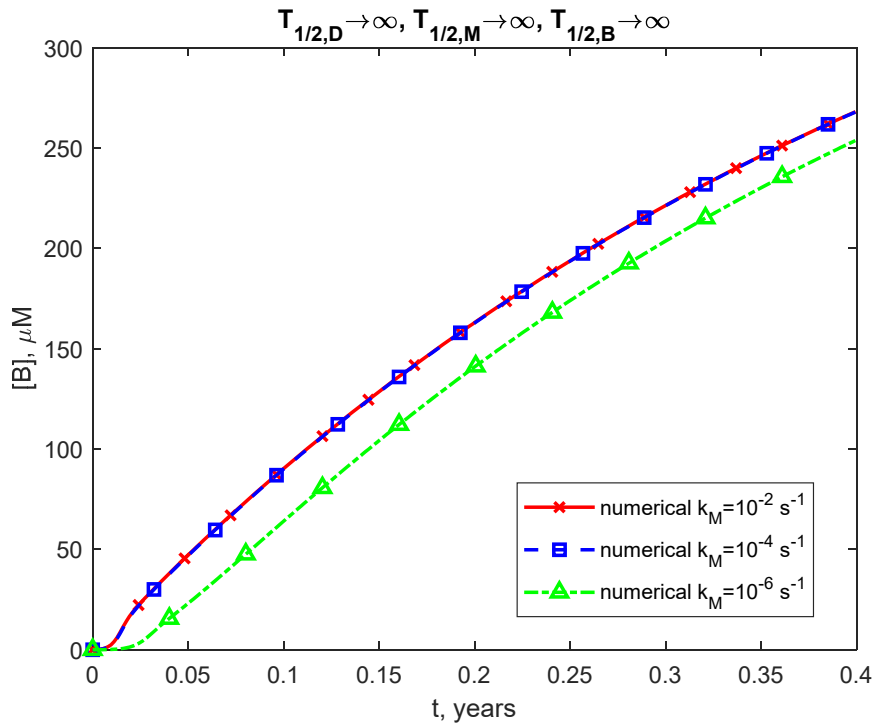

Fig. S11. (a) Molar concentration of free misfolded oligomers of TDP-43, [*B*], as a function of time (in years). (b) Similar to Fig. S11a, but with a focus on the specific time range of [0, 0.4 years] on the *x*-axis. The numerical solution is obtained by solving Eqs. (4)-(7) with initial conditions (8), while the approximate solution is determined using Eq. (16). The presented scenario assumes dysfunctional protein degradation machinery with $T_{1/2,D} \to \infty$, $T_{1/2,M} \to \infty$, and $T_{1/2,B} \to \infty$. The results are shown for three values of k_M. The case with $k_1 = 10^{-6}$ s^{-1}, $k_2 = 10^{-6}$ μM^{-1} s^{-1}, and $\theta_{1/2,B} = 10^7$ s.

(a)

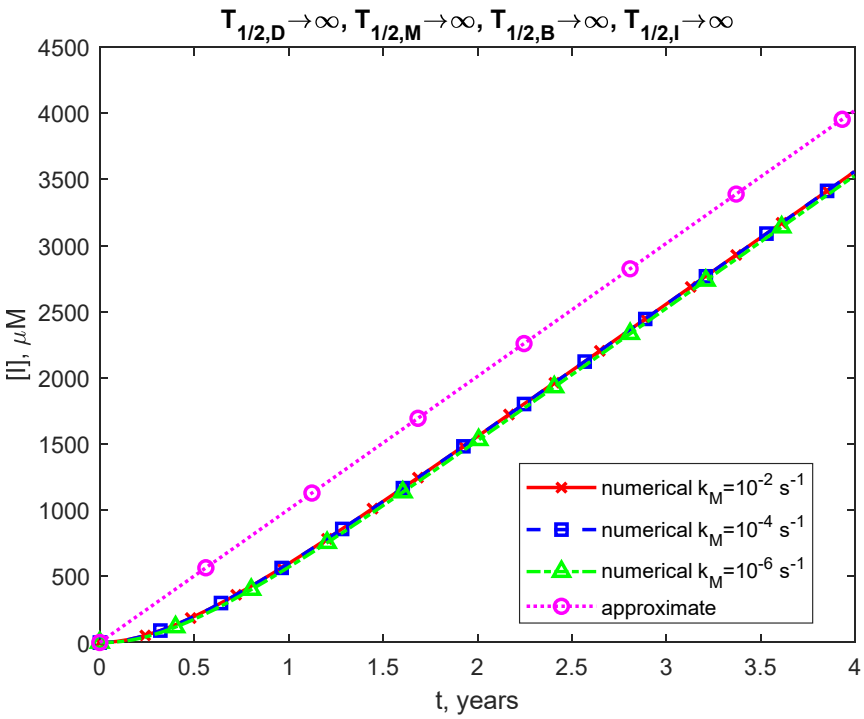

(b)

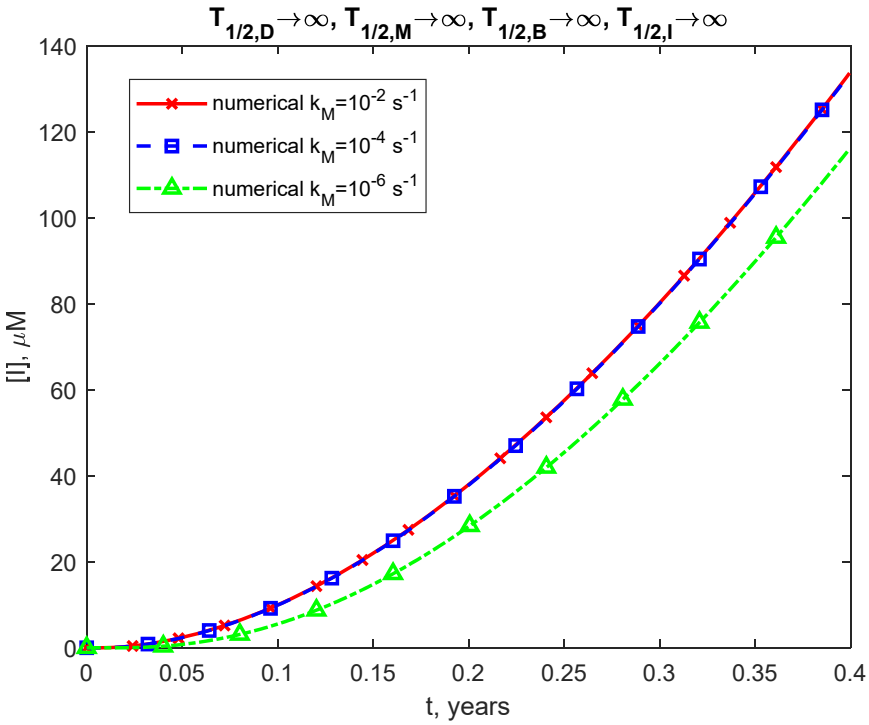

Fig. S12. (a) Molar concentration of toxic TDP-43 oligomers incorporated into inclusion bodies, [*I*], as a function of time (in years). (b) Similar to Fig. S12a, but with a focus on the specific time range of [0, 0.4

years] on the *x*-axis. The numerical solution is obtained by solving Eqs. (4)-(7) with initial conditions (8), while the approximate solution is determined using Eq. (20). The presented scenario assumes dysfunctional protein degradation machinery with $T_{1/2,D} \to \infty$, $T_{1/2,M} \to \infty$, $T_{1/2,B} \to \infty$, and $T_{1/2,I} \to \infty$. The results are shown for three values of k_M. The case with $k_1 = 10^{-6}$ s^{-1}, $k_2 = 10^{-6}$ μM^{-1} s^{-1}, and $\theta_{1/2,B} = 10^7$ s.

(a)

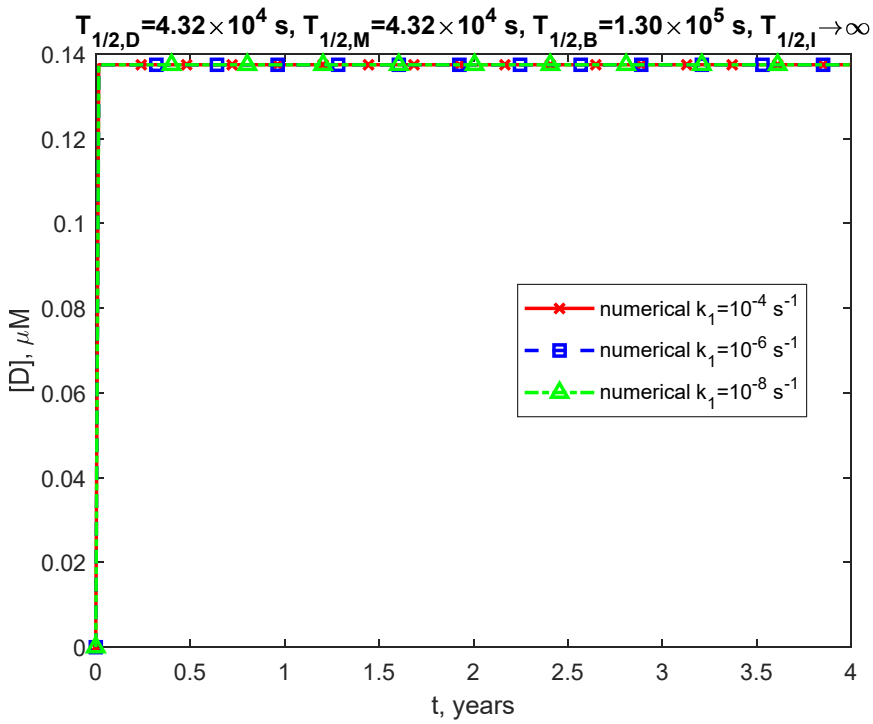

(b)

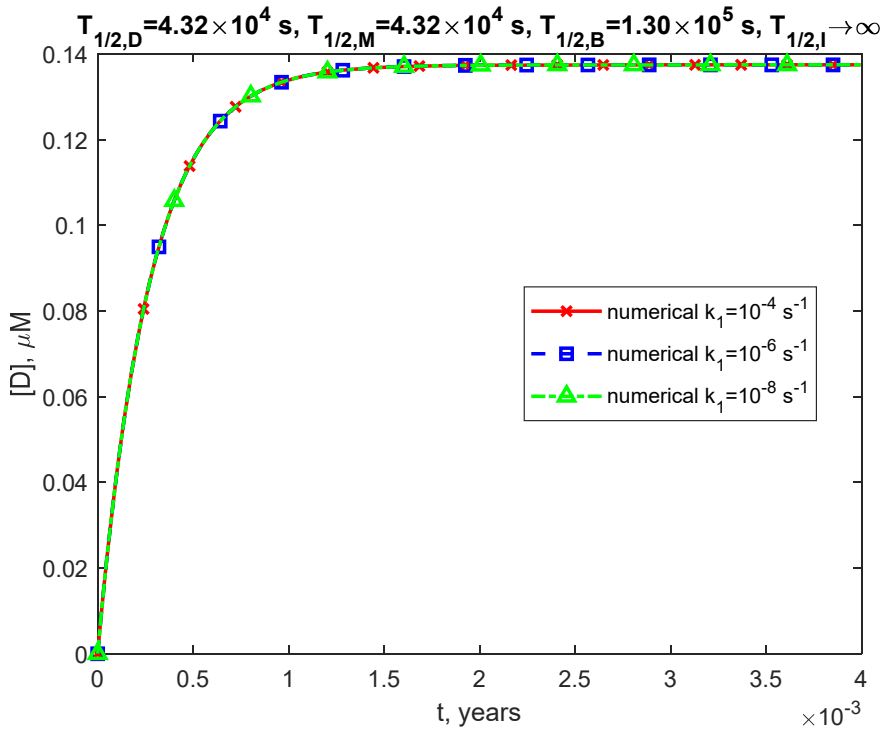

Fig. S13. (a) Molar concentration of TDP-43 dimers, [*D*], as a function of time (in years). (b) Similar to Fig. S13a, but with a focus on the specific time range of [0, 0.004 years] on the *x*-axis. The numerical solution is obtained by solving Eqs. (4)-(7) with initial conditions (8). The presented scenario assumes a physiologically relevant half-life for TDP-43 dimers: $T_{1/2,D} = 4.32 \times 10^4$ s. The approximate solution is not shown, as it applies only to the scenario with infinite half-lives of TDP-43 dimers, monomers, and free misfolded oligomers. The results are displayed for three values of k_1. The case with $k_2 = 10^{-6}$ μM^{-1} s^{-1}, $k_M = 10^{-4}$ s^{-1}, and $\theta_{1/2,B} = 10^7$ s.

(a)

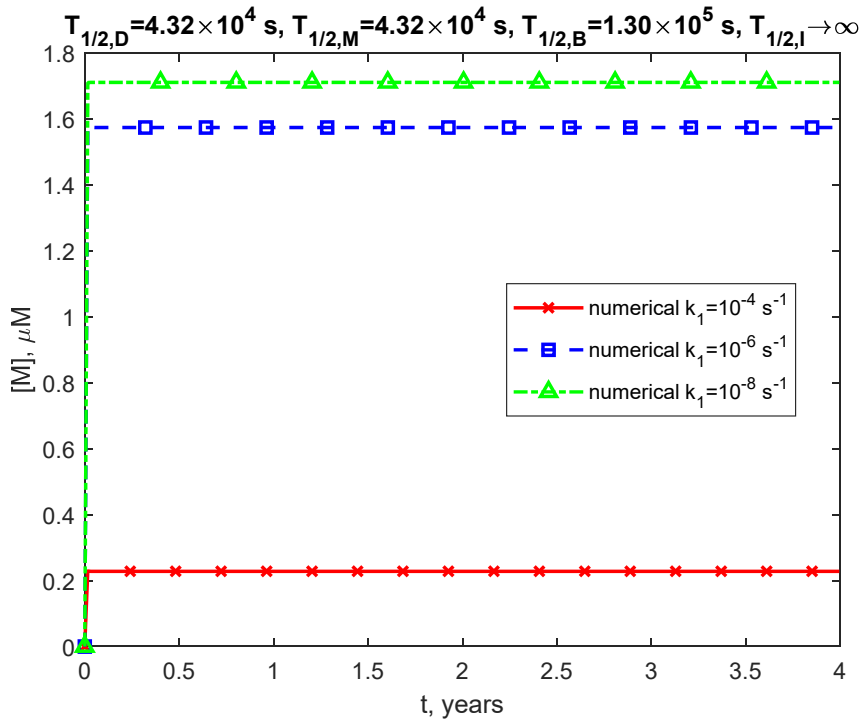

(b)

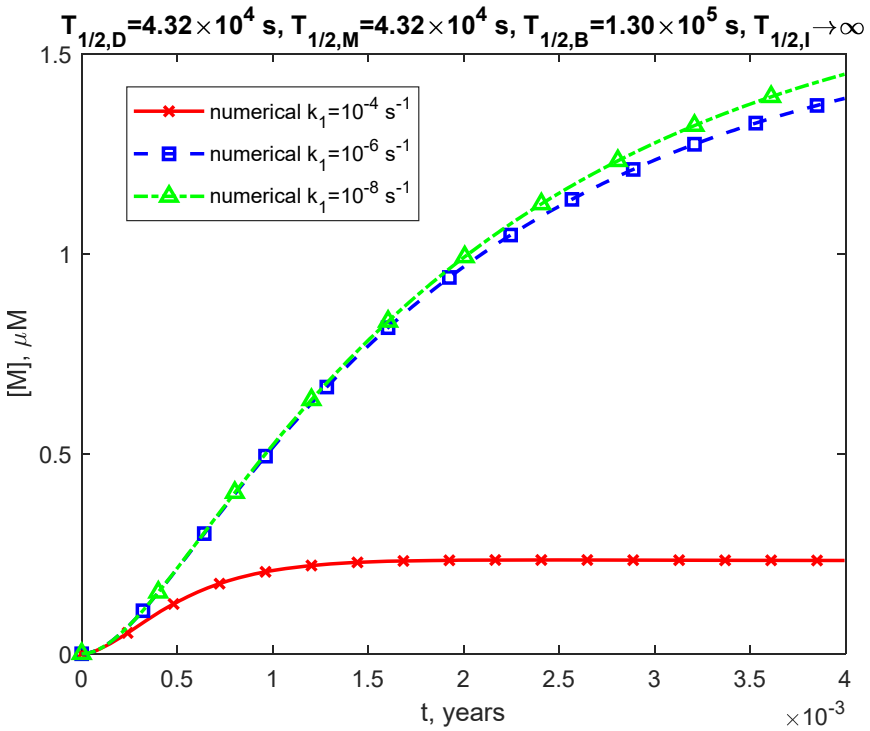

Fig. S14. (a) Molar concentration of TDP-43 monomers, [*M*], as a function of time (in years). (b) Similar to Fig. S14a, but with a focus on the specific time range of [0, 0.004 years] on the *x*-axis. The numerical

solution is obtained by solving Eqs. (4)-(7) with initial conditions (8). The presented scenario assumes physiologically relevant half-lives for TDP-43 dimers, monomers, and free misfolded oligomers: $T_{1/2,D} = 4.32\times10^4$ s, $T_{1/2,M} = 4.32\times10^4$ s, and $T_{1/2,B} = 1.30\times10^5$ s. The approximate solution is not shown, as it applies only to the scenario with infinite half-lives of TDP-43 dimers, monomers, and free misfolded oligomers. The results are displayed for three values of k_1. The case with $k_2 = 10^{-6}$ μM^{-1} s^{-1}, $k_M = 10^{-4}$ s^{-1}, and $\theta_{1/2,B} = 10^7$ s.

(a)

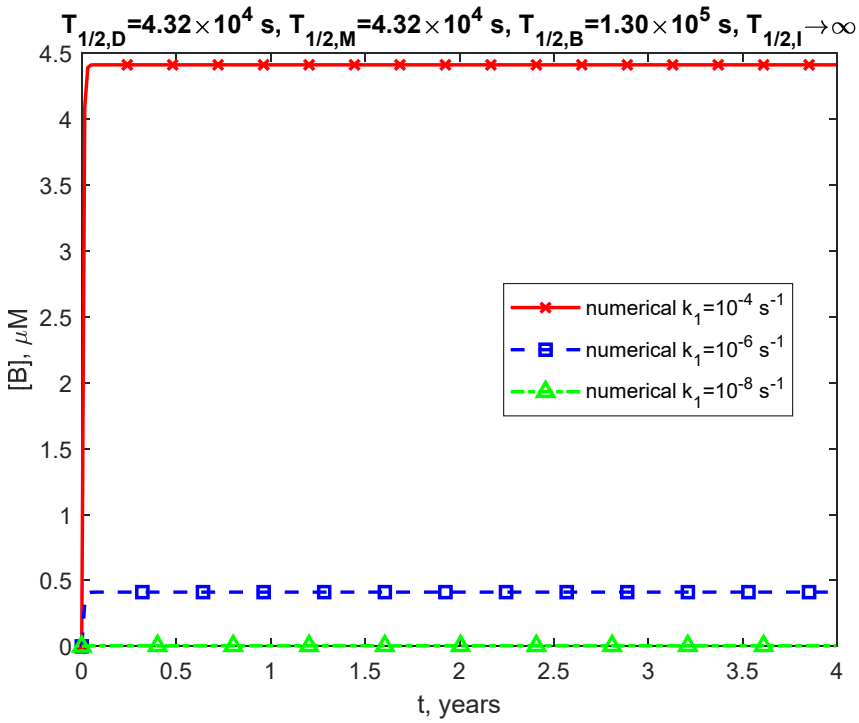

(b)

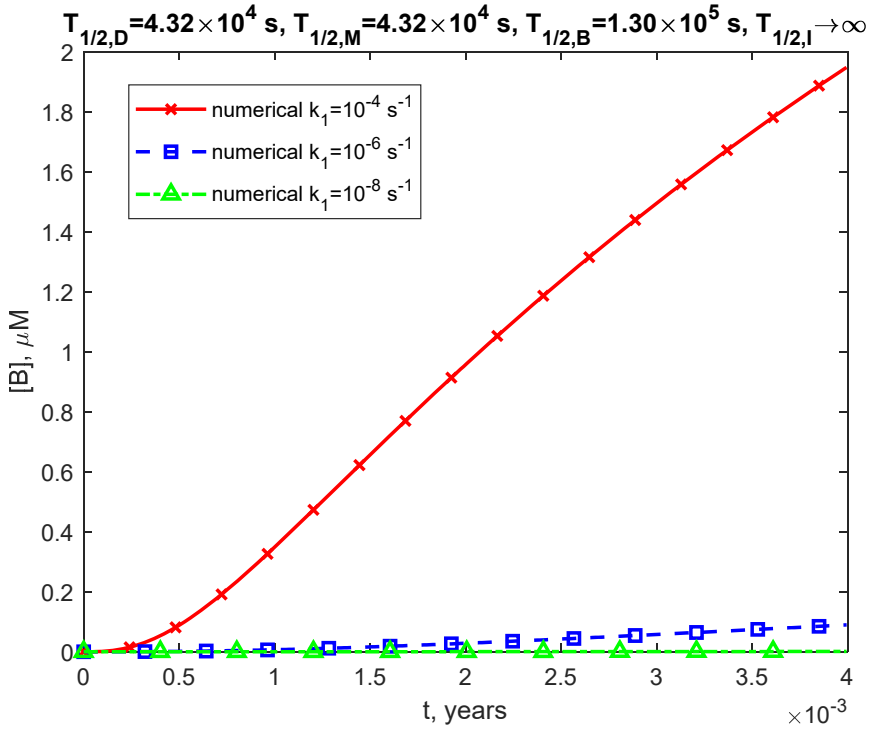

Fig. S15. (a) Molar concentration of free misfolded oligomers of TDP-43, [*B*], as a function of time (in years). (b) Similar to Fig. S15a, but with a focus on the specific time range of [0, 0.004 years] on the *x*-axis. The numerical solution is obtained by solving Eqs. (4)-(7) with initial conditions (8). The presented scenario assumes physiologically relevant half-lives for TDP-43 dimers, monomers, and free misfolded oligomers: $T_{1/2,D} = 4.32\times10^4$ s, $T_{1/2,M} = 4.32\times10^4$ s, and $T_{1/2,B} = 1.30\times10^5$ s. The approximate solution is not shown, as it applies only to the scenario with infinite half-lives of TDP-43 dimers, monomers, and free misfolded oligomers. The results are displayed for three values of k_1. The case with $k_2 = 10^{-6}$ μM^{-1} s^{-1}, $k_M = 10^{-4}$ s^{-1}, and $\theta_{1/2,B} = 10^7$ s.

(a)

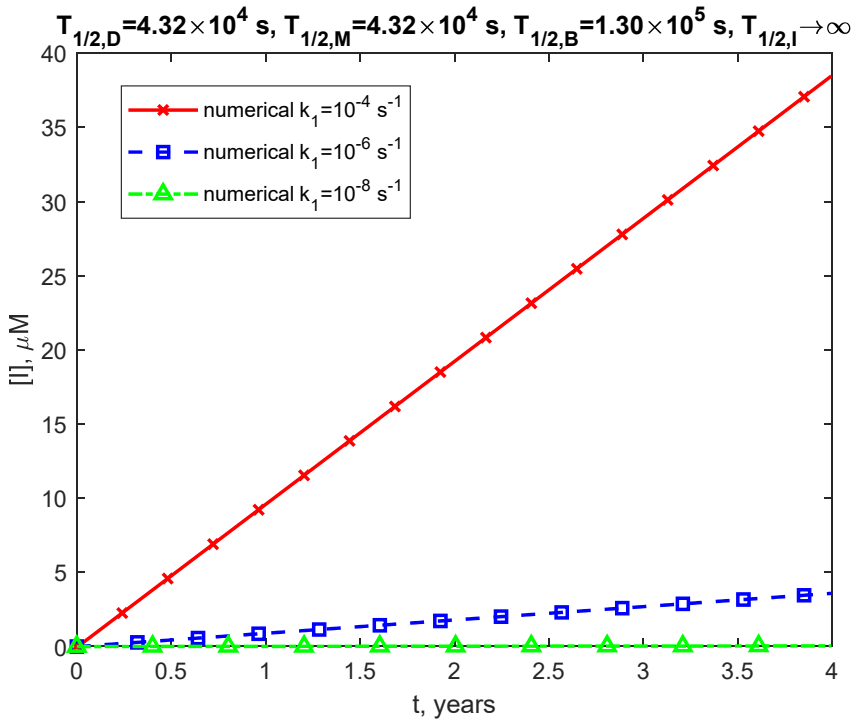

(b)

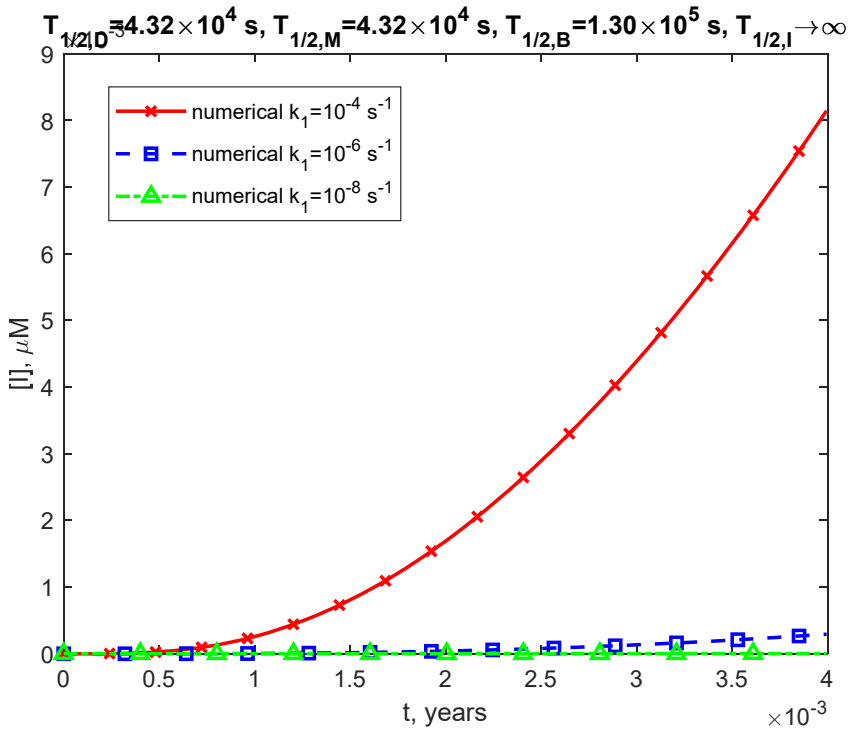

Fig. S16. (a) Molar concentration of toxic TDP-43 oligomers incorporated into inclusion bodies, [*I*], as a function of time (in years). (b) Similar to Fig. S16a, but with a focus on the specific time range of [0,

0.004 years] on the *x*-axis. The numerical solution is obtained by solving Eqs. (4)-(7) with initial conditions (8). The presented scenario assumes physiologically relevant half-lives for TDP-43 dimers, monomers, free misfolded oligomers, and oligomers deposited into inclusion bodies: $T_{1/2,D} = 4.32\times10^4$ s, $T_{1/2,M} = 4.32\times10^4$ s, $T_{1/2,B} = 1.30\times10^5$ s, and $T_{1/2,I} \to \infty$. The approximate solution is not shown, as it applies only to the scenario with infinite half-lives of TDP-43 dimers, monomers, and free misfolded oligomers. The results are displayed for three values of k_1. The case with $k_2 = 10^{-6}$ μM^{-1} s^{-1}, $k_M = 10^{-4}$ s^{-1}, and $\theta_{1/2,B} = 10^7$ s.

(a)

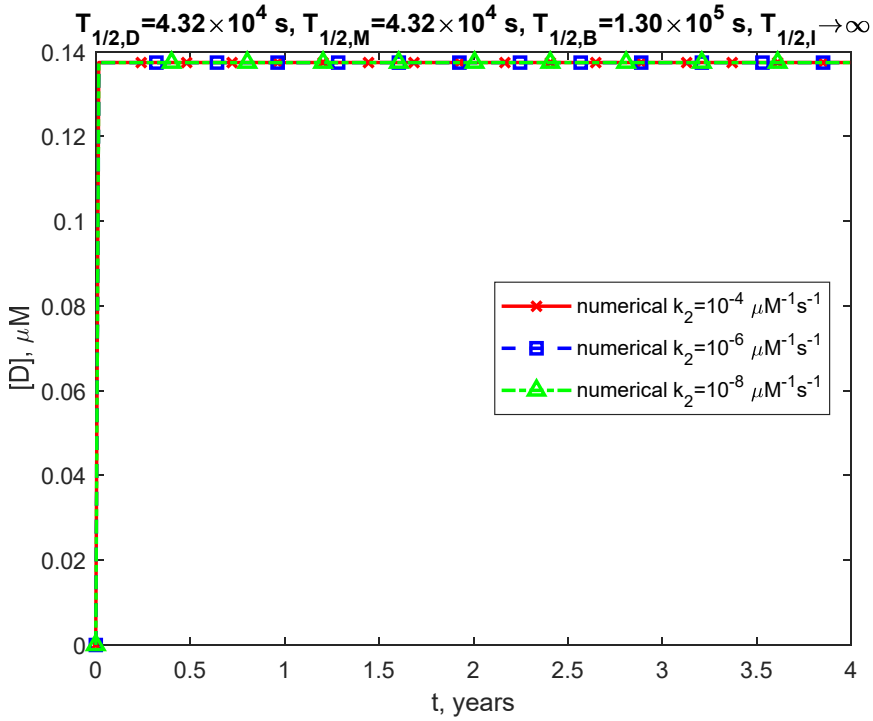

(b)

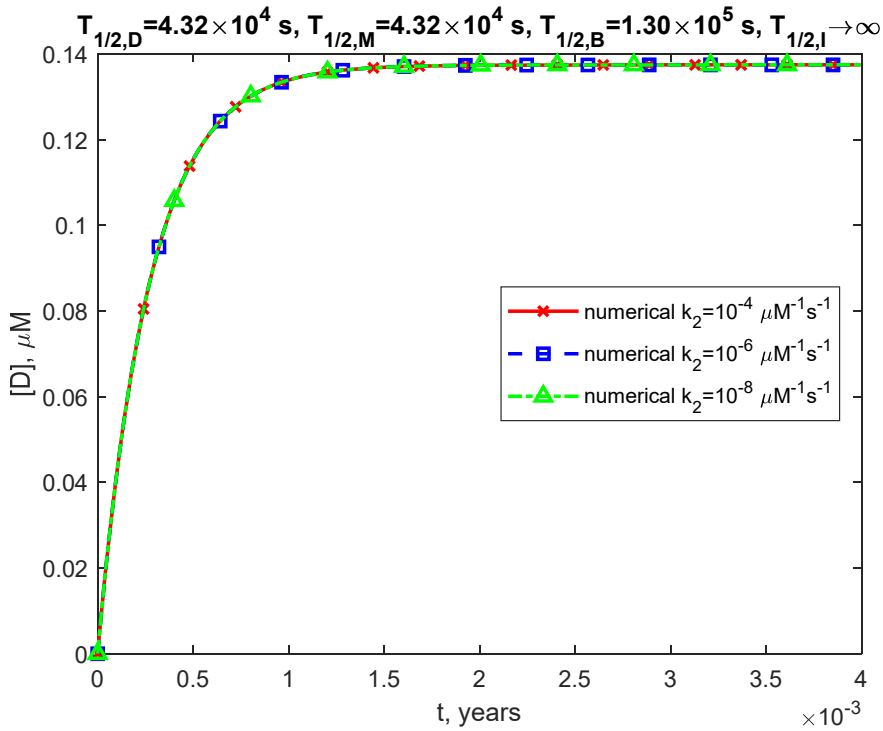

Fig. S17. (a) Molar concentration of TDP-43 dimers, [*D*], as a function of time (in years). (b) Similar to Fig. S17a, but with a focus on the specific time range of [0, 0.004 years] on the *x*-axis. The numerical solution is obtained by solving Eqs. (4)-(7) with initial conditions (8). The presented scenario assumes a physiologically relevant half-life for TDP-43 dimers: $T_{1/2,D} = 4.32 \times 10^4$ s. The approximate solution is not shown, as it applies only to the scenario with infinite half-lives of TDP-43 dimers, monomers, and free misfolded oligomers. The results are displayed for three values of k_2. The case with $k_1 = 10^{-6}$ s^{-1}, $k_M = 10^{-4}$ s^{-1}, and $\theta_{1/2,B} = 10^7$ s.

(a)

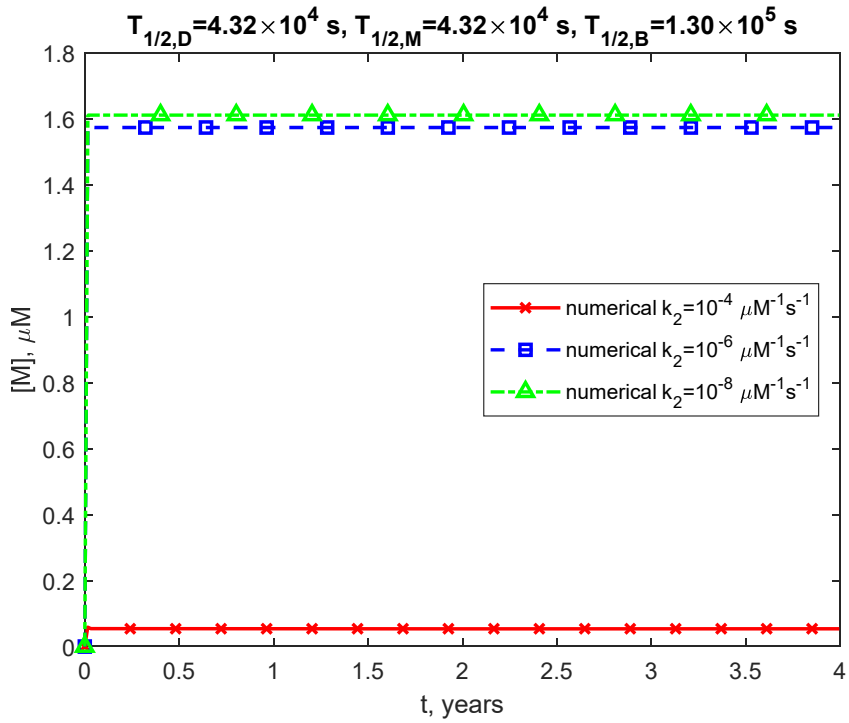

(b)

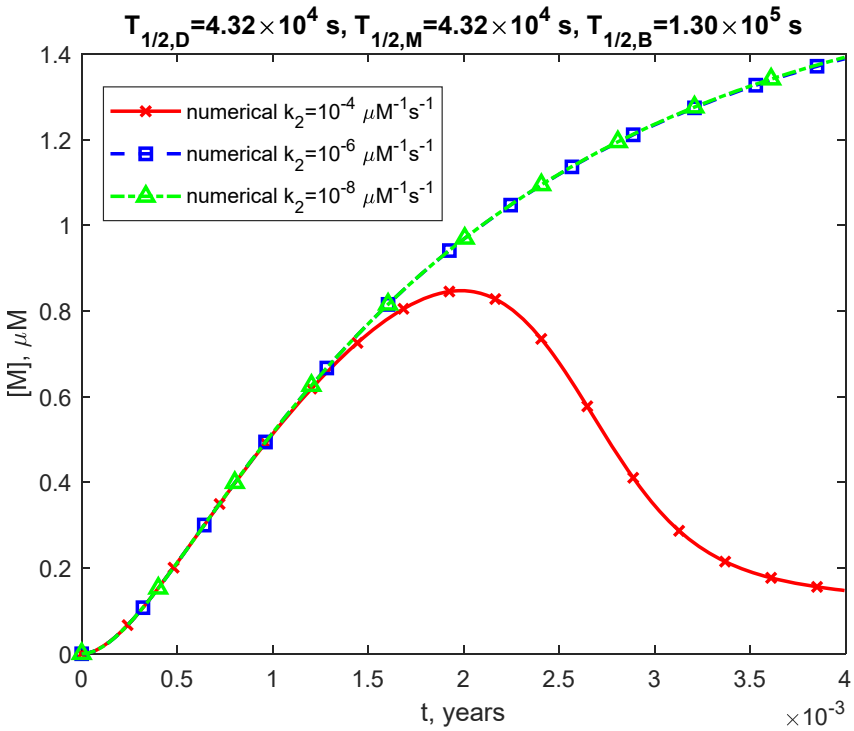

Fig. S18. (a) Molar concentration of TDP-43 monomers, [*M*], as a function of time (in years). (b) Similar to Fig. S18a, but with a focus on the specific time range of [0, 0.004 years] on the *x*-axis. The numerical

solution is obtained by solving Eqs. (4)-(7) with initial conditions (8). The presented scenario assumes physiologically relevant half-lives for TDP-43 dimers, monomers, and free misfolded oligomers: $T_{1/2,D} = 4.32\times10^4$ s, $T_{1/2,M} = 4.32\times10^4$ s, and $T_{1/2,B} = 1.30\times10^5$ s. The approximate solution is not shown, as it applies only to the scenario with infinite half-lives of TDP-43 dimers, monomers, and free misfolded oligomers. The results are displayed for three values of k_2. The case with $k_1 = 10^{-6}$ s^{-1}, $k_M = 10^{-4}$ s^{-1}, and $\theta_{1/2,B} = 10^7$ s.

(a)

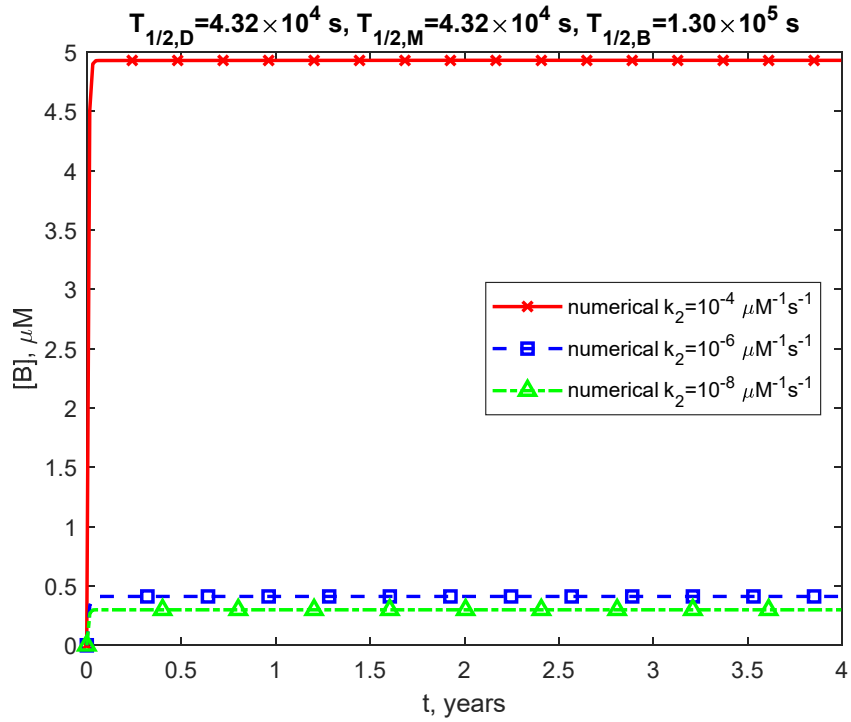

(b)

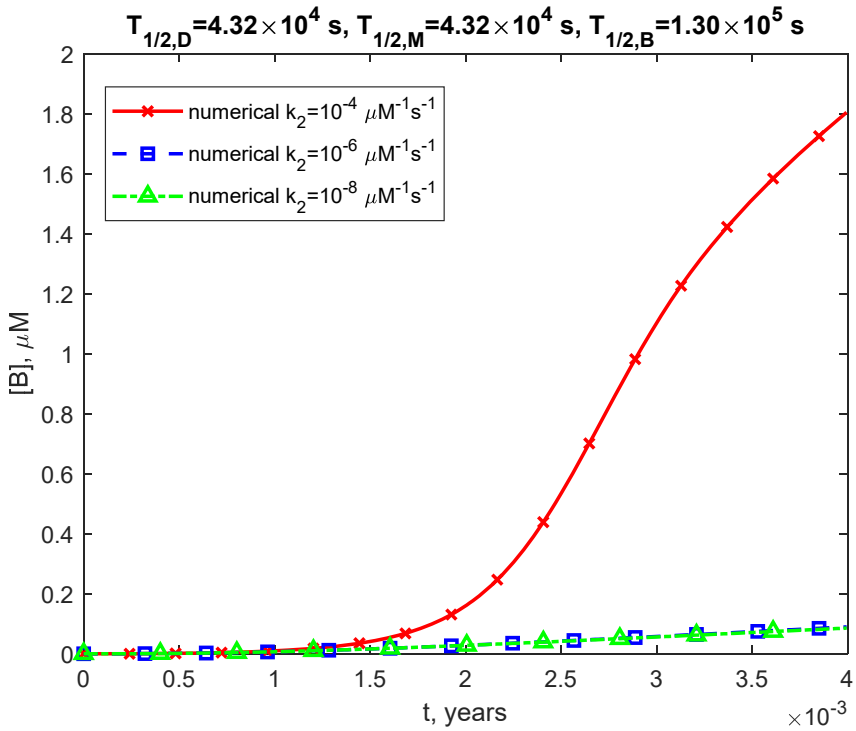

Fig. S19. (a) Molar concentration of free misfolded TDP-43 oligomers, [*B*], as a function of time (in years). (b) Similar to Fig. S19a, but with a focus on the specific time range of [0, 0.004 years] on the *x*-axis. The numerical solution is obtained by solving Eqs. (4)-(7) with initial conditions (8). The presented scenario assumes physiologically relevant half-lives for TDP-43 dimers, monomers, and free misfolded oligomers: $T_{1/2,D} = 4.32\times10^4$ s, $T_{1/2,M} = 4.32\times10^4$ s, and $T_{1/2,B} = 1.30\times10^5$ s. The approximate solution is not shown, as it applies only to the scenario with infinite half-lives of TDP-43 dimers, monomers, and free misfolded oligomers. The results are displayed for three values of k_2. The case with $k_1 = 10^{-6}$ s^{-1}, $k_M = 10^{-4}$ s^{-1}, and $\theta_{1/2,B} = 10^7$ s.

(a)

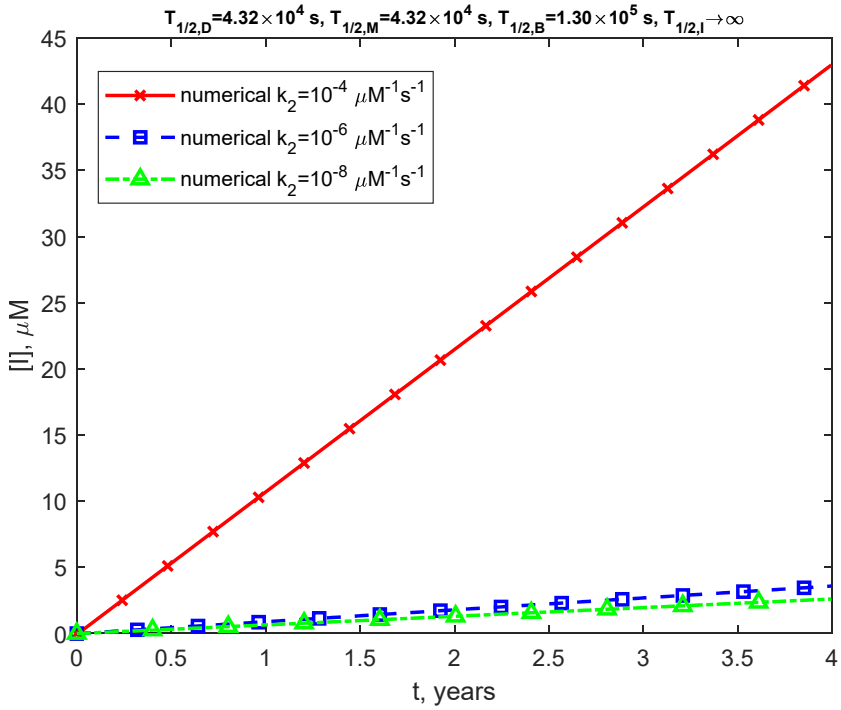

(b)

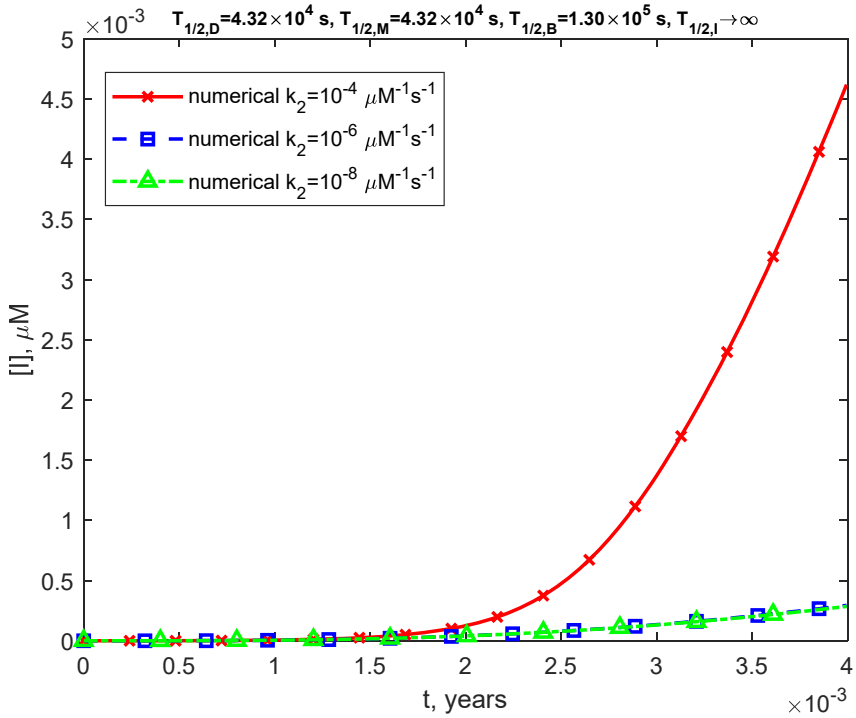

Fig. S20. (a) Molar concentration of toxic TDP-43 oligomers incorporated into inclusion bodies, [*I*], as a function of time (in years). (b) Similar to Fig. S20a, but with a focus on the specific time range of [0,

0.004 years] on the *x*-axis. The numerical solution is obtained by solving Eqs. (4)-(7) with initial conditions (8). The presented scenario assumes physiologically relevant half-lives for TDP-43 dimers, monomers, free misfolded oligomers, and oligomers deposited into inclusion bodies: $T_{1/2,D} = 4.32\times10^4$ s, $T_{1/2,M} = 4.32\times10^4$ s, $T_{1/2,B} = 1.30\times10^5$ s, and $T_{1/2,I} \to \infty$. The approximate solution is not shown, as it applies only to the scenario with infinite half-lives of TDP-43 dimers, monomers, and free misfolded oligomers. The results are displayed for three values of k_2. The case with $k_1 = 10^{-6}$ s^{-1}, $k_M = 10^{-4}$ s^{-1}, and $\theta_{1/2,B} = 10^7$ s.

(a)

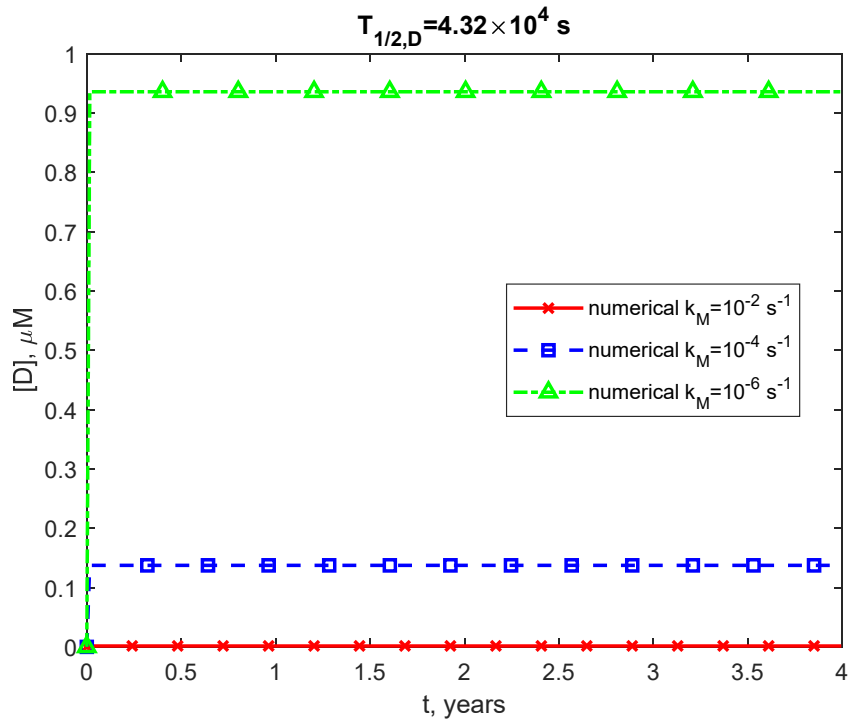

(b)

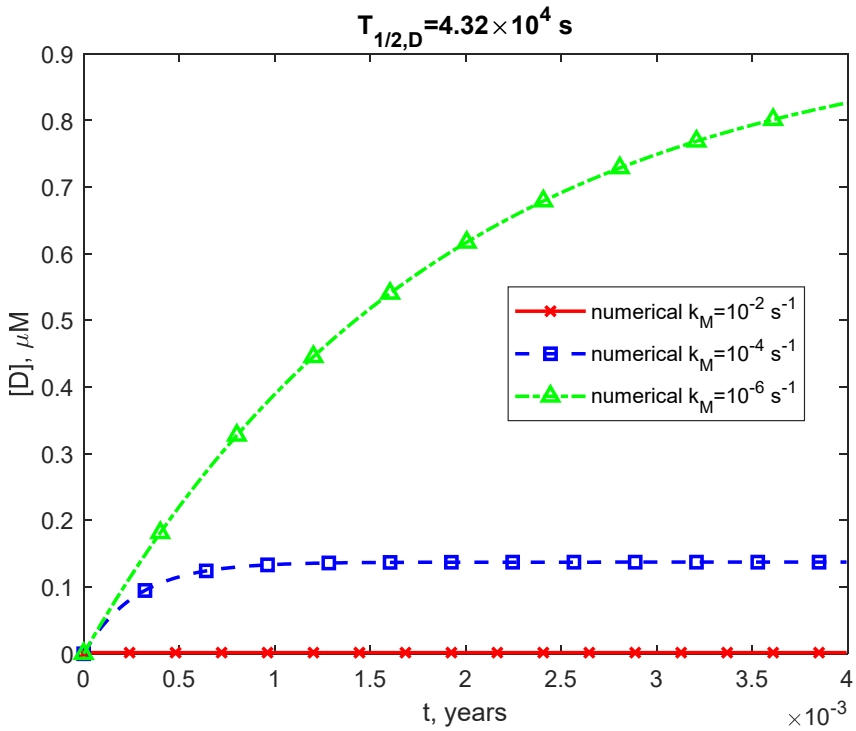

Fig. S21. (a) Molar concentration of TDP-43 dimers, [*D*], as a function of time (in years). (b) Similar to Fig. S21a, but with a focus on the specific time range of [0, 0.004 years] on the *x*-axis. The numerical solution is obtained by solving Eqs. (4)-(7) with initial conditions (8). The presented scenario assumes a physiologically relevant half-life for TDP-43 dimers: $T_{1/2,D} = 4.32 \times 10^4$ s. The approximate solution is not shown, as it applies only to the scenario with infinite half-lives of TDP-43 dimers, monomers, and free misfolded oligomers. The results are displayed for three values of k_M. The case with $k_1 = 10^{-6}$ s^{-1}, $k_2 = 10^{-6}$ μM^{-1} s^{-1}, and $\theta_{1/2,B} = 10^7$ s.

(a)

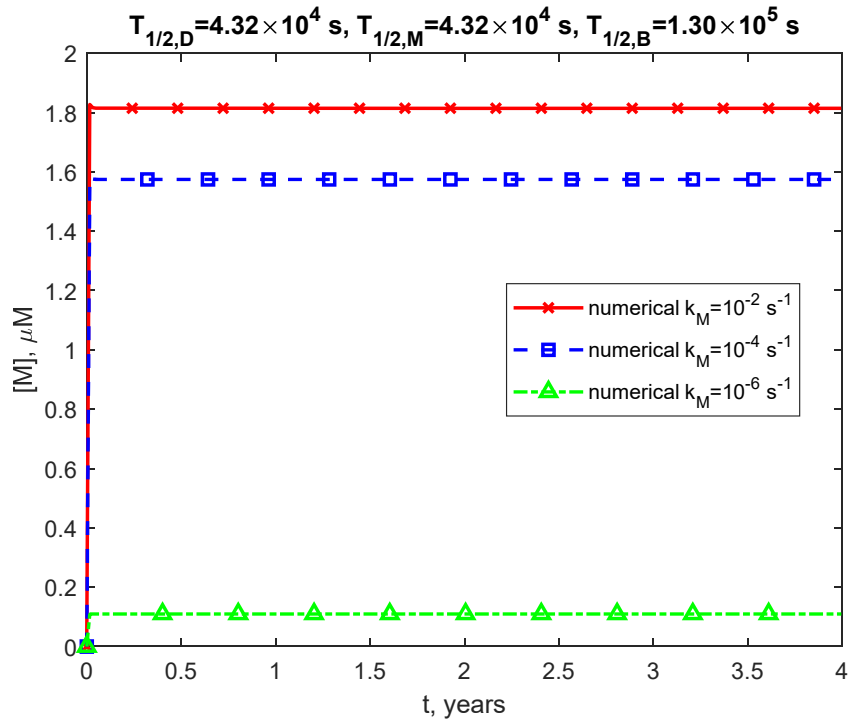

(b)

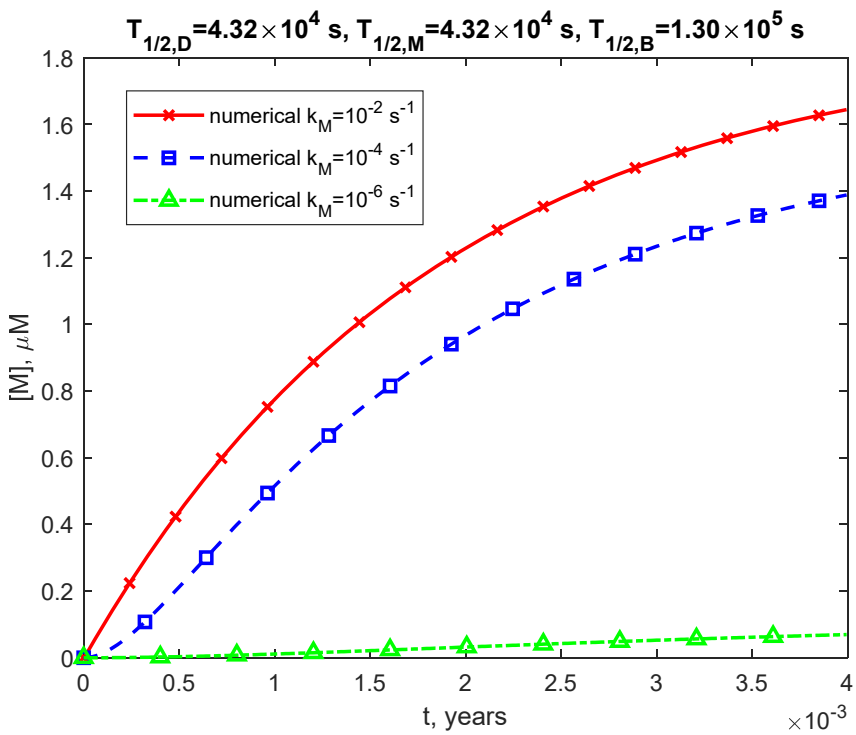

Fig. S22. (a) Molar concentration of TDP-43 monomers, [*M*], as a function of time (in years). (b) Similar to Fig. S22a, but with a focus on the specific time range of [0, 0.004 years] on the *x*-axis. The numerical

solution is obtained by solving Eqs. (4)-(7) with initial conditions (8). The presented scenario assumes physiologically relevant half-lives for TDP-43 dimers, monomers, and free misfolded oligomers: $T_{1/2,D} = 4.32\times10^4$ s, $T_{1/2,M} = 4.32\times10^4$ s, and $T_{1/2,B} = 1.30\times10^5$ s. The approximate solution is not shown, as it applies only to the scenario with infinite half-lives of TDP-43 dimers, monomers, and free misfolded oligomers. The results are displayed for three values of k_M. The case with $k_1 = 10^{-6}$ s^{-1}, $k_2 = 10^{-6}$ μM^{-1} s^{-1}, and $\theta_{1/2,B} = 10^7$ s.

(a)

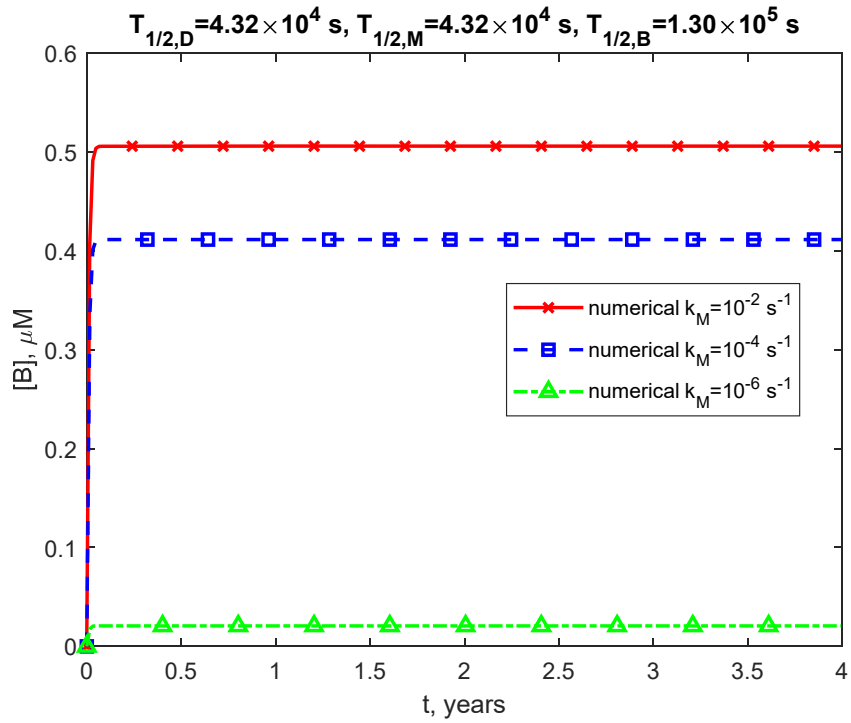

(b)

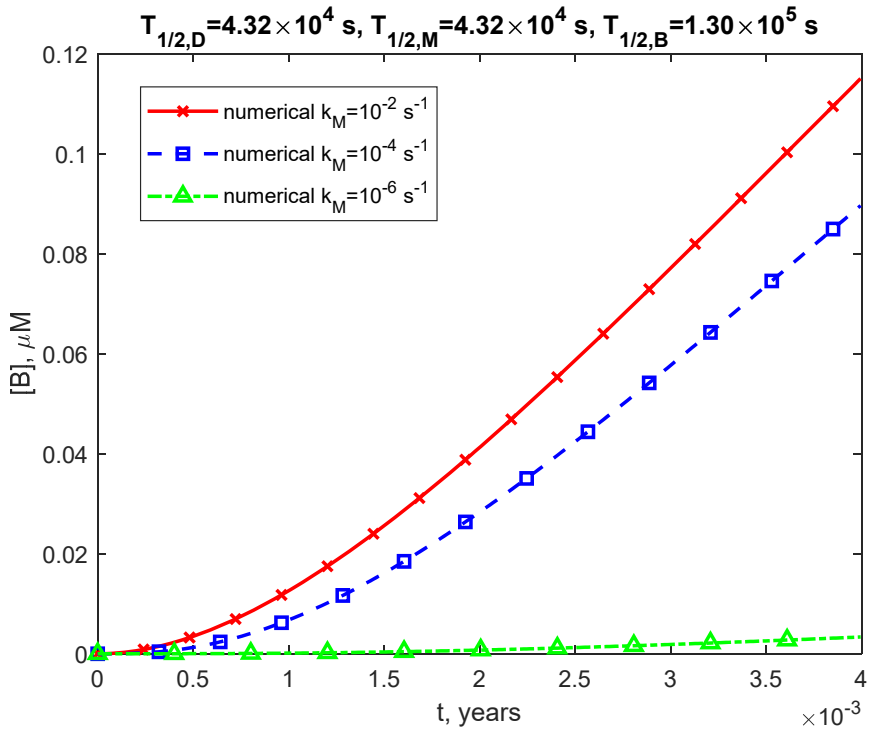

Fig. S23. (a) Molar concentration of free misfolded TDP-43 oligomers, [*B*], as a function of time (in years). (b) Similar to Fig. S23a, but with a focus on the specific time range of [0, 0.004 years] on the *x*-axis. The numerical solution is obtained by solving Eqs. (4)-(7) with initial conditions (8). The presented scenario assumes physiologically relevant half-lives for TDP-43 dimers, monomers, and free misfolded oligomers: $T_{1/2,D} = 4.32\times10^4$ s, $T_{1/2,M} = 4.32\times10^4$ s, and $T_{1/2,B} = 1.30\times10^5$ s. The approximate solution is not shown, as it applies only to the scenario with infinite half-lives of TDP-43 dimers, monomers, and free misfolded oligomers. The results are displayed for three values of k_M. The case with $k_1 = 10^{-6}$ s^{-1}, $k_2 = 10^{-6}$ μM^{-1} s^{-1}, and $\theta_{1/2,B} = 10^7$ s.

(a)

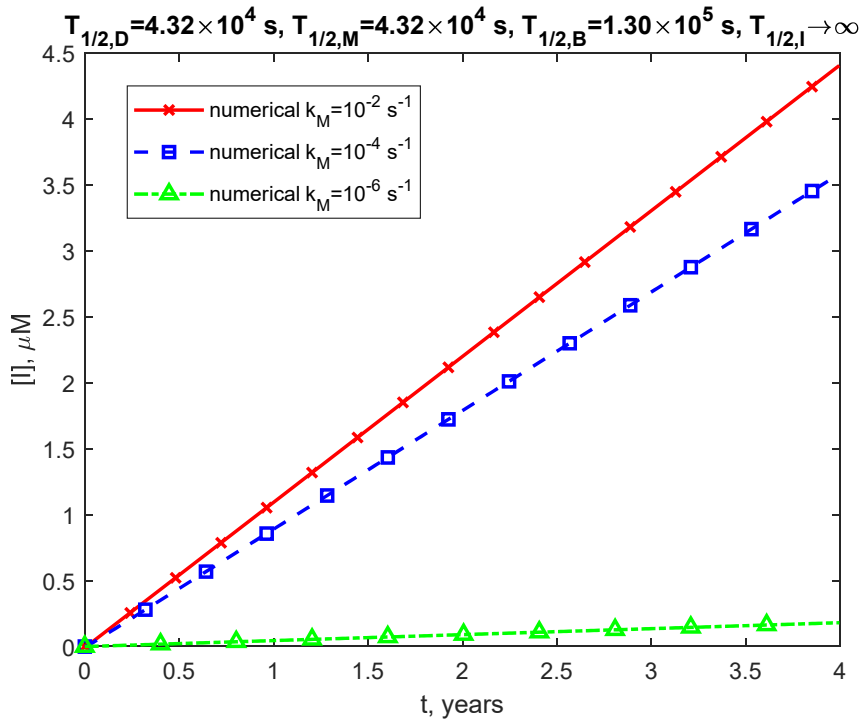

(b)

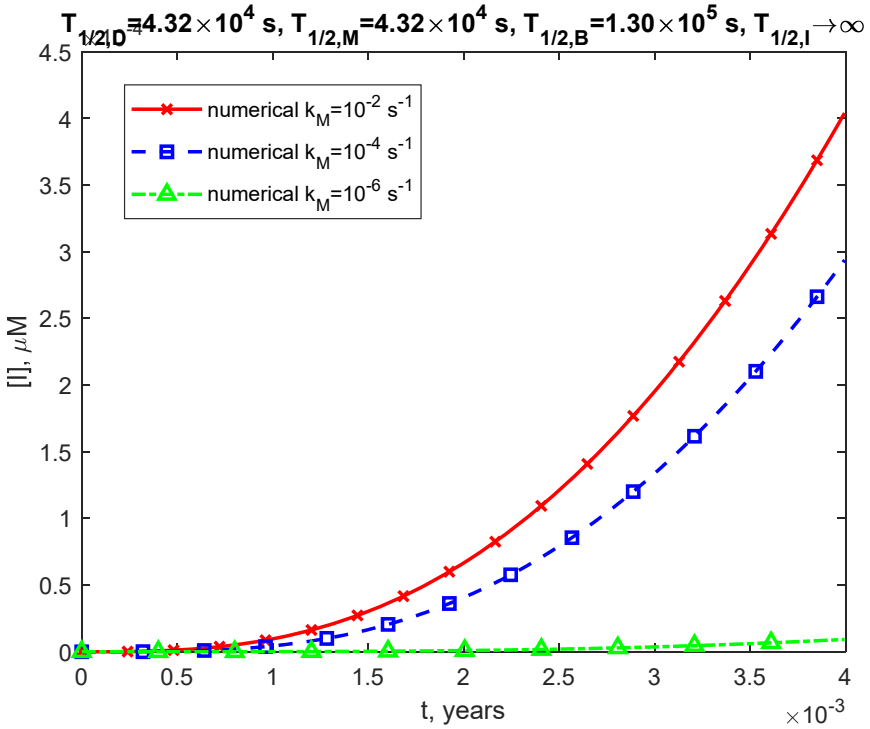

Fig. S24. (a) Molar concentration of toxic TDP-43 oligomers incorporated into inclusion bodies, [*I*], as a function of time (in years). (b) Similar to Fig. S24a, but with a focus on the specific time range of [0,

0.004 years] on the *x*-axis. The numerical solution is obtained by solving Eqs. (4)–(7) numerically with initial conditions (8). The presented scenario assumes physiologically relevant half-lives for TDP-43 dimers, monomers, free misfolded oligomers, and oligomers deposited into inclusion bodies: $T_{1/2,D} = 4.32 \times 10^4$ s, $T_{1/2,M} = 4.32 \times 10^4$ s, $T_{1/2,B} = 1.30 \times 10^5$ s, and $T_{1/2,I} \to \infty$. The approximate solution is not shown, as it applies only to the scenario with infinite half-lives of TDP-43 dimers, monomers, and free misfolded oligomers. The results are displayed for three values of k_M. The case with $k_1 = 10^{-6}$ s^{-1}, $k_2 = 10^{-6}$ μM^{-1} s^{-1}, and $\theta_{1/2,B} = 10^7$ s.